Investigation of the mechanical properties of printed circuit boards for nanosatellite

by

TSHIPOY WILLIAM MUKIND

Dissertation submitted in the partial fulfilment of the requirements for the degree

Master of Engineering in Satellite Systems and Applications

in the Faculty of Engineering and Built Environment

at the

Cape Peninsula University of Technology

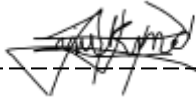**Supervisor: Dr T. NGONDA**

Co-supervisor: Mr S. MAKHOMO

Bellville campus

December 2022

DECLARATION

I, Tshipoy William Mukind, declare that the content of this dissertation represents my own unaided work, and that the dissertation has not previously been submitted for academic examination towards any qualification. Furthermore, it represents my own opinions and not necessarily those of the Cape Peninsula University of Technology.

_____   22 December 2022

          Signed   **Date**

ABSTRACT

Printed circuit boards (PCBs) are the backbones of electronic devices, used in nanosatellite to mechanically support, electrically connect, and protect electronic components of different subsystems. Their use in the space industry requires better knowledge of how they will react to the application of mechanical stress, because once in space there is no way of addressing any failure caused by structural deficiency. Therefore, the present work aimed at investigating the reaction of four-layer printed circuit boards to the application of static mechanical load. To achieve its aim, three objectives have been assigned to this dissertation: to characterize the reaction of the board to tensile stress and flexure stress, and to determine the allowable stress the board can withstand without compromising its structural performance. Hounsfield and Zwick Roell Universal Testing Machine (UTM) were used, respectively, to assess the board to tensile stress and to flexure stress using a three-point bend test; fractography analysis was undertaken with a Nikon SMZ25 microscope to validate the results.

The FR-4 and Mercurywave samples were found, respectively, to have an ultimate tensile strength of 200.9084 MPa and 151.3143 MPa; a flexure strength of 602.7 MPa and 333.6 MPa; an ultimate tensile strain of 9.8% and 7.1%; a Young's modulus of elasticity of 6.8 GPa and 5.9 GPa; a flexure modulus of elasticity of 42.0 GPa and 23.7 GPa; a Poisson's ratio of 0.8% and 0.9%; a bending stiffness of 32.3 N/mm and 28.1 N/mm; a percentage elongation of 9.8% and 7.1%; and a deflection angle at fracture of 52.3% and 46.2%. The discussion has shown that the FR-4 sample will react significantly better to the application of tensile and flexure stress, and fractography analysis has validated the findings of the result analysis by showing trans-laminar and intra-laminar fracture morphology on the surface of the samples tested to tensile test and trans-laminar, intra-laminar and interlaminar fracture morphology on the surface of the samples tested to flexure test.

Keywords: Modulus of elasticity; stiffness; strain; stress; deflection angle at fracture; FR-4, fractography; interlaminar; intra-laminar; Mercurywave; percentage elongation; printed circuit boards; trans-laminar.

ACKNOWLEDGEMENTS

I wish to thank the following people:

- Dr Tiyamike NGONDA, for guiding me throughout the completion of my Master of Engineering degree.
- Mr. Selbourne MAKHOMO, for being there next to Dr Ngonda, ensuring that the work is done correctly.
- Prof Robert Van Zyl, for the opportunity given to pursue my study with F'SATI.
- The F'SATI technicians who helped with the acquisition of materials for my research work.
- CPUT Mechanical Department for support in purchasing material for my research.
- Mr. Williams BRADLEY, for his availability and support during my research work.
- Ms. Penny LOUW, Senior Technician Officer at UCT centre for material engineering for giving me access to their laboratory and supervising the flexural experiment work and post-fracture analysis.
- Ms. Shaheeda PETERSEN, for her support and supervision of the tensile experiment work and post-fracture analysis.
- My parents, for being there for me throughout my academic life.
- My family, for the moral, financial, and emotional support.
- My colleagues and friends, for always pushing me towards perfection.
- My beautiful fiancé, for being my pillar of strength every stage of the way.

DEDICATION

If it had not been the Lord who was on our side, now may Israel say; If it had not been the Lord who was on our side, when men revolted against us: then they had swallowed us up quick, when their wrath was kindled against us: then the waters had overwhelmed us, the stream had gone over our soul: then the proud waters had gone over our soul. Blessed be the Lord, who hath not given us as a prey to their teeth. Our soul is escaped as a bird out of the snare of the fowlers: the snare is broken, and we escaped. Our help is in the name of the Lord, who made heaven and Earth.

(Psalm 124, KJV)

TABLE OF CONTENTS

LIST OF EQUATIONS

LIST OF FIGURES

LIST OF TABLES

ABBREVIATIONS AND ACRONYMS

PCB   Printed circuit board

UTM   Universal testing machine

ZACube   South African nanosatellite mission

DIP   Dual-in line packages

FR-4   NEMA grade designation of glass-reinforced epoxy resin laminates material

F'SATI   French South Africa Technical Institute

RF   Radio frequency

EMI   Electromagnetic interference

PWB   Printed wiring board

ISO   International Standard Organization

ASTM   American Society for Testing and Materials

EPS   Electrical power system

OBC   On-board computer

GPS   Global positioning system

PPM   Pulse-position modulation

ANSYS   Analysis system

FEA   Finite element analysis

SGF   Short glass fibre

SERR   Strain energy release rate

SMZ25   Stereo microscope with zoom ratio of 25:1

NOTATIONS

Units

g	Gram
N	Newton
kN	Kilo Newton
mm	millimetre
MPa	Mega Pascal
GPa	Giga Pascal
%	Percentage

SYMBOLS

Symbol	**Name**	**Measurement**
δ	Small delta	Deformation
σ	Sigma	Stress
ε	Epsilon	Strain
ν	Greek letter ν	Poisson's ratio
E	Letter e	Young's modulus of elasticity
P	Letter p	Applied load
Δ	Capital delta	Changes

1. INTRODUCTION

1.1. Introduction

Printed circuit boards (PCBs), Figure 1-1(Printplaat, n.d.), are backbones of electronic apparatus; they are used to mechanically support electronic components and electrically connect them between themselves and with external devices (Church *et al.*, 2013). The impact of mechanical stresses on PCBs is an area of interest for almost all electronic applications as they are critical to any electronic plant performance. In a nanosatellite mission, repairs or maintenance of structural components are almost impossible once the spacecraft enters its orbit. Therefore, it is of utmost importance to ensure PCB integrity under stresses caused by the applied static mechanical load before these PCBs are put in their working environment and exposed to critical conditions.
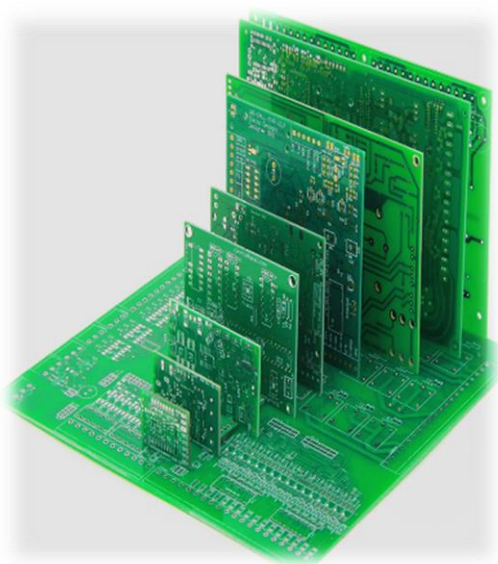
Figure 1-1: Printed circuit boards

PCB mechanical characteristics such as material strength and material elastics constant are important parameters in assuring the effectiveness of PCB for its use in space mission. Two mechanical experiments used to characterize the boards are presented in this paper: tensile and flexure testing. Tensile characterisation was done through a tensile test performed on a Hounsfield universal testing machine (UTM) to investigate the reaction of the PCBs. The tensile stress experienced by the PCBs is caused by reaction of the structure of the nanosatellite to aerodynamic pulling load. Properties such as the ultimate strength, the ultimate strain, yield strength, offset, Poisson's ratio and Young's modulus of elasticity will

be investigated as important parameters of any structure that is supposed to be subjected to mechanical loading.

The flexural characterisation was done through a three-point bend test performed on a Zwick Roell UTM. The test was performed to primarily study the behaviour of the PCBs used in the development of the South African nanosatellite mission. In use these boards are subjected to the load applied by the electronic components they support and therefore this test was done to evaluate their structural integrity. Property such as the flexural strength that the board can oppose to applied load was the primary concern of the test undertaken.

The determination of how much the board can deform before fracture occurred was the second concern of this test. It is important to make sure that during its uses, the pc board of one subsystem does not bend to a level where it encounters an electronic component of any other subsystem and negatively affect the satellite's operation. The third concern of the test was to evaluate the fracture morphology of the board under stress applied along and across its load-bearing fibres.

These properties were measured in terms of three distinct aspects described as.

- The necessary stress that can cause a deformation of the board found at a point of the stress-strain curve called the inflection point
- The stress at which the deformation of the specimen deviates from its linear slope defining the yield strength; and
- The maximum stress the specimen can withstand before it breaks.

1.2. Problem statement

The use of PCBs in the space industry requires a clear knowledge of how they will react to the application of mechanical stress. This is because; in space there is no way of addressing any failure caused by the structural deficiency of a PCB. The complexity rises with the individualisation of each designed PCB as they are designed based on a specific mission. Whereby, the behaviour of one PCB cannot be assigned to another unless they were designed for the same mission with the same exact specifications. Therefore, the present work investigates the reaction of four-layer PCBs to flexure and tensile stresses.

1.3. Research aims and objectives

The aims of this research work were to analyse the mechanical behaviour of printed circuit boards used for ZACube nanosatellite and provide data for its mission development. To achieve these aims, the following objectives were pursued:

- Characterise the reaction of the PCBs to tensile stress.
- Characterise the reaction of the PCBs to flexure stress.

1.4.Research background

The design of printed circuit boards is conditioned primarily by the number of power planes and routing layers purposed to its functionality, with consideration to minimising the development cost. The number of layers required on a specific PCB is a function of its design purpose, capability to discriminate noise, category signal separations, number of routed traces (nets), control of the impedance, buses' routing and individual circuit's component density(Montrose, 2000). The identification of the PCB is based on the number of copper layers it contains. It was found that PCBs exist as:

- *Single-sided PCB* is generally reserved to electronic devices that do not contain periodic signal design, primarily used in the design of analogue instrumentation and control systems.

- *Double-sided PCB* is a configuration that exists in two basic layouts: the dual-in line packages (DIP) is mainly used in the design of memory arrays where the device function at a slow speed rate; and the enhanced doubled-sided routing that enables radio-frequency return current. This configuration is an upgraded DIP version with routing made easier to achieve.

- *Four-layer PCB stack up* is a configuration specific to the use of reference planes, increasing the possibility of cancelation of flux in radiofrequency (RF) currents.

- *Six-layer PCB stack up* is a design configuration that provides much lower power with ground plane impedance compared to a four-layer configuration; the lower impedance is a quality that creates room for improving the overall decoupling for electronic devices.

- *Eight-layer PCB stack up* is a configuration specific to the suppression of the electromagnetic interference (EMI) and the enhancement of the signal integrity.

- *Ten-layer PCB stack up* is a PCB design configuration aimed at improving impedance control and radio-frequency flux cancelation.

The structural configuration of a PCB is determined by the applications for which it is designed; these applications are set into two fundamental areas: the analogue radio frequency (RF) and the digital radio frequency. The difference in these two fundamental areas of PCB application is in the ability of the PCB to tolerate signal losses and the complexity of its structural configuration (Lee W. Ritchey, 1999):

- The *analogue RF circuit* processes short and precise signals, a complexity not that much in the way that two- or three-layers PCBs can be used to accommodate such circuits.
- The *digital RF circuit* is designed to process more complex circuits with substantial tolerance in signal loss; digital circuits are complex and demand a certain number of signal and power layers to accommodate them.

The above description shows how complex a PCB can be, but this complexity is enlarged by the fact that space technology is following an innovative trend utilising miniaturised electronic packages enclosed in cubic aluminium boxes of 100-mm cube (4-inch cube packaging for Beanie Babies), 1 kilogram often referred to as U1, to achieve big space missions. The mystery behind the successful miniaturisation of space technology is found in the complexity of the PCB design. The major challenge faced by Twiggs and his team was to provide support and connectivity to different miniaturised electronic components that comprise the satellite. This challenge was overcome by the capacity of a PCB to mechanically support, electrically isolate, and electronically connect different electronic devices within a system or subsystem. The satellite made in the size of this cubic is called nano-satellite or Cube Sat (Deepak & Twiggs, 2012). The Cape Peninsula University of Technology (CPUT) satellite mission, ZACube, utilises Cube Sat technology to realise the South African space mission; it uses off-shelf PCBs in its electronic package for the development of ZACube. The only available information relative to these PCBs is that of the material properties considered individually, but PCBs are not made of one material but are a composite of at least four layers of different materials: copper as a conductor layer; prepreg

as a dielectric layer; a flame-retardant material layer; and a liquid photo imageable as a mask layer. The F'SATI's (French South African Technical Institute) technicians have no PCBs data on which to rely for the prediction of a PCB reaction to mechanical stress or prevention of failure. A document containing different mechanical properties of PCBs is required.

1.5. Research methodology

For the purpose of this research study, the observational experimental was adopted as methodology and was processed in the following phases:

Phase 1: Investigating the structural configurations of the PCBs, focus on the F'SATI design.

Phase 2: Mechanical characterisation of the PCBs using the universal testing machine; and

Phase 3: Investigation of the failure mode using fractographic analysis.

1.6. Delineation of the research

This research will be restricted to the study of the mechanical properties of the two types of PCB used in the development of ZACube mission. The below structure will be followed:

- *Chapter 1:* This introduction presents different element describing the topic and the overall approach to this research work.
- *Chapter 2:* This chapter presents literature on different aspects of printed circuit board and different properties that will be investigated in the present work.
- *Chapter 3*: This chapter presents the methodology followed to achieve the aims and objectives of this research.
- *Chapter 4:* This chapter focuses on the analysis of the results.
- *Chapter 5*: This chapter presents a discussion of the results.
- *Chapter 6*: This chapter concludes by giving a summary of the objectives, indicating whether they have been achieved or not and offering recommendations as outcomes of the findings from the discussion.

2. LITERATURE REVIEW

2.1. Printed circuit board

A printed circuit board, or printed wiring board (PWB), is a multi-layered laminate structure wherein each laminate layer consists of different material. Each these materials have specific mechanical properties that impact the performance and structural integrity of the PCB as a composite material. The diverse basic laminate layers of PCB – copper foil, flame retardant material, dielectric material and solder mask – with their specific material characteristics offer to the PCB a profound orthotropic and anisotropic character (Barua et al., 2016). But due to the viscoelastic character of the dielectric layers, stress relaxation and creep properties are provided to the composite to limit deformation along its edges (Rahangdale et al., 2017).

2.2. Use of PCB in the nanosatellite industry

PCBs are the backbones of satellites because they mechanically support and electrically connect electronic components; hence, they are exposed to various thermal and mechanical load conditions. Knowledge of their mechanical and thermal properties helps to prevent failure and predicts their thermal and mechanical behaviour (Bhavsar *et al.*, 2014).

Nanosatellites consist of several electronic packages that meet functional requirements. These electronic packages constitute the assembly of PCBs mounted in the mechanical structure. Electronic pieces are placed mechanically on these PCBs and interconnected electrically using PCBs' circuit-foil (Jayaraman *et al.*, 2016).

A study presented by the Space Technology Synthesis Laboratory of Chosun University evaluated the validity of a 1U Cube satellite design for their 2015 space mission to quasi-static analysis and modal analysis. A PCB of 0.368 kg served as backbone of the system to support subsystem components such as the electrical power system (EPS), the communication devices, on-board computer (OBC), the pulse-position modulation (PPM) and the global positioning system (GPS). Investigation of the allowable deflection margin of the PCBs that can be accommodated by the structural operation of this cube satellite was undertaken with a quasi-static load of 42.3 g. A maximum deflection of 0.180 mm was found with an allowable deflection of 0.435 mm. The structural safety of 0.93 was found to have the highest probability of safe use of the PCB on this particular nanosatellite (Oh *et al.*, 2014).

2.3. Mechanical assessment of PCBs

Mechanical properties of material, measures of the reaction of the structure to an external mechanical applied load are used to predict the behaviour and failure mode of a structure under mechanical applied load or stresses. They are also used to determine the potential application and sustainability of a mechanical structure (Mabuwa, 2022).

A study was conducted on the different mechanical testing methods required to assess composite polymer materials and relative typical standard test methods for the characterisation of different mechanical properties and failure mode analysis based on the International Standard Organization (ISO) and the American Society for Testing Materials International (ASTM). Details are given on when to use a specific testing method for a specific mechanical characterisation of specific composite material (Forster, 2015).

2.3.1. Assessment of the tensile properties

A review article on Poisson's ratio and modern material describes Poisson's ratio (ν) as a provision of a universal mean of expressing the performance of a homogeneous or non-homogeneous structure as real materials. It is said to be the ratio of the lateral to the axial strain defined within the elastic zone of loading direction. The Poisson's ratio of isotropic material must be defined in a range of $-1 \leq \nu \leq \frac{1}{2}$; for solid materials like ceramics, metals and polymers, it should be defined within a range of $0.25 < \nu < 0.35$; for glass and mineral materials which are highly compressible, the Poisson's ratio is approximate to zero. Some materials having a negative Poisson's ratio are called auxetic, but anisotropic materials with elastic directional properties have Poisson's ratio that can be negative when exposed to tensile load applied parallel to the fibre direction and positive when applied in the direction orthogonal to the direction of the fibre (Greaves & , A. L. Greer, 2011). Research has demonstrated that the Poisson's ratio of monoclinic, orthotropic and triclinic materials can be either positive or negative except for cubic materials (Ting & Chen, 2005). The tensile Poisson effect is defined as a phenomenon where a material subjected to applied tensile load in a specific direction tends to expand in the direction of the load and shrink in the other two directions normal to the axis of the applied load (Hassan, 2016).

The strength of a material structure is determined by the structure's adequate performance while exposed to stresses. The test that enables the prediction or evaluation of the deformation response of a structure subjected to pulling load is called tensile test. Two

7

authors have proposed the determination of tensile properties of metallic structure used in the construction industry using an electronic extensometer, and that of wood using a Hounsfield Tensometer, and the flexural properties of these construction materials using a three-point bending jig fitted on the Hounsfield universal testing machine. The results of the tests were compared to the theoretical values (Itugha & Jumbo, 2019).

E-glass epoxy laminates fabricated at different fibre orientations were evaluated through tensile tests and the results of the experimental work were compared to those of the ANSY FEA software. The comparisons yielded an average error in the software result of about 4.2% (Kalia *et al.*, 2018).

The analysis of the strength of a hybrid composite laminate to tensile loading where properties such as; Poisson's ratio, Young's modulus, shear modulus and bulk modulus were investigated. The results showed that the fibre bonding and the matrix strength of the laminate were functions of the time of curing. While this time of curing also affects the strength of the laminate, it was concluded that the strength of the laminate is primarily a function of the orientation of the laminate layers' fibre (Sri *et al.*, 2015).

The level of reliability of Resign Coated Copper (RCC) board was compared to that of an FR-4 board with a leverage of experimental analysis like tensile strength using a universal tensile machine; time and temperature dependent viscoelastic behaviour using a dynamic mechanical analyser; and coefficient of thermal expansion, Young's modulus and Poisson ratio using a thermo-mechanical analyser. The results of the thermo-mechanical analysis were used to simulate the level reliability of the boards using ANSYS finite element analysis software, but the results of software simulations are just imaginary evaluations and not real time performance evaluations of the board and should be considered with caution (Rahangdale *et al.*, 2017).

The tensile and compressive properties of a glass fibre epoxy and glare laminate subjected to hygrothermal conditioning were compared to those of the unconditioned samples. The experiment was conducted on an Instron UTM based on standard ASTM-D3039-76 at a head speed of 1.27 mm/minutes. The results obtained from the tests performed yielded concluding remarks; the hygrothermal conditioning of the samples did not cause any significant change in the samples' properties. The Young's modulus and Poisson's ratios for the dry samples were found to be [27.4 GPa, 2.20%] for the Glass fibre epoxy [53.3 GPa, 1.70%] and for the

glare laminate, and for the wet samples [24.7 GPa, 1.80%] and [52.7 GPa, 1.90%] (Botelho & Almeida, 2007).

2.3.2. Assessment of the flexure properties

Techniques of mechanical representation of characters used in the study of different failure modes of epoxy glass structured in a sandwich configuration of an electronic circuit board were analysed. Focus was on material strength and material elastic properties of the sandwich structure evaluated through the tensile and the three-point bending test. It was demonstrated that the three-point bending test has an inconvenience: stresses are more concentrated in the middle, predefining a breaking point of the specimen where the loading point is centred. Thus, the strain limit in the specimen is not met, giving less possibility to achieving the specimen bending maximum strain (Pietrikova *et al.*, 2020).

The experimental results of the bending stiffness and the shear stiffness of an industrial PCB using a four-corner shear and a four-point bend test were compared to that of FEA (finite element analysis) in this study. Results showed that the FEA results were overestimated compared to that of the experimental analysis. It was noted that FEA software is designed for isotropic material, but PCBs are anisotropic materials as they are composite materials, and this gives room for inconclusive evaluations. Experimental assessment should always prevail for compliance and reliability purposes (Loon *et al.*, 2019).

The experimental results from a three-point bend test of a two-layer laminate made of glass fibre epoxy as the first layer and Kevlar epoxy as a second layer is compared to the theoretical value of its flexural strength in this study, comparing the volume fraction of each layer as the bending load is applied to the specimen. Three properties were investigated, with comparisons between their theoretical and experimental results evaluated. These properties were as follows: the deflection, the compressive stress on the upper midsection of the specimen, and the tensile stress on the lower midsection of the specimen. The result showed that the experimental results of the deflection and compressive stress were about 0.6% smaller than the theoretical value, and the tensile stress 0.6% greater than the theoretical value (Uleiwi, 2007).

Three composites laminate – flax hemp, flax MAPP and flax epoxy – were tested to mechanical load such as impact and flexural stress, with results compared and reported in this paper. The flexural test was conducted using a three-point bending test based on standard

ASTM D-790, and the Rockwell hardness test was conducted to test the laminates to impact load. The results of the test showed that the ultimate flexural strength of the hemp laminate was 88.26 MPa, 86.26 MPa for the flax MAPP, and 18 MPa for the flax epoxy providing evidence that the hemp sample has a higher flexural strength due to the strength of hemp fibre (Sharavanan *et al.*, 2018).

2.4. Assessment of fractography analysis

Fractography analysis of the effect of hygrothermal conditioning of carbon fibre epoxy laminate subjected to compressive load was presented in this paper, with different modes of compression failure described, such as:

- *Shear failures* defined as failures that occur either through the thickness, in-plane or along the wedge.
- *Interlaminar fracture* defined as failures that occur by delamination due to buckling or splitting of the laminate.
- *Interfacial failures* defined as failures that occur by brooming or crushing of fibre.
- *Kink-band fractures* defined as failures that occur through the thickness kink bands or in-plane kink bands.

The result of the fracture analysis indicated that the lower compression strength observed in the tested sample was due to a decrease in the polymer matrix stiffness caused by the hygrothermal conditioning of the sample (Opelt *et al.*, 2017).

A proposition of a new categorisation of the compressive fracture modes of reinforced fibres composite material based on microscopic evaluations on different laminate was presented in this paper. Scanning electron microscopy was used to investigate the different modes of compression failure of hybrid composite material. Compression failure was classified within four main modes:

- The *first mode* was the shear failure characterised by the in-plane shear, through the thickness shear and wedge splitting.
- The *second mode* was the interlaminar failure characterised by delamination buckling and longitudinal cracking.
- The *third mode* was the interfacial failure characterised by longitudinal cracking, brooming and fibre crushing.

- The *fourth mode* was the Kink-band failure characterised by the in-plane kink-band and the through-thickness kink-band.

The major finding of this paper was the characterisation of the wedge splitting fracture mode of a sample subjected to compression stress (Opelt *et al.*, 2018).

Fractography analysis was undertaken to evaluate the possibility of improving the strength effect of the epoxy matrix of the carbon fibre-reinforced composite material. This paper proposes a solution that consists of enhancing the surface area of the grafted fibre of carbon nanotubes, improving the matrix-fibre bonding and thereby strengthening the matrix using the carbon nanotubes (Sharma & Lakkad, 2015).

A study was presented on multivariable analysis methods that used acoustic data emission to do in-service analysis of the fracture modes of composite glass fibre reinforced polymer material tested to tensile load. Post-fracture analysis on a Scanning Electron Microscopy validated the result. Four failure modes – matrix cracking, interfacial de-bonding, fibre breakage and delamination – were presented as four main failure modes of composite material subjected to tensile stress. Analysis determined that the matrix cracking occurred at a strain of 0.22% and has led to failure of the sample at a strain of 1.55%; post-failure analysis has shown the presence of all four types of failure on the failed surface of the sample. It was concluded that the method presented in this paper was a potential manner for analysis of the failure mode of the sample during testing, but more work still needs to be done (Harizi *et al.*, 2022).

A study was presented in this paper analysing the bending character of composite material at different concentrations of short glass fibre (SGF). It was reported that a concentration of 0.1 SGF produced good flexural properties of the composite epoxy glass material. Fractography analysis assessed the structural configuration of the manufactured composite material. It has shown that the composite with SGF concentration of 0.1% gave good adhesion between the epoxy glass matrix and the SGF; the effective dispersion of the SGF in the matrix of the epoxy glass enhanced the bending properties of the composite material (Dasari *et al.*, 2021).

The analysis of a fractured surface of a scarf repaired laminate subjected to tensile stress was presented in this paper. It was noted that predominate failure modes identified on the fractured surface were as follows:

- Trans-laminar fracture or crack propagation occurring within the thickness region where failure of fibres was observed; and

- Intra-laminar fracture or propagation of failure within the thickness region where the matrix was broken or interfaces between matrix and fibre were de-bonded and pulled out of fibre along the warp tows.

Analysis of the adhesive films within different laminates of the composite was also investigated at the fractured surface. It is reported that the localised direction of crack propagation and radial line, fibre pull out, fractured fibres surrounded by matrix, and high interfacial adhesion of fibre to matrix prove that fracture was caused by tensile stress (Marques *et al.*, 2021).

A study investigating the rate at which growth of delamination as fatigue mode in epoxy or carbon-glass hybrid material subjected to fibre peel-off, striation or fibre bridging stress, determined a high possibility of generating a prediction model for the evaluation of the micro-fracture marking related to delamination of a hybrid laminate. The formation of tiny markings in the course of delamination describes the extension rate within the macroscopic degree while subjected to cyclic load. The impacts of the features of the delamination of the glass and carbon fibre at the microscopic degree are considered to foretell the rate at which a hybrid material behaves. Glass fibres give lower fibre bridging than carbon fibre, but glass fibre has a wide engraved area that results in a collaborative benefaction to the dissipation of energy for a hybrid material. The analysis was undertaken using the strain energy release rate (SERR) experiment method (Monticeli *et al.*, 2022).

A study of a novel perspective on the fracture of sandwich composite material used on wind turbine blades was presented in this paper. Fractographic analysis was used to investigate the fractured region of the sample. Two methods were used for analysis: the optical microscopy and X-ray computed tomography. A digital image correlation measurement was used to validate the state of the laminate skin strain. It is demonstrated that the fractographic parameters of epoxy glass-fibres laminate failed under the application of a bi-axial compressive stress caused by the buckling of the board. Characteristic such as shear dominated fracture, delamination, micro-cracks of resin, matrix-fibre interface and fibre cracks have been determined as the main failure mode observed on the morphology of the sample analysed in this paper (Chen, 2020).

3. RESEARCH METHODOLOGY

To achieve the aims of the present research work, three technical steps have been defined and are presented in this chapter. The first step was the identification of the samples and the investigation of their structural configurations. The second step was the mechanical characterisation of the properties of the identified samples. The third step was the fractography analysis. The mechanical characterisation consisted of investigating the reaction of the samples to tensile and flexure stress, and the fractography analysis consisted of investigating the morphology of the fracture surface to support the findings of the mechanical characterisation.

3.1. Identification of the sample

The identification of the samples occurred through research and consultation. Seven samples were provided by F'SATI, six Mercurywave and one FR-4 substrate PCB and four FR-4 substrate PCBs were purchased from Trax Interconnect. Figure 3-1 shows the two types of samples collected from F'SATI, with FR-4 denoting the FR-4 sample and MW the Mercurywave sample. The structural configuration of the sample was evaluated through research and supported by microscopy analysis.
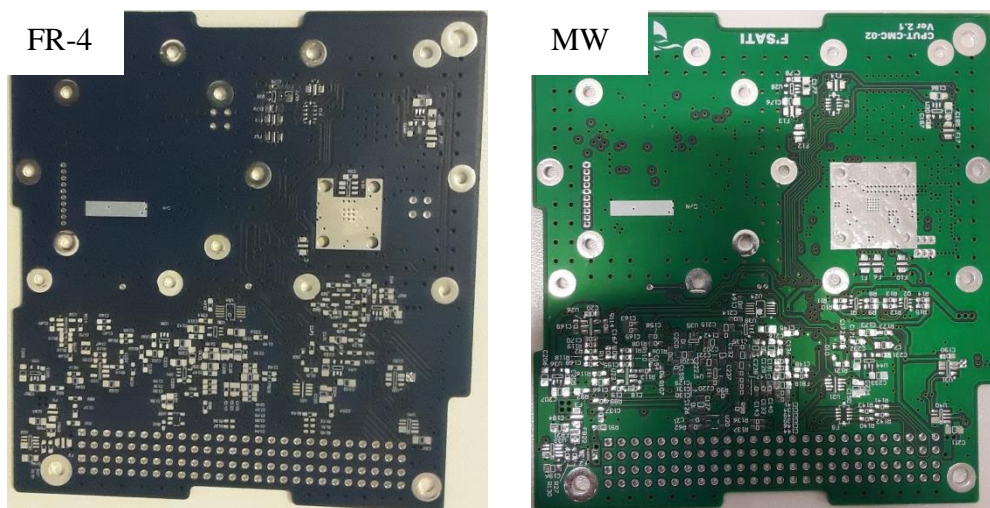
Figure 3-1: Samples

3.2. Testing and analysis equipment

The investigation of the behaviour of the samples will be done with the following equipment:

- Truecut mechanical shearing machine

- Hounsfield UTM
- Zwick Roell UTM
- Nikon SMZ25

➢ Truecut mechanical shearing machine

The Truecut mechanical shearing machine displayed in Figure 3-2 is a driving brake-motor that uses a shaft-mounted speed reduction unit and is controlled by a push button to command the stroke that can be either single or continuous. Providing silent on-the-spot engagement, it is one of the most ultra-modern small-scale mechanical cutting machines with minimum effect on the structure of the material. It has a low cutting angle with an inclined shear direction that minimises the twisting and reduces the bowing. The clearance of its blade set simply by manual manoeuvre, is used to cut materials such as metallic and composite laminate. It is a QH11D model with cutting thickness of 3.5 mm and cutting width of 1250
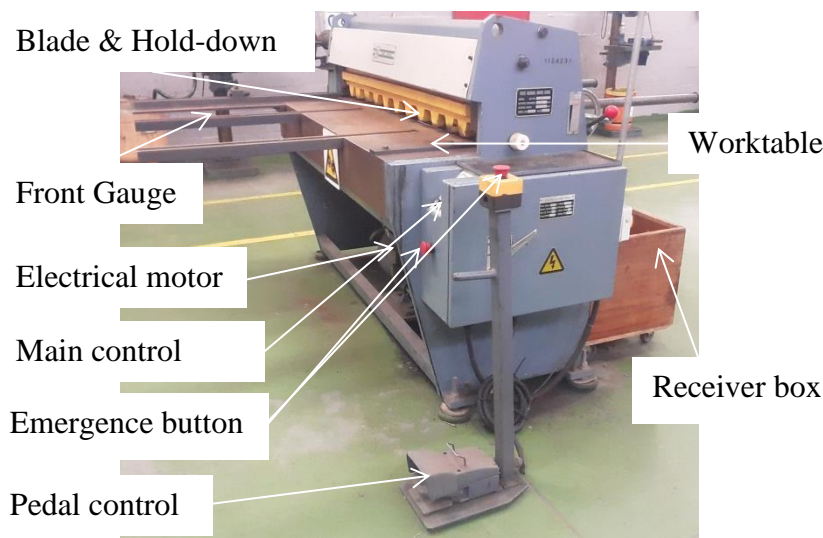
Figure 3-2: Truecut shearing mechanical machine

mm.

➢ Hounsfield UTM

The Hounsfield, illustrated in Figure 3-3, is a universal testing machine (UTM) for performing various mechanical tests. The actual one has the capability of performing only two tests: tensile and flexure tests. It is used with a load transducer of the type U4000 that carries a load cell of 50 kN maximum capacity, a control monitor to manually control the system, and a computer assisted machine control system and data acquisition software

Horizon, that allow the automatic control of the testing procedure and collection of data,

(b) Tensile test fixture   (a) Apparatus   (d) Manual control monitor
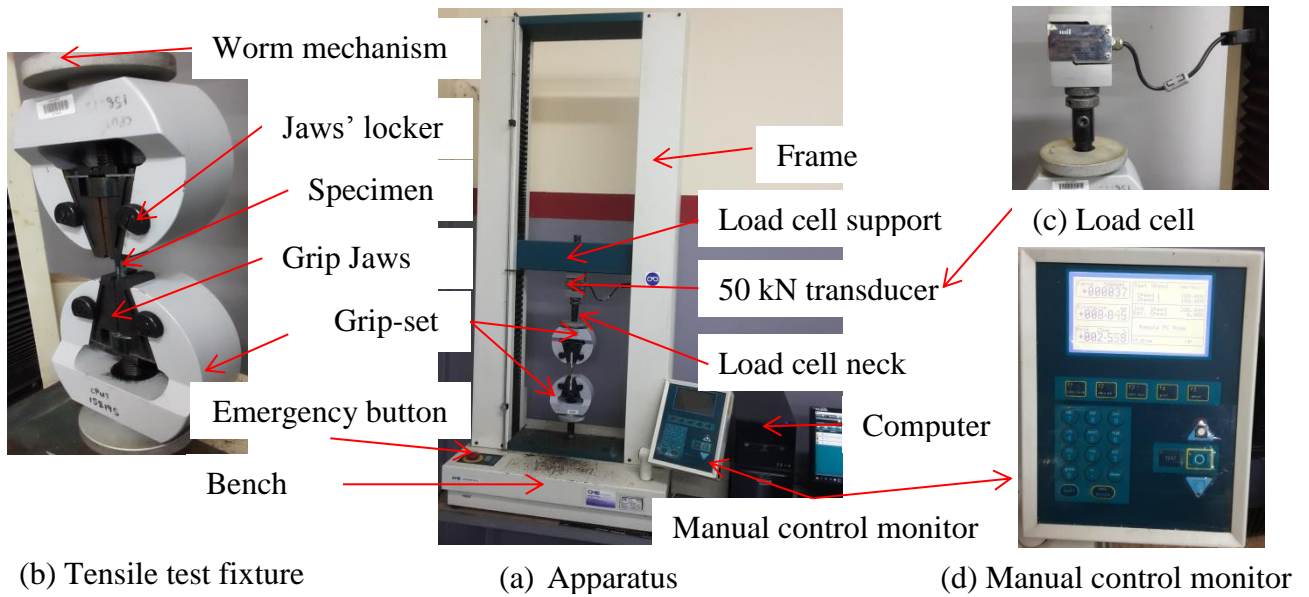
Figure 3-3: Hounsfield universal testing machine

analysis and graphical representation of the behaviour of the tested specimen.

> **Zwick Roell UTM**

The Zwick Roell, illustrated in Figure 3-4, is also a universal testing machine for performing various mechanical tests. The need for this alternative was because the Hounsfield UTM does not have the necessary accessories to perform a flexure test on the sample used in the present

(a) Apparatus   (b) Flexure test fixture
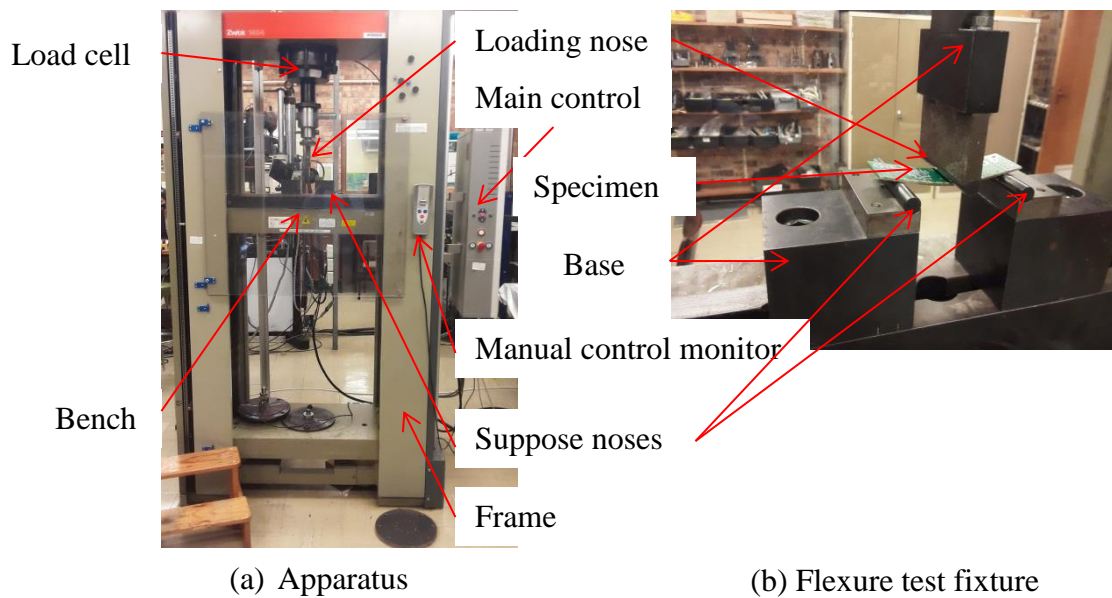
Figure 3-4: Zwick Roell universal testing machine

paper. This UTM is used with one loading nose that is mounted on the load cell of the machine; a base that carries two support noses is mounted on the bench of the machine. The load cell is used to measure the load applied to the specimen while the bench measures the deflection of the specimen.

> **Nikon SMZ25**

Figure 3-5 shows the Nikon SMZ25, a stereo or 3-D microscope with a microscope zooming range of 25.1. Offering a unique and exceptional capability, it is used for stereoscopic observations with high quality image capture and for applications that require lower magnification microscopic analysis. It is find it application in material science and industry, and can be extended to research and development activities, component surface examination, production quality control functions, failure analysis studies, crack detection, coating efficiency and composite materials for aerospace examinations.
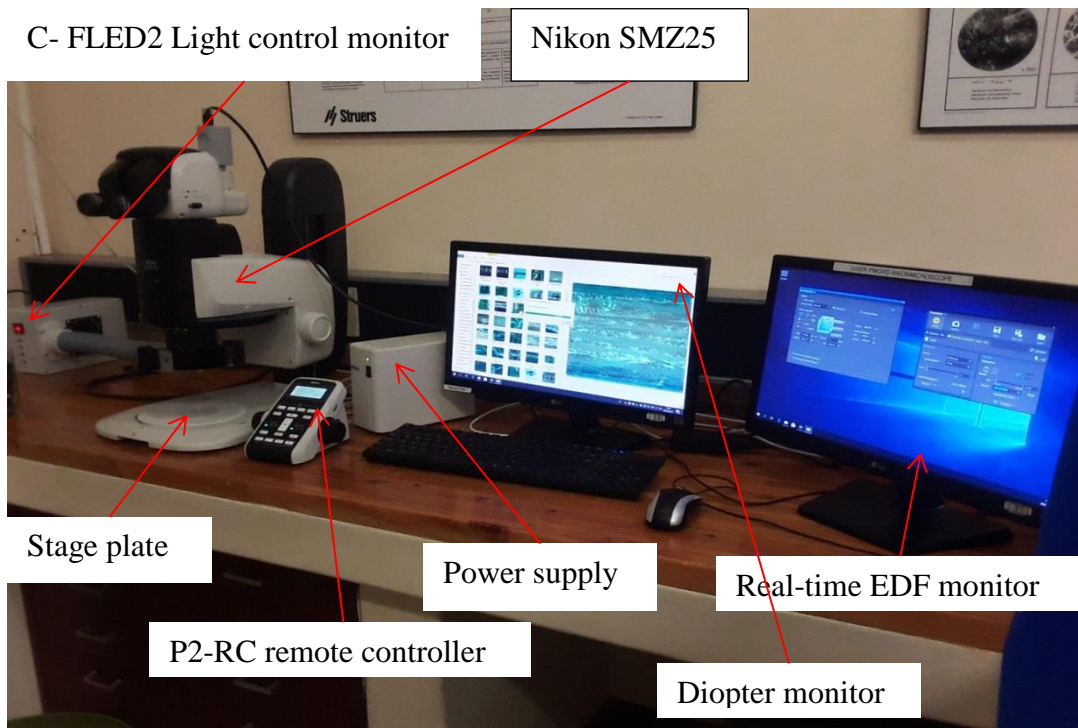
Figure 3-5: Fractography analysis equipment

3.3. Mechanical characterisation of the samples

The study of the reaction of the samples to mechanical stress will be limited to the two fundamentals mode of solicitation of the samples: the flexure and tensile stress. The tensile test will be done on the Hounsfield UTM at CPUT Bellville Campus Strength of Material Laboratory, and the flexure test will be done at UCT Material Science Laboratory.

3.3.1. Tensile test specimen preparation

The characteristics of the specimen were obtained from the ASTM 3039 standard, but because of the higher level of anisotropy of the sample, the dimensions of the sample were experimentally determined. The Truecut shearing mechanical machine was used to trim the PCBs to twenty-four specimens of rectangular shapes, with dimensions presented in Table 3-1 and Figure 3-6. Figure 3-7 displays the tensile specimens where MW_TL denotes the Mercurywave specimens cut along the 0° fibres, MW_TT denotes the Mercurywave specimens cut across the 0° fibres, FR-4_TT denotes the FR-4 specimens cut across the 0° fibres of the sample and FR-4_TL denotes the FR-4 specimens cut along the 0° fibres of the sample.

MW_TL

MW_TT

FR-4_TT

FR-4_TL
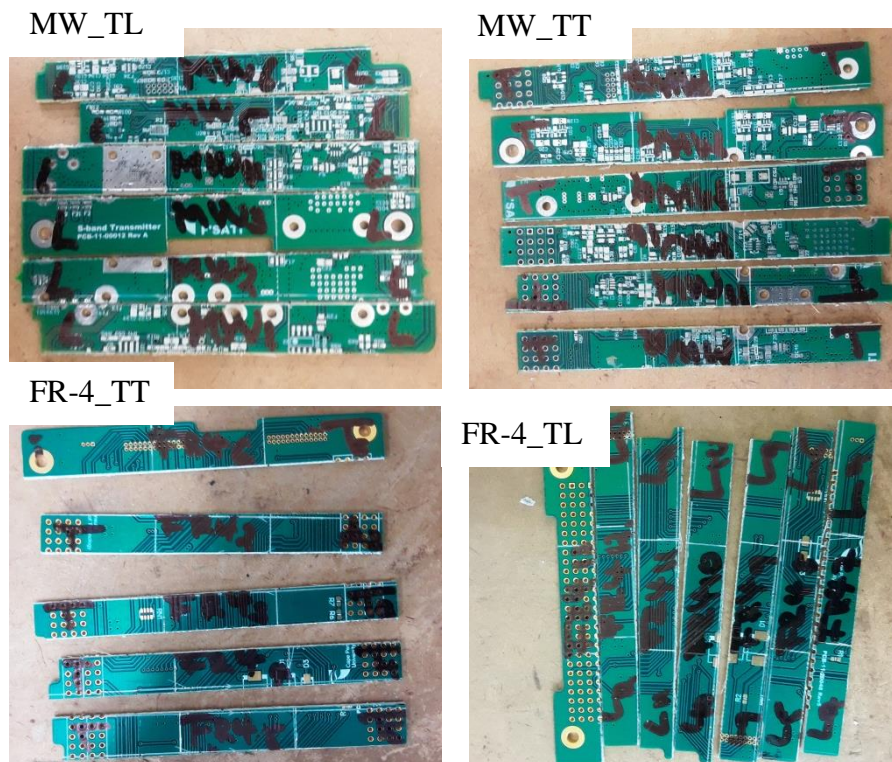
Figure 3-6: Tensile test specimens

Table 3-1: Tensile test specimens' dimensions expressed in mm

Sample	Specimen	Length	Gage length	Width	Thickness
FR-4	0° fibres	96	26.1	10.2	1.574
	90° fibres	90	26	10.4	
Mercurywave	0° fibres	96	24	10.7	1.623
	90° fibres	90	25	10.4	
Test parameters	UTM load cell	Load range	Head speed	Elongation range	Strain rate
	50 kN	0 to 5 KN	2 mm/min	0 to 3 mm	0.54 mm/min
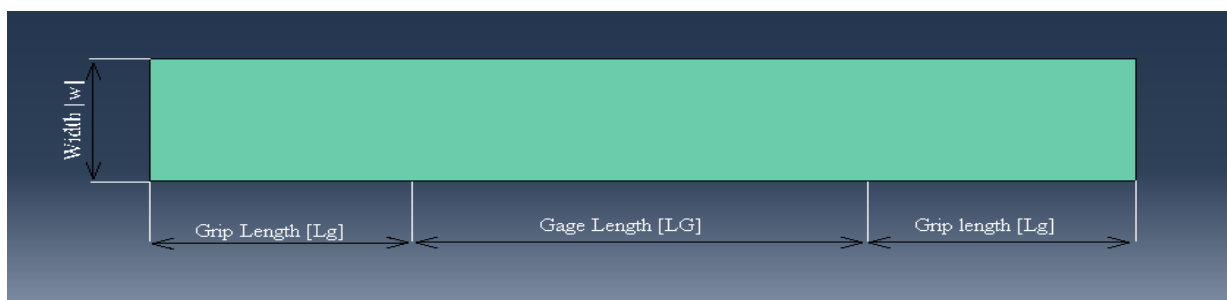
Figure 3-7: Tensile specimen abacus drawing

3.3.2. Tensile test procedure

The procedure started by setting the accessories on the machine, a step undertaken with the machine completely off. Two grip heads were mounted on the machine, one on the load cell and the other one on the bench of the machine. Pins locked the grip heads of the machine. The second step consisted of placing the specimen in the jaws of the grip heads and using the worm mechanism of the grip heads to tighten the specimen in the jaws without inducing stress or initiating cracks. Lock screws were turned such to lock the jaw within the axis of the load cell. The third step consisted of switching the UTM on, using the control monitor to set the control of the machine in manual mode and with the up/down button, pull the specimen to

align with the load cell axis. The fourth step consisted of setting up the machine; the horizon software is opened on the computer, the control monitor of the machine sets it in automatic mode, the correct standard is selected on the software, the dimensions of the specimen (gage length and thickness) were measured (Table 3.1) and stated on the software, the end of test was specified to 30% maximum load at fracture, and the outcome of the test was specified as load versus elongation. After these four steps have been completed, an overall check-up ensures that everything is in place before starting the test. The test was run under room temperature until fracture of the specimen was observed and the result was collected in the form of load-elongation data with relative curves. Data were exported in PDF and excel format. A flash USB was used to collect the data from the UTM computer for further analysis.

From the collected data, properties such as ultimate tensile strength, tensile strain, offset yield strength, offset strain, Young's modulus of elasticity, Poisson's ratio and post-fracture percentage elongation were computed. Equation 1 was used to compute the ultimate tensile strength and offset yield strength accordingly, where σ denotes the tensile stress expressed in MPa; P the applied load expressed in Newton; and A the cross-section area expressed in mm^2. Equation 2 was used for strain and offset strain, where ε is the tensile strain expressed in %; δ is the measured elongation expressed in mm; and L_G is the gage length expressed in mm. Equation 3 was used to compute Young's modulus, where E is the Young's modulus of elasticity expressed in GPa; $\Delta\sigma$ is the change in stress; and $\Delta\varepsilon$ the change in strain within the elastic region of the stress-strain curve.

$$\sigma = \frac{P}{A}$$ Equation 1: Ultimate tensile stress formula

$$\varepsilon = \frac{\delta}{L_G}$$ Equation 2: Ultimate tensile strain formula

$$\nu = -\frac{\varepsilon_{\text{lat}}}{\varepsilon_{\text{long}}}$$ Equation 3: Poisson's ratio formula

$$E = \frac{\Delta\sigma}{\Delta\varepsilon}$$ Equation 4: Young's modulus of elasticity formula

$$\%\delta = \varepsilon^{\text{ult}} - \frac{\sigma^{\text{ult}}}{E}$$ Equation 5: Percentage elongation formula

Equation 4 was used to compute the Poisson's ratio, where ν expressed in %, ε_{lat} is the lateral strain; and ε_{long} is the longitudinal strain. Equation 5 was used to compute the post-fracture percentage elongation, where $\%\delta$ is the percentage elongation; L_2 is the final length; and L_1 is the original length. The above formula were discussed by Norman E. Dowling in his book titled mechanical behavior of materials (Dowling, 2013).

3.3.3. Flexure test specimen preparation

Specimens' dimensions were obtained from the ASTM D-790 standard. Figure 3-9 illustrates the dimensioning of the specimen on abacus software. The Truecut shearing mechanical machine was used to trim the PCBs to sixteen specimens of rectangular shape with dimensions presented in Table 3-2. Figure 3-8 displays different flexure specimens: the FR-4_FT denotes the FR-4 specimen cut across the load-bearing fibres of the sample; FR-4_FL denotes the FR-4 specimen cut along the load-bearing fibres of the sample; MW_FT denotes the Mercurywave specimen cut across the load-bearing fibres; and MW_FL denotes the Mercurywave specimen cut along the load-bearing fibres.
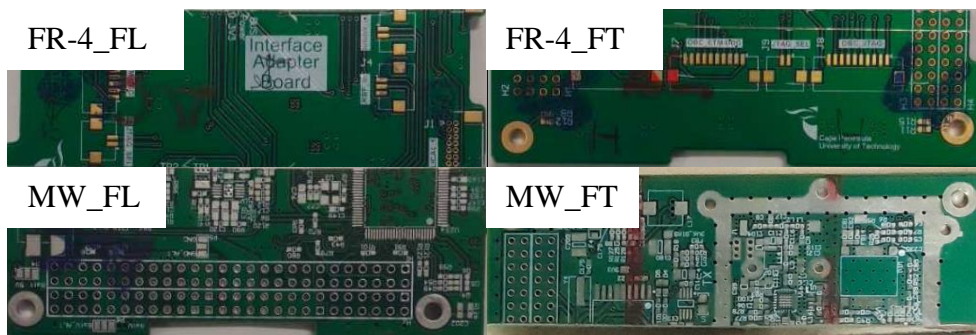
Figure 3-8: Flexure specimens

Table 3-2: Flexure specimens' dimensions expressed in mm

Sample	Specimen	Length	Support span	Load span	Width	Thickness
FR-4	0° fibres	96	76.8	38.4	28.95	1.574
	90° fibres	90	72	36	29.2	
Mercurywave	0° fibres	96	76.8	38.4	27.95	1.623
	90° fibres	90	72	36	28.63	
Flexure test	UTM load	Load range	Head speed	Deflection range	Strain-control

parameters	cell				
	200 kN	0 to 0.3 KN	2 mm/min	0 to 13 mm	0.58 mm/min

Figure 3-9: Flexure specimen abacus drawing

3.3.4. Flexure test procedure

The procedure began by setting the accessories on the Zwick Roell UTM with the machine completely off; a three-point bend fixture was mounted on the machine: one part constituting the loading nose was set on the load cell and the other constituting the support nose was set on the bench of the machine. A pin locked the loading nose on the load cell of the machine and screws fastened the base of the support noses on the bench using an Allen key. The support noses were set according to support span of the specimens. The second step consisted of switching the UTM on, then using the manual control monitor to bring the machine bench to a height of 1134.5 mm through the up/down button. The third step consisted of placing the specimen in the support noses and bringing the bench up so that specimen can be as close as possible to the loading noses. The fourth step consisted of setting up the machine: the testXpertII software is opened on the computer, the control monitor of the machine is used to set it in automatic mode, the correct standard is selected on the software, the dimensions of the specimen (support span, width and thickness) were measured (Table 3-2) and stated on the software, the end of test was specified to 30% maximum load at fracture, a preload of 10 N was set, and the outcome of the test was specified as load versus deflection. After these four steps were completed, an overall check ensured that everything is in place before starting the test. The test was run under room temperature until fracture of the specimen was observed and the result was collected in the form of load-deflection data with relative curves; these data were exported in excel format. A flash USB was used to collect the data from UTM computer for further analysis. From the collected data, properties such as bending stiffness,

bending strength, bending strain, bending yield strength, bending offset strain, flexure modulus of elasticity and deflection angle at fracture were computed. Equation 6 was used to compute for the bending stiffness, where k denotes the bending stiffness expressed in N/mm; F denotes the applied load expressed in N; and d denotes the deflection recorded at fracture expressed in mm. Equation 7 was used to compute for the bending strength and bending yield strength accordingly, where σ_f denotes the flexure stress expressed in MPa; F denotes the applied load expressed in N; w denotes the width expressed in mm; t denotes the thickness expressed in mm; and L denotes the support span. Equation 8 was used to compute for flexure strain and flexure offset strain, where ε_f is the flexure strain expressed; and the other parameters are as described above. Equation 9 was used to compute the flexure modulus of elasticity, where E_f is the flexure modulus of elasticity expressed in GPa; $\Delta\sigma_f$ is the change in flexure stress; and $\Delta\varepsilon_f$ the change in flexure strain within the elastic region of the stress-strain curve. Equation 10 was used to compute for the deflection angle at fracture, where β denotes the deflection angle at fracture expressed in degrees; the other parameters are the same as described above.

$$k = \frac{F}{d}$$ Equation 6: Bending stiffness formula

$$\sigma_f = \left(\frac{3FL}{2wt^2}\right)\left[1 + 6\left(\frac{d}{L}\right) - 4\left(\frac{t}{L}\right)\left(\frac{d}{L}\right)\right]$$ Equation 7: Flexure stress formula

$$\varepsilon_f = \frac{6dt}{L^2}$$ Equation 8: Flexure strain formula

$$E_f = \frac{\Delta\sigma_f}{\Delta\varepsilon_f}$$ Equation 9: Flexure modulus of elasticity

$$\beta = \frac{2d}{L}$$ Equation 10: Deflection angle at fracture

$$\overline{X} = \text{AVERAGE}(X_1 : X_2) \text{ or } \overline{X} = \sum \frac{X}{n}$$ Equation 11: Arithmetic mean formula

$$S = \text{STDEV.P}(X_1 : X_2) \text{ or } S = \sqrt{\frac{(\sum X^2 - n\overline{X}^2)}{(n-1)}}$$ Equation 12: Standard deviation formula

The statistical characteristics of the properties computed will be evaluated on excel. The arithmetic mean was computed using Equation 11 and the standard deviation was computed using Equation 12.

3.4.Fractography analysis

Fracture surface analysis of the failed samples was subjected to both the tensile and flexure stress. Sample preparation and the microscopic analysis procedure are described below.

3.4.1. Sample preparation

The dimensions of the samples were determined based on the specification of the microscope Nikon SMZ 25_18 manual. The height of the samples was defined in function of the lowest working distance of the objectives, which is 20 mm. The Truecut shearing mechanical machine trimmed the specimens to a rectangular shape with dimensions presented in Table 3-3.

Table 3-3: Microscopic analysis sample parameter

Sample	Specimen	Length	Width	Thickness
FR-4 and Mercurywave	0° fibres	10 mm	10 mm	1.574 and 1.623 mm
	90° fibres	10 mm	10 mm	

3.4.2. Microscopic analysis procedure

The microscopic analysis was done under diascopy illumination according to the following steps: *Step one* consisted of switching the microscope on by turning on the P2-CTLA control box by pressing the power switch button. *Step two* consisted of starting the computer, opening the NIS Elements and adjusting all settings for the software reading for the analysis. *Step three* consisted of setting the sample on the stage plate right below the objective. *Step four* consisted of bringing the objective in line with the optical trajectory. *Step five* consisted of turning on illumination through the remote brightness control selection switch and adjusting the brightness for a proper view of the sample. *Step six* consisted of adjusting the focus using the focus knobs. *Step seven* consisted of changing the magnification using the zooming button from the P2-RC remote controller. *Step eight* consisted of capturing the image using the NIS element, with quality of capture managed through the real time EDF function of the software. *Step nine* consisted of saving the data on the computer and

collecting the data using a flash USB. *Step ten* consisted of switching off the machine after completion of the analysis.

4. RESULTS

From the experimental tests conducted on the two samples, FR-4 and Mercurywave substrate PCB, stress-strain curves of each specimen tested to tensile and bending stress were drawn and evaluation of tensile and bending properties of each sample are analysed in this chapter. This chapter will begin by analysing the mechanical properties of the samples tested to tensile stress, then bending stress, and then will conclude with post-fracture analysis of the fractured samples.

4.1. Tensile test result

The FR-4 and Mercurywave samples were tested to tensile stress; 12 specimens per sample were tested: six along and six across the axis of their load-bearing fibres. This section started by evaluating the tensile properties of the FR-4 sample and that of the Mercurywave sample followed right after.

4.1.1. Tensile properties of FR-4 sample tested along the axis of load-bearing fibres

Figure 4-1 shows stress-strain curves of the FR-4 sample tested along the axis of the load-bearing fibres. The acronym FR-4 stands for FR-4 specimen, and the letter L denotes the stress applied along the axis of the load-bearing fibres. Figure 4-2 (appendix A) shows specimens fractured in different regions: specimen 1 (L1) has failed just below the grip jaw, where three holes of different diameters were noticed, constituted a zone of high stress concentration; specimen 2 (L2) has failed within the gage length; specimen 3 (L3) has failed within the gage length with the failure identified as initiated in a region where holes are noticed and progress in a short angular shape before extending linearly; specimen 4 (L4) has failed right below the grip jaw where the fracture was noted as initiated from a high stress concentration zone where holes are noticed and propagated in an angular shape following a path filled with holes; specimen 5 (L5) also has failed right below the grip jaw where the fracture has been initiated from a set of holes, then propagated along the width of the specimen; and specimen 6 (L6) has failed at the midsection of the gage length in a region where holes are noticed along its width. The curves of Figure 4-1 displayed the reaction of each specimen or the rate at which each specimen elongated under the application of tensile stress. Properties such as ultimate tensile strength, ultimate tensile strain, offset yield

strength, post-fracture percentage elongation, Young's modulus and Poisson's ratio were deducted from these curves and presented below.
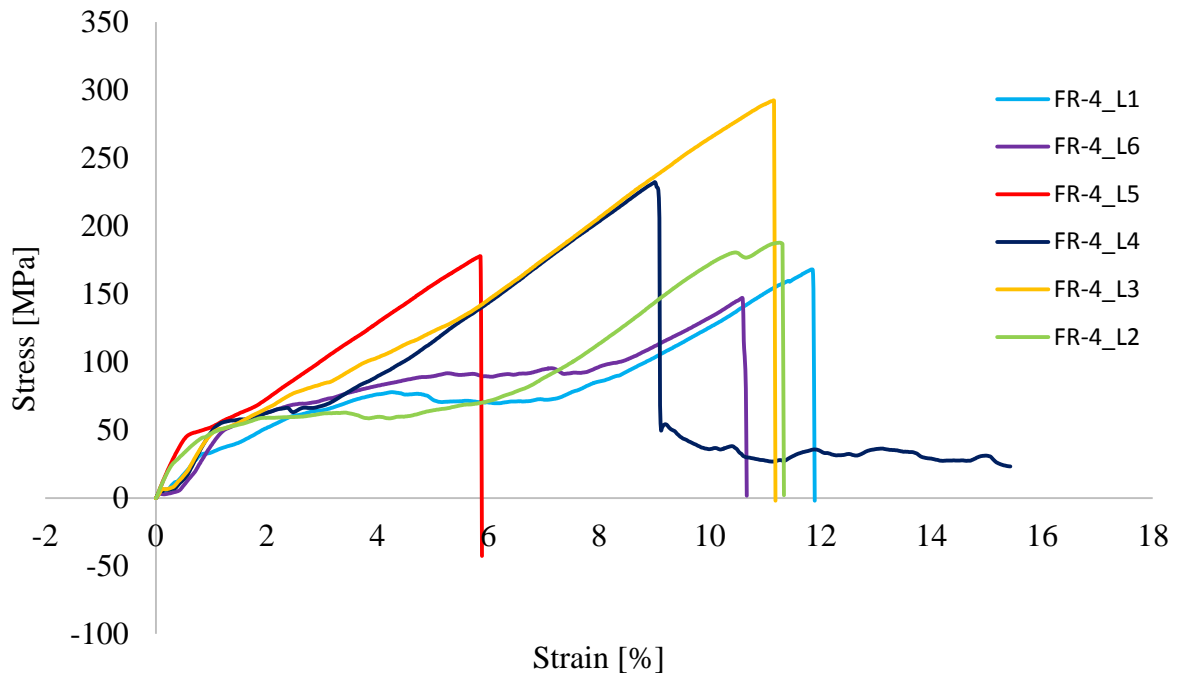
Figure 4-1: Stress-strain curves of the FR-4 sample tested along the axis of load-bearing fibres

L1   L2   L3   L4   L5   L6
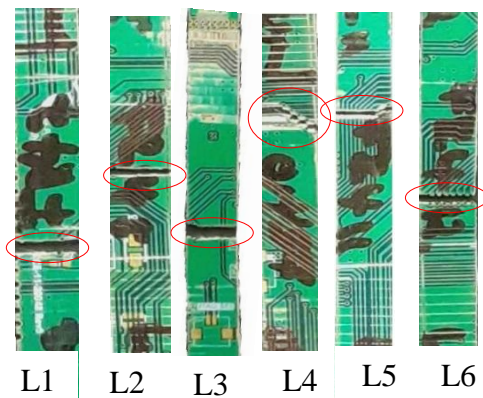
Figure 4-2: Fracture FR-4 specimen tested along the 0° fibre axis

➤ **Toe correction**

The stress-strain curve in Figure 4-3 illustrated the behaviour of the FR-4 specimen tested along its load-bearing fibres. Three points depicted on the curve described four stages through which the specimen progressed while subjected to tensile stress. The first stage, a zone described as toe on the curve, represents a region on the strain axis between point zero

26

and the intersection of the slope of the elastic region's tangent to the strain axis where no specimen's property is defined. This was a stage where the specimen aligns within the axis of the applied load and represents an artifact generated by the take-up of the slack. Therefore, for an exact determination of different mechanical properties of the specimen, a correction should be made to account for this 'no property' region by substituting the zero strain by the size of the toe. The second phase is the elastic zone which determined the linear elongation of the specimen, a phase during which if the stress is removed, the specimen will retrieve its initial shape. The third phase is the transition zone, illustrating the extent of combined elastic-plastic deformation experienced by the specimen right before fracture occurs. Fracture is the fourth and final phase displayed by the curve above which also represents the point at which specimen failed under the application of tensile stress.
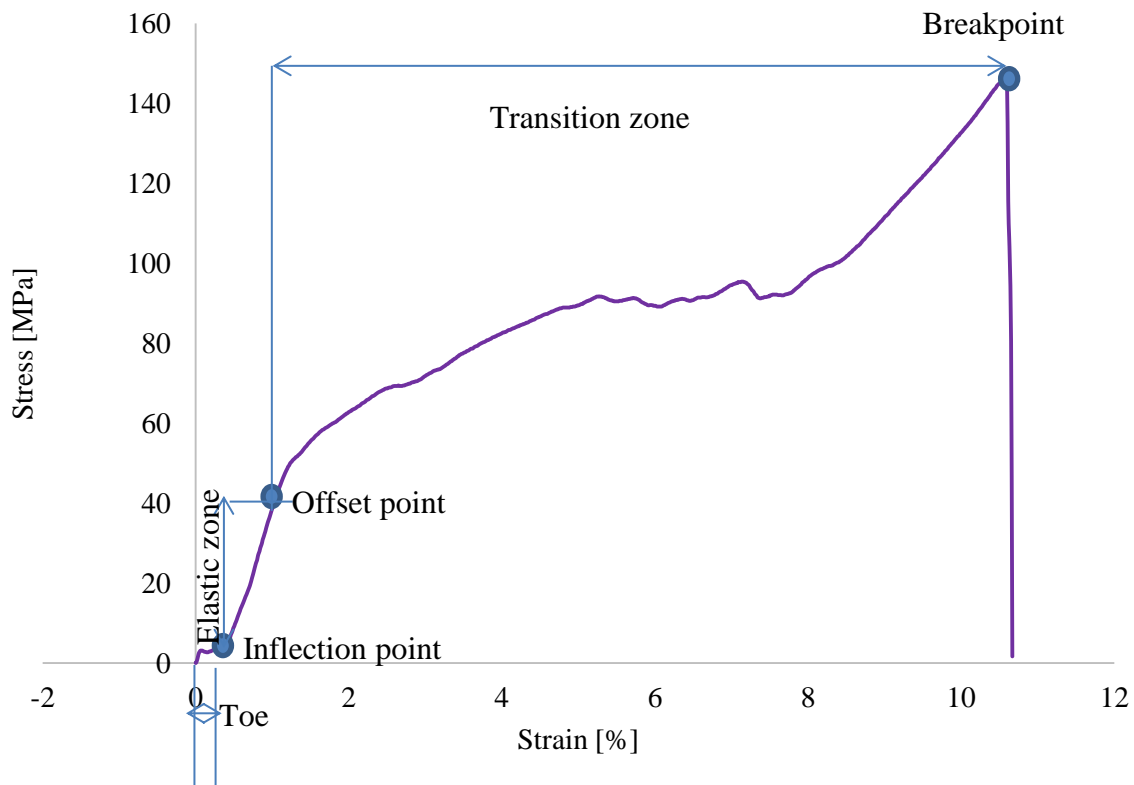
Figure 4-3: Toe correction for the specimen tested along the 0° fibre axis

➢ **Offset tensile yield strength**

Analysis of the curves of Figure 4-1 of section 4.1.1 illustrates the points on the curve where deviations in strain from the linear deformation occurred. Figure 4-4 shows offset yield strengths of different specimens evaluated at different offset strains, as illustrated in Figure 4-

27

5. Figure 4-4 shows that L4 has the highest offset yield strength and L6 the lowest. The mean yield strength was found to be 33.188 MPa with a standard deviation of 10.4632 at an offset

	L1	L2	L3	L4	L5	L6
εO [%]	0.7	0.3	0.6	0.4	0.4	0.4

Figure 4-4: Offset strain

	L1	L2	L3	L4	L5	L6
σy [MPa]	31.4	23.1	39.4	50.9	35.1	19.2
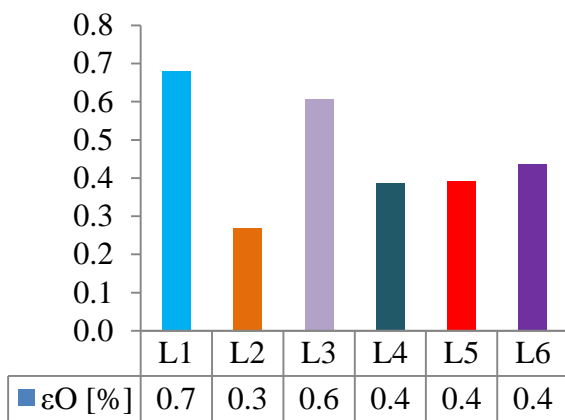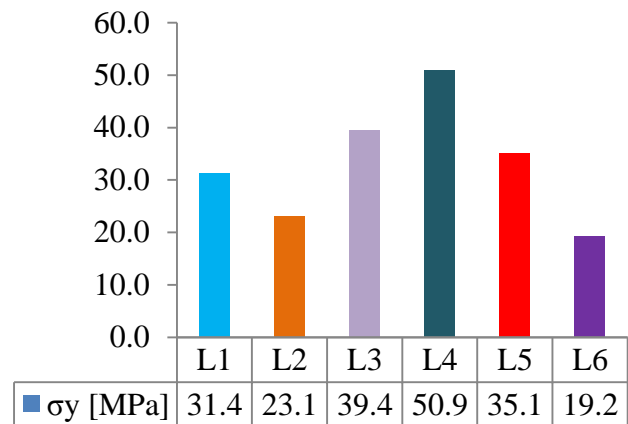
Figure 4-5: Offset yield strength

strain of 0.4615% with a standard deviation of 0.1397. The analysis showed that the first deviation from the linear deformation of the FR-4 sample tested along the 0° fibres occurred at different stresses and with different offsets because of the complex localised structural configuration of each region of the sample: the L4 region did elastically deform more but plastic deformation was initiated from the L2 region.

➢ **Ultimate tensile strength**

Figure 4-1 of section 4.1.1 shows that all specimens did not yield the same ultimate tensile strength or maximum stress, and Figure 4-2 shows that the failure did not occur in the same way or in the same region in all six specimens. Instead, each specimen broke at specific stresses, in a specific way, and due to the localised structure of that specific region of the specimen where the stress concentration was high. Figure 4-6 shows different measured maximum stresses. It shows that; L3 has the highest ultimate strength and L6 has the lowest, a mean ultimate strength of 200.90 MPa with a standard deviation of 48.3619 was computed. The high standard deviation shows that the rate of localised stress concentration in the specimen was irregular, with failure occurred at different strengths. This proved the highly heterogeneous nature of the composite material where the embedded copper foil and drilled holes present on the laminate reduced the strength of the sample at localised region and constitute a weak region of the sample. It was from there that the failure of the sample subjected to tensile stress along the load-bearing fibres did occurred.

➢ Ultimate tensile strain

The analysis of stress-strain curves in Figure 4-3 in section 4.1.1 shows that the specimens obtained from the very same sample broke at different strain rates, as seen in Figure 4-7. Figure 4-7 shows that L1 displays a high strain and L5 has the lowest; the mean ultimate strain was found to be 9.8201% with a standard deviation of 1.9909. This confirmed that when subjected to tensile stress, a certain region of the sample elongated significantly more than the others because some parts of the sample were more complex than others. Figure 4-2 shows different outer structural configurations of the specimens that influenced the extent to which they elongated.

	L1	L2	L3	L4	L5	L6
■ εUlt [%]	11.7	11.3	10.9	8.8	5.9	10.3
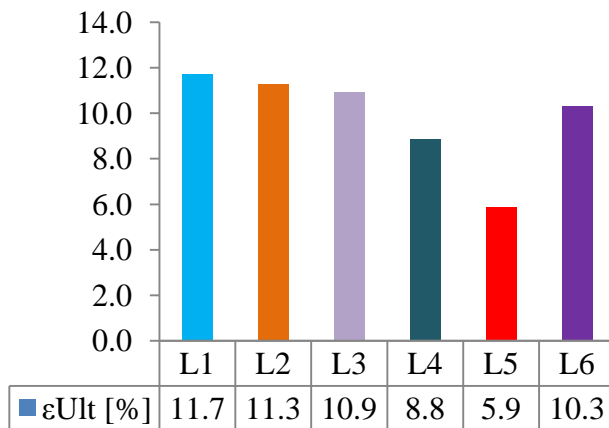
Figure 4-6: Ultimate tensile strain

	L1	L2	L3	L4	L5	L6
■ σ [MPa]	168.0	187.7	292.4	232.3	177.8	147.1
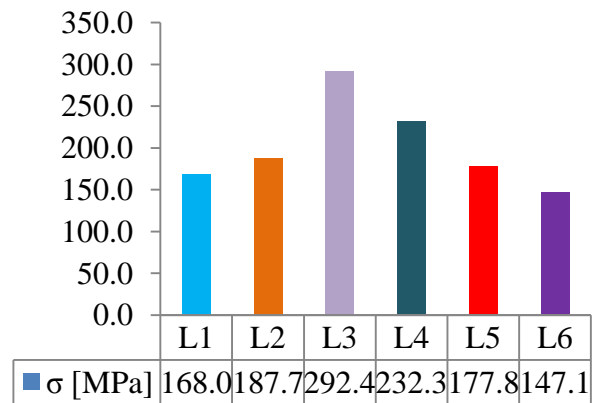
Figure 4-7: Ultimate tensile strength

➢ Young's modulus of elasticity

Analysis of Figure 4-3 of section 4.1.1 illustrates the extent of the linear or elastic deformation of the FR-4 sample tested along its load-bearing fibres; from it, Young's modulus of elasticity was computed. This property defined the extent to which the sample initially deformed before the first point of change in strain without relative change in stress had occurred. Figure 4-9 shows Young's modulus of elasticity of different specimens deducted from Figure 4-1 of section 4.1.1. it is seen that L2 has a high Young's modulus and L1 has the lowest. The mean Young's modulus was determined as 6.7787 GPa with a standard deviation of 1.5639, which confirmed that for the very same sample, some regions elastically deformed more than other regions while subjected to tensile stress because of the complexity of the structural configuration of the sample. As each fractured specimen shown in Figure 4-2 looks different, so its elastic behaviour was different.

➢ Poisson's ratio

The lateral deformation relative to longitudinal deformation of the sample was computed for each tested specimen. Figure 4-10 displays values of different computed Poisson's ratios; the analysis of Figure 4-10 verified that each specimen yielded a specific Poisson's ratio. L5 had the highest Poisson's ratio and L6 the lowest. The mean Poisson's ratio was computed to 0.8836% with a standard deviation of 0.0347. This showed that the lateral deformation of the sample was not proportional to that of the longitudinal deformation and certain regions of the sample did deform in both the longitudinal and transversal direction more than others when the sample was subjected to tensile stress applied along the load-bearing fibres. Figure 4-2 shows that the structural configuration of the sample did not allow it to react homogeneously, but each region reacted according to its specific localised structural configuration.

	L1	L2	L3	L4	L5	L6
■ E [GPa]	4.5	9.4	6.4	7.6	5.6	7.2
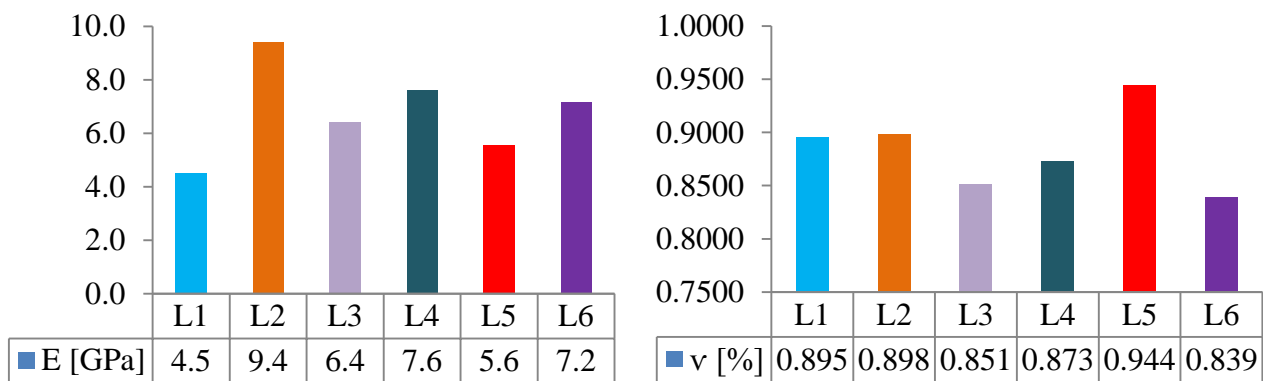
Figure 4-9: Young's modulus of elasticity

	L1	L2	L3	L4	L5	L6
■ v [%]	0.895	0.898	0.851	0.873	0.944	0.839

Figure 4-8: Poisson's ratio

➢ **Post-fracture percentage elongation**

The evaluation of the extent to which the sample stretched under plastic deformation is an

	L1	L2	L3	L4	L5	L6
■ %δ	11.7	11.3	10.9	8.8	5.8	10.3
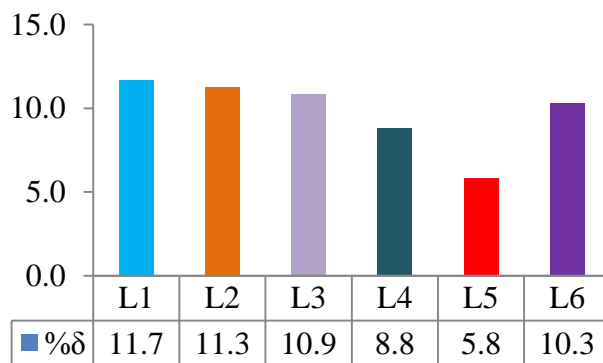
Figure 4-10: Post fraction percentage elongation expressed in percentage

important parameter for determining whether a sample was ductile or brittle. Figure 4-8 provides different post-fracture percentage elongations computed from the analysis of the

curves in Figure 4-1 of section 4.1.1. The analysis showed that L1 yielded the highest plastic deformation and L5 the lowest. The mean post-fracture percentage elongation was found to be 9.7891% with a standard deviation of 1.9906. As illustrated in Figure 4-3 of section 4.1.1, the plastic deformation of each specimen was highly affected by the localised structural configuration of the boards.

4.1.2. Tensile properties of FR-4 sample tested across the axis of load-bearing fibres

Figure 4-11 presents details of the stress-strain curve of the sample tested across the 0° fibres. Figure 4-12 shows six specimens cut from the very same sample and tested across the axis of its load-bearing fibres. The analysis of Figure 4-12 (Appendix A) shows a specimens
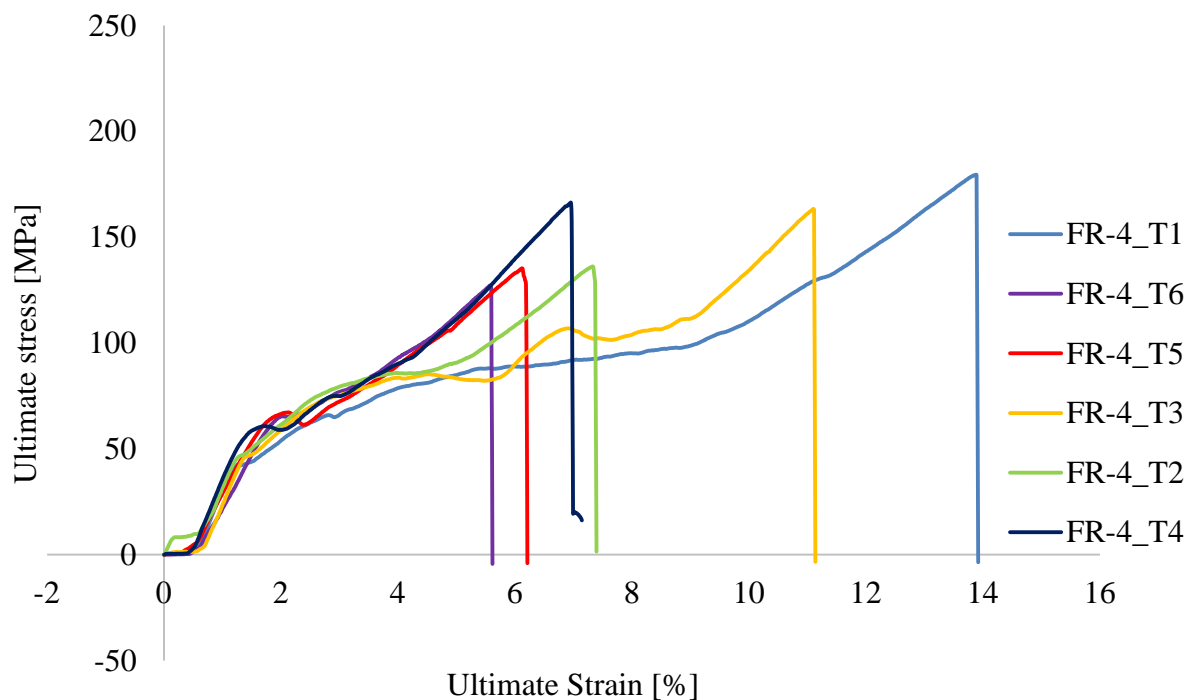
Figure 4-11: Stress-strain curves for the specimens tested across the axis of load-bearing fibres

fractured in different regions of the gage length: specimen 1 (T1) failed within the centre of its gage length; specimen 2 (T2) also failed within the centre its gage length; specimen 2 (T3) failed away from the centre of the gage length; specimen 4 (T4) fracture was propagated in a combined linear and angular shape within its gage length; specimen 5 (T5) failed within its gage length in a nonlinear shape; and specimen 6 (T6) failed within the upper region

31

of its gage length. Properties such as ultimate tensile strength, ultimate tensile strain, offset yield strength, Young's modulus and Poisson's ratio of different specimens, derived from the analysis of curves in Figure 4-11, are presented in the below sections.
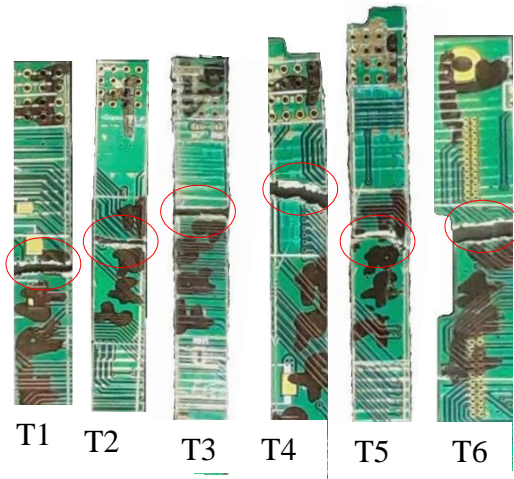
Figure 4-12: Fractured FR-4 specimen tested across the 0° fibre axis

➢ **Toe correction**

Figure 4-13 describes the behaviour of the FR-4 sample tested across the load-bearing fibres. The detailed explaination provided in section 4.1.1 applies to this section.
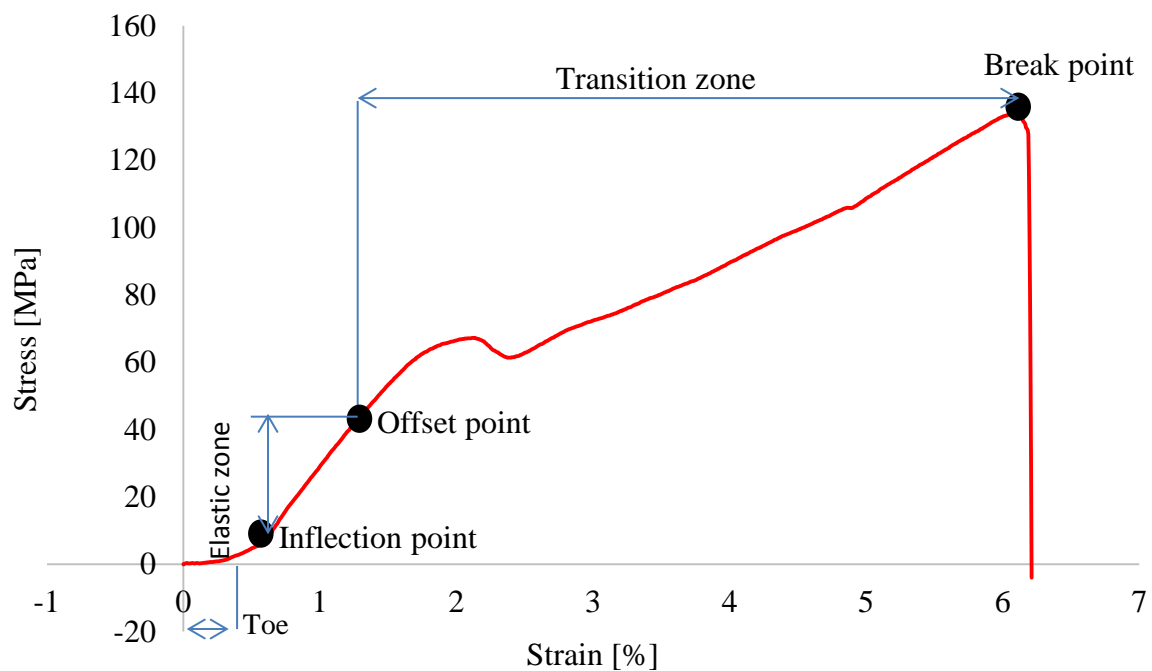
Figure 4-13: Toe correction for the FR-4 specimen tested across the 0° fibre axis

➤ Offset tensile yield strength

Analysis of Figure 4-13 showed the extent of linear deformation or the point at which the first deviation of the strain from the linear deformation had occurred at different strains relating to different stresses. Figure 4-15 shows different offset points identified on the curves of Figure 4-11 from which the offset yield strength of different specimens was measured, as illustrated in Figure 4-14. Analysis of Figure 4-14 shows that T5 deviated at the highest offset point corresponding to the highest offset yield strength and T6 had the lowest offset yield strength. The mean yield strength was computed t 41.1586 MPa with a standard deviation of 7.0301, at a mean offset strain of 0.7002% with a standard deviation of 0.1589. This confirmed that each specimen yielded at a specific stress and with a specific offset rate showing that the FR-4 sample subjected to tensile stress applied across its load-bearing fibres did deform elastically at a different rate. This rate was a function of the localised structural configuration of the sample.

	T1	T2	T3	T4	T5	T6
■ εO [%]	0.6	0.6	0.6	0.8	1.0	0.6
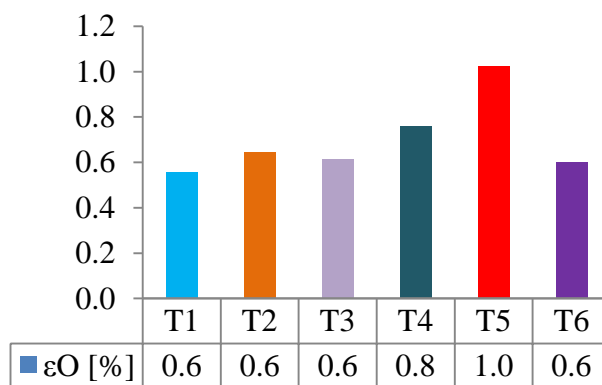
Figure 4-15: Offset strain expressed

	T1	T2	T3	T4	T5	T6
■ σy [MPa]	37.4	41.1	40.3	47.2	51.5	29.4
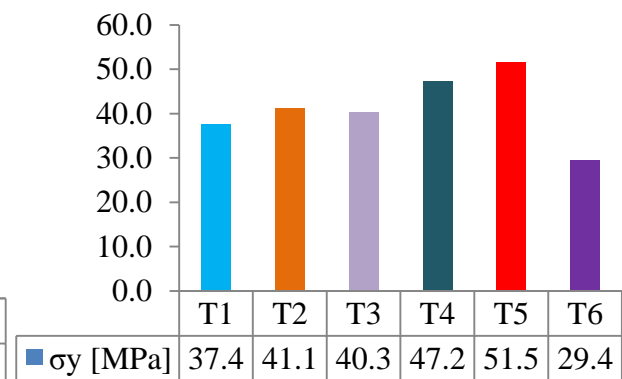
Figure 4-14: Offset yield strength

➤ Ultimate tensile strength

Figure 4-11 of section 4.1.2 showed that, as for the FR-4 sample tested along the axis of load-bearing fibres, the specimens did not all break at the same stress; each specimen yielded a specific ultimate strength. As seen in Figure 4-17, T1 had the highest ultimate strength and T6 the lowest. The mean ultimate strength was found to be 151.31MPa with a standard deviation of 0.1589. The standard deviation shows that the rate at which the strength of the sample changes as a function of its structural configuration (illustrated in Figure 4-12) was

not very high. It was primarily affected by the presence of holes within the localised region of the sample.

➢ **Ultimate tensile strain**

The analysis of stress-strain curves in Figure 4-11 of section 4.1.2 showed that the specimens obtained from the same sample broke at a different strain rate. Figure 4-16 shows that T1 had the highest ultimate strain and T6 the lowest. The mean ultimate strain was found to be 7.9758% with a standard deviation of 2.9479. This proved that when subjected to tensile load, a certain region of the sample did elongate significantly more than the others because some

	T1	T2	T3	T4	T5	T6
■εUlt [%]	13.3	6.8	10.5	6.5	5.7	5.0
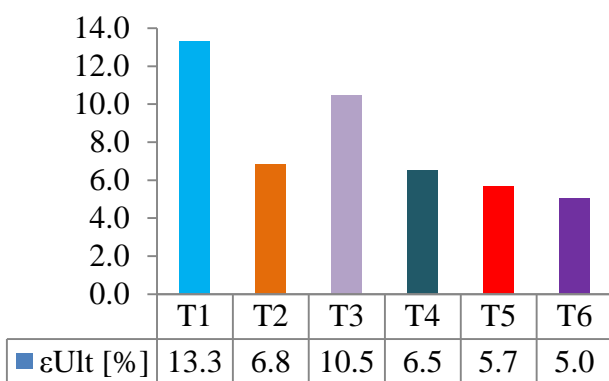
Figure 4-16: Ultimate tensile strain

	T1	T2	T3	T4	T5	T6
■σ [MPa]	179.5	136.2	163.4	166.4	135.3	127.3
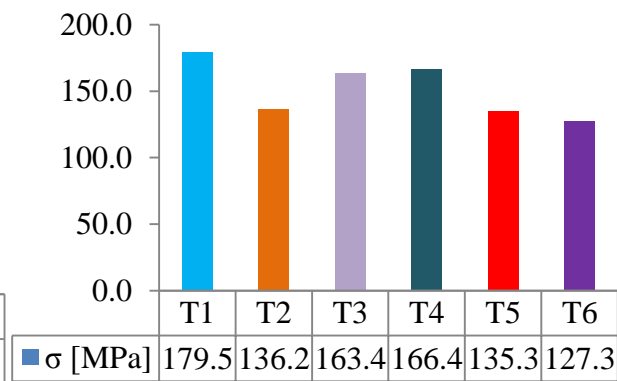
Figure 4-17: Ultimate tensile strength

parts of the sample were more heterogeneous than others.

➢ **Young's modulus of elasticity**

Analysis of Figure 4-13 of section 4.2.1 illustrated the extent of the linear or elastic deformation of the sample tested across the axis of load-bearing fibres. Figure 4-19 shows Young's modulus of elasticity of different specimens obtained from the same sample; T2 had

	T1	T2	T3	T4	T5	T6
■E [GPa]	6.8	8.8	5.3	5.9	4.1	7.1
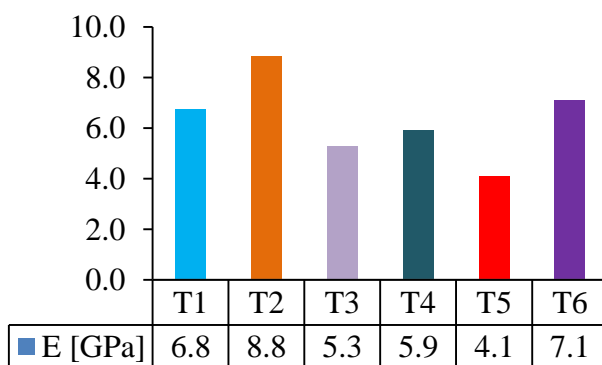
Figure 4-19: Young's modulus of elasticity

	T1	T2	T3	T4	T5	T6
■ν [%]	0.8	0.7	0.8	0.8	0.7	0.6
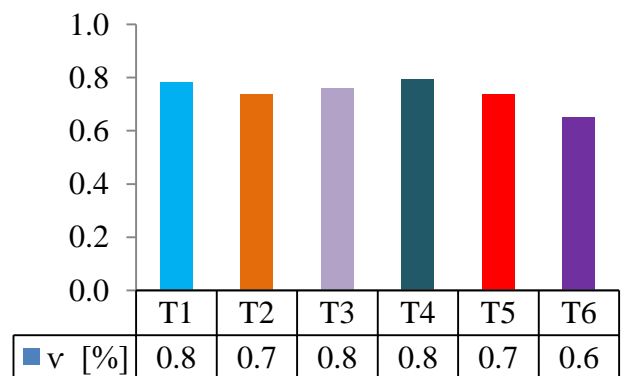
Figure 4-18: Poisson's ratio

the highest Young's modulus of elasticity and T5 the lowest. A mean of 6.3348 GPa with a standard deviation of 1.4830 was computed. The results obtained confirmed that for the very same sample, some regions were highly elastic compared to others while subjected to tensile stress applied across its load-bearing fibres, for the same reason as those given in section 4.1.1.

➤ **Poisson's ratio**

Figure 4-18 displays the Poisson's ratio computed for each tested specimen; it showed that for each specimen a specific Poisson's ratio was found. T3 had the highest Poisson's ratio and T6 the lowest. The mean Poisson's ratio was noted as 0.7451% with a standard deviation of 0.0476 showing that the lateral deformation of the sample was not proportional to that of the longitudinal deformation and certain regions of the sample did deform in both the longitudinal and transversal direction more than others when the sample was subjected to tensile stress applied across the 0° fibres. This implied that the structural configuration of the sample did not allow the sample to react symmetrically, but each region reacted according to its specific structural configuration.

➤ **Post-fracture percentage elongation**

Figure 4-20 shows different post-fracture percentage elongations computed from the analysis of the curves of Figure 4-11 of section 4.1.2. Analysis showed that T1 yielded the highest plastic deformation and T6 the lowest.

	T1	T2	T3	T4	T5	T6
■%δ	13.3	6.8	10.4	6.5	5.7	5.0
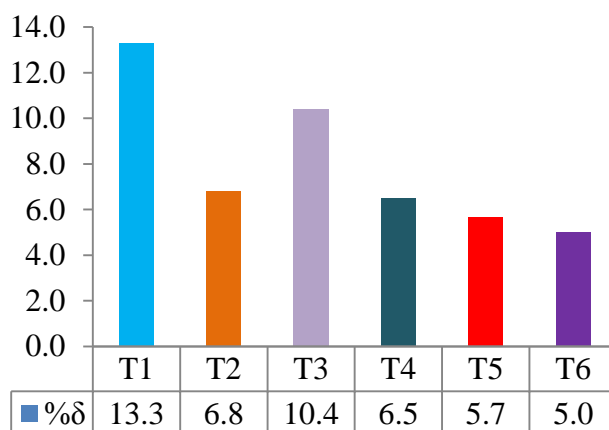
Figure 4-20: Post-fracture percentage elongation

The arithmetic mean computed was found to be 7.9505% with a standard deviation of 2.9505 showing that each specimen elastically deformed at a different rate before fracture.

4.1.3. Tensile properties of Mercurywave sample tested across the axis of load-bearing fibres

Figure 4-22 (Appendix A) shows the Mercurywave specimens tested across the load-bearing fibres: specimen 1 (T1) failed within its gage length in a nonlinear shape; specimen 2 (T2) failed below the grip jaw and failure was initiated from a hole and propagated along the width of the specimen; specimen 3 (T3) failed right below the grip jaw in a nonlinear shape; specimen 4 (T4) failed right below the grip jaw also in a nonlinear shape; specimen 5 (T5) failed within its gage length in a nonlinear shape; and specimen 6 (T6) failed within its gage length and failure was observed to have been initiated from the holes present in the failure region. The stress-strain curves of Figure 4-21 illustrated the reaction of each specimen to tensile stress. Same properties as those presented in section 4.1.2 deducted from the analysis of these curves are presented below.
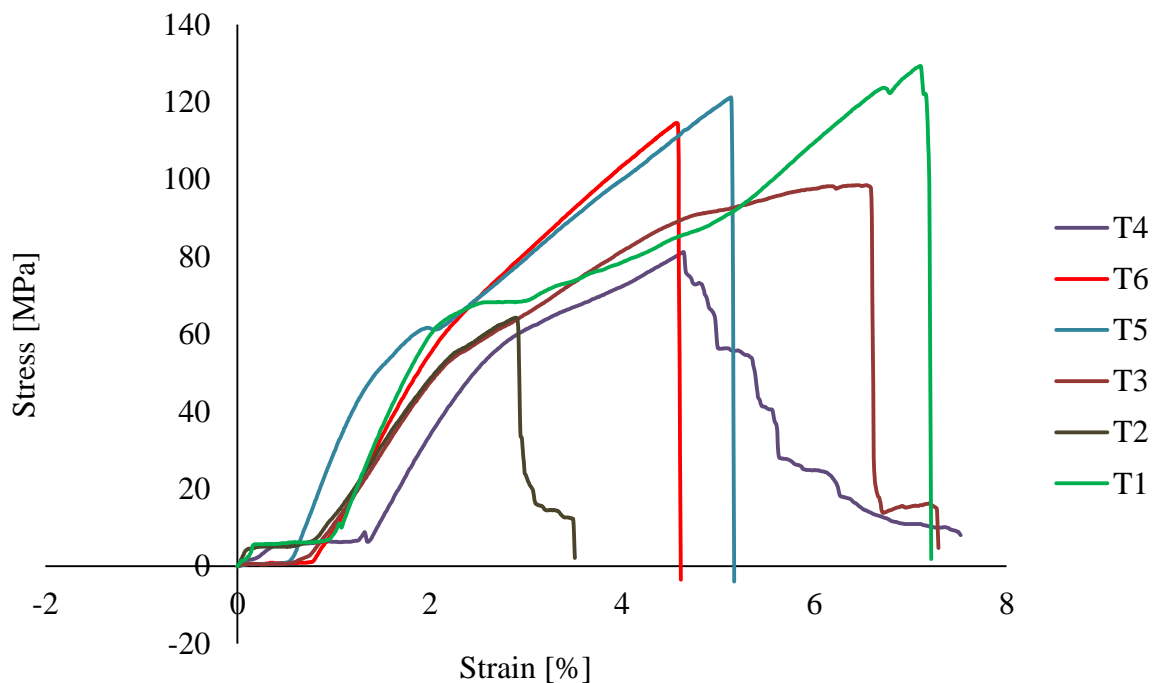
Figure 4-21: Stress-strain curves of the Mercurywave specimens tested across the 0° fibres axis
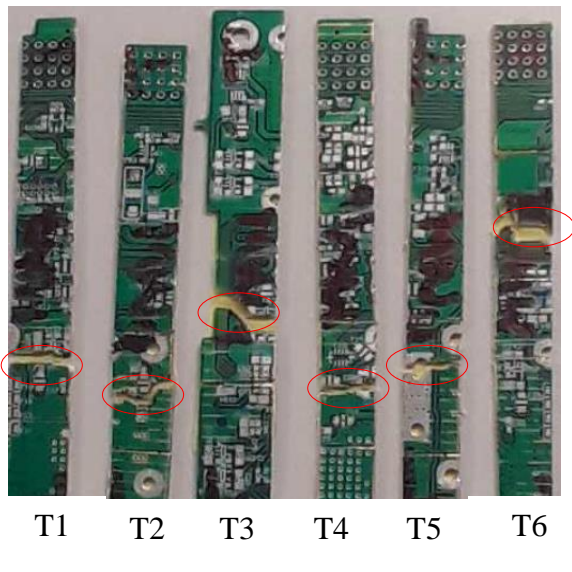
Figure 4-22: Mercurywave specimen tested across the 0⁰ fibres axis

> **Toe correction**

Figure 4-23 presents a detailed description of the reaction of the Mercurywave sample tested along the 0° fibres. The explanation in section 4.1.1 applied to this section as well.
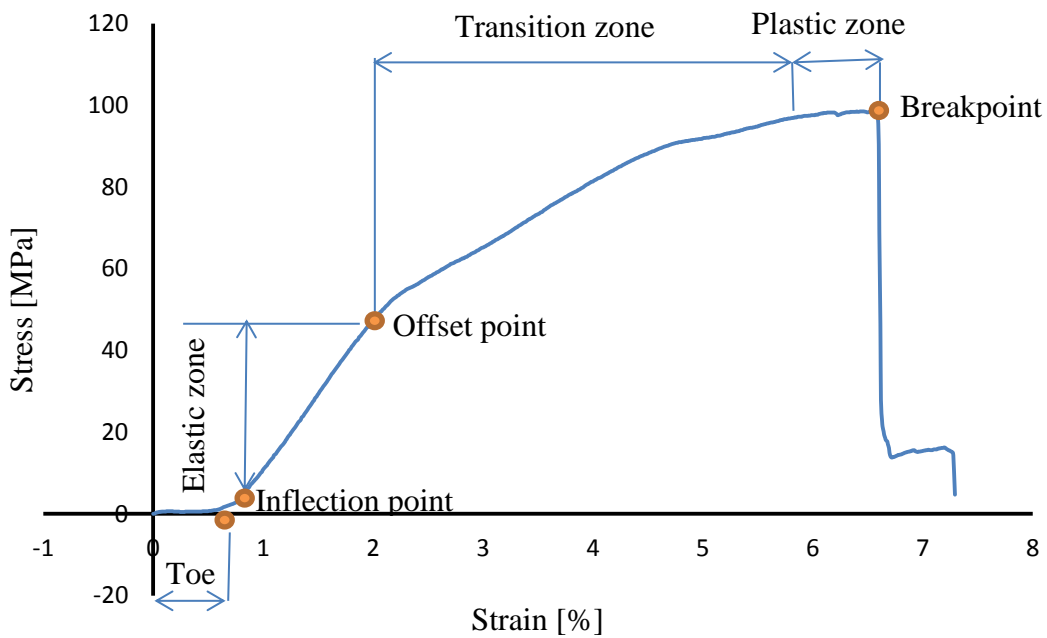
Figure 4-23: Toe correction for the Mercurywave specimen tested across the 0° fibre axis

> **Offset tensile yield strength**

Analysis of the curves of Figure 4-21 above showed deviations in strain from the linear deformation occurring at different stresses and strains.

The analysis of Figures 4-24 and 4-25 shows that T1 had the highest offset yield strength and T2 the lowest. The mean yield strength was 35.2070 MPa with a standard deviation of 6.0160 at a mean offset strain of 0.7411% with a standard deviation of 0.1152, showing that each part of the sample did yield at its specific strain and stress.

	T1	T2	T3	T4	T5	T6
■ εO [%]	0.7	0.7	0.9	0.8	0.5	0.8
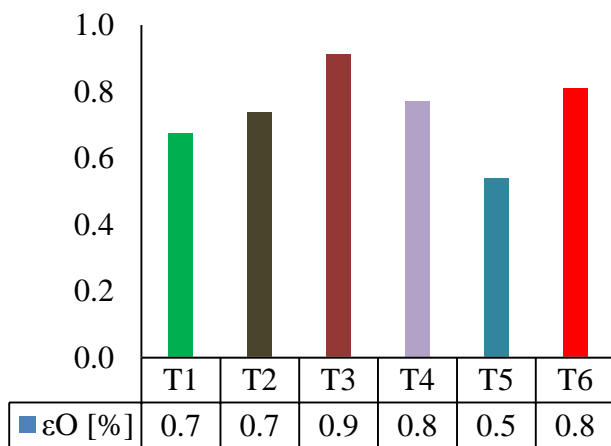
Figure 4-24: Offset strain

	T1	T2	T3	T4	T5	T6
■ σy [MPa]	45.3	25.3	32.1	37.0	34.3	37.2
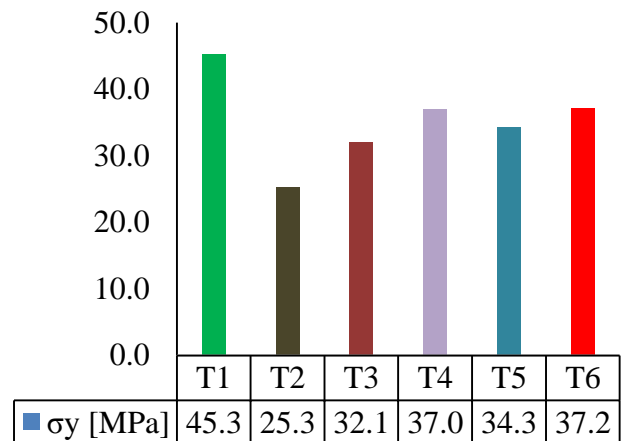
Figure 4-25: Offset yield tensile strength

➢ **Ultimate tensile strength**

Figure 4-21 of section 4.1.3 showed that all specimens did not produce the same ultimate tensile strength or maximum stress; instead, each sample broke at a specific stress. Figure 4-26 shows the difference in the recorded stresses at fracture: T1 had the highest ultimate strength and T2 the lowest. The mean ultimate tensile strength was computed as 01.4855 MPa with a standard deviation of 22.8806. The standard deviation suggested a high rate in the different ultimate strengths measured across the 0° fibres of the sample. Holes of different diameters noticed in a localised region of the sample and its non-homogeneous nature were found to be major factors that influence the irregularity in the strength of the sample opposed to the application of the load, as illustrated in Figure 4-22.

➢ **Ultimate tensile strain**

The analysis of stress-strain curves of Figure 4-21 in section 4.1.3 showed that the specimens obtained from the very same sample broke at different strain rates. Figure 4-27 shows that T2 had the largest strain and T4 the lowest. The mean ultimate strain was determined to be 5.0561% with a standard deviation of 1.2057, suggesting that when subjected to tensile stress,

the deformation of the sample was irregular: some parts elongated much more than the others because of the complex nature of the sample (Figure 4-22).

	T1	T2	T3	T4	T5	T6
σult [MPa]	129.3	64.2	98.5	81.2	121.2	114.6

Figure 4-27: Ultimate tensile strength

	T1	T2	T3	T4	T5	T6
εUlt [%]	6.2	6.5	5.9	3.4	4.6	3.7
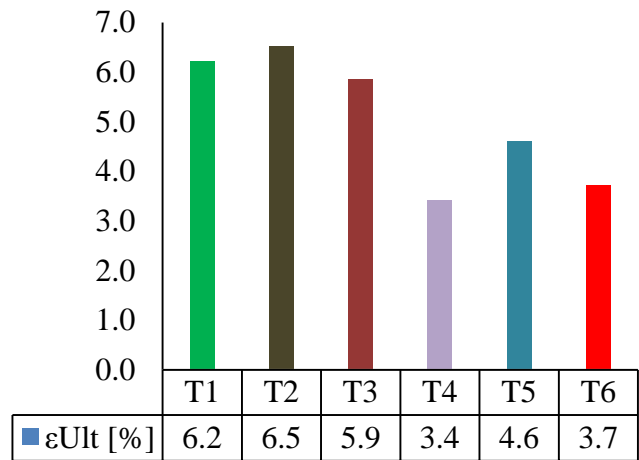
Figure 4-26: Ultimate tensile strain

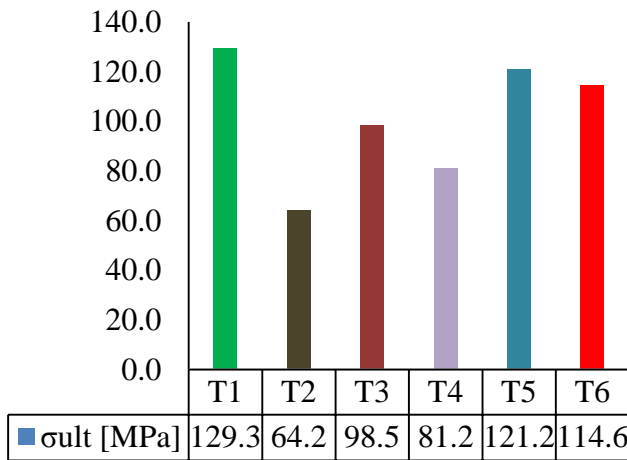➢ **Young's modulus of elasticity**

Analysis of Figure 4-23 of section 4.1.3 displayed the extent of elastic behaviour of the specimen tested across the 0° fibres. According to the analysis of Figure 4-21, Young's modulus of elasticity of each tested sample was computed. Figure 4-30 shows Young's modulus of elasticity of different specimens obtained from the same sample, with results showing that T2 had the highest Young's modulus of elasticity and T3 the lowest. The mean Young's modulus of elasticity computed from the tested sample was noted as 5.6407 GPa and a standard deviation was computed to 1.1317. The standard deviation showed once again that the rate of elastic deformation within the sample was irregular. This can be explained by the fact that the elastic deformation of the sample was influenced by the localised material structure.

➢ **Poisson's ratio**

Figure 4-29 showed that each specimen yielded a specific Poisson's ratio. T4 had the highest Poisson's ratio and T2 the lowest. The mean Poisson's ratio was found to be 0.9520% and a standard deviation of 0.0109. The standard deviation computed showed that the rate of change in Poisson's ratios computed for different parts of the sample was almost equal. But the non-homogeneous nature of the sample was again proven in the fact that the lateral deformation of the sample was not proportional to that of the longitudinal deformation.

➢ **Post-fracture percentage elongation**

39

The evaluation of the extent to which the specimen stretched under plastic deformation was computed, with Figure 4-28 presenting different post-fracture percentage elongations for each specimen. It was evident that specimen T2 yielded the highest plastic deformation and specimen T4 the lowest. The mean post-fracture percentage elongation was found to be 5.0374% and a standard deviation of 1.2067, demonstrating that the rate of change in plastic deformation of the sample was also irregular. This property shows that the structural configuration of the sample differs from one point to another, so the plastic deformation is influenced by this aspect.

	T1	T2	T3	T4	T5	T6
■ E [GPa]	5.5	7.3	4.2	4.4	6.8	5.7
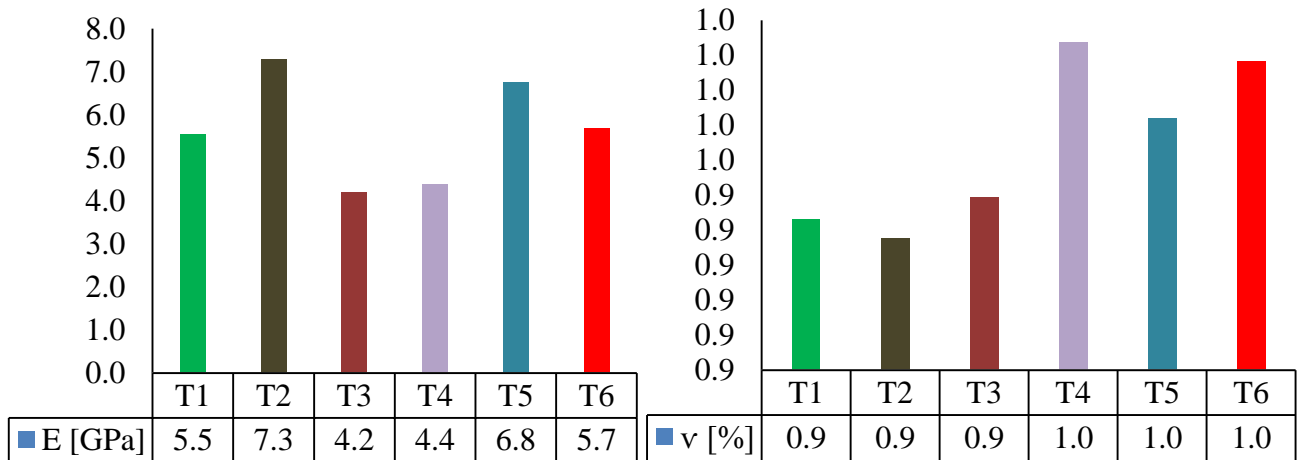
Figure 4-29: Young's modulus of elasticity

	T1	T2	T3	T4	T5	T6
■ v [%]	0.9	0.9	0.9	1.0	1.0	1.0
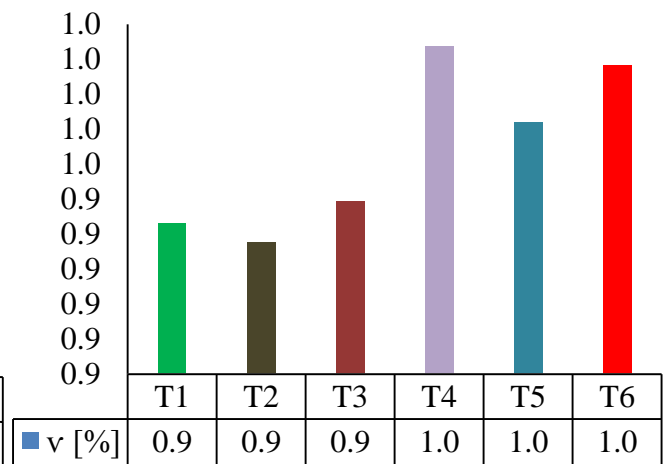
Figure 4-28: Poisson's ratio

	T1	T2	T3	T4	T5	T6
■ %δ	6.2	6.5	5.8	3.4	4.6	3.7
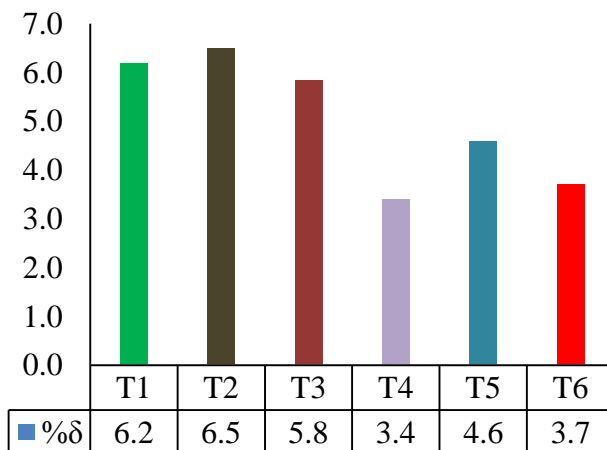
Figure 4-30: Post-fracture percentage elongation

4.1.4. Tensile properties of the Mercurywave sample tested along the 0° fibres

Figure 4-32 (Appendix A) shows failed Mercurywave specimens tested along the 0° fibres axis: L1 cracked below the grip jaw in a nonlinear shape within a heterogenic region; L2 also cracked right below the grip jaw in a V shape following a holes-filled path; L3 cracked within the gage length in a Z shape following a holes-filled path also; T4 cracked below the grip jaw in a nonlinear shape following also a path filled with holes of small diameter; L5 failed within the gage length with the initiation of the crack originating from a hole; L6 failed within the gage length in a combined shape (angular and linear). The stress-strain curves of
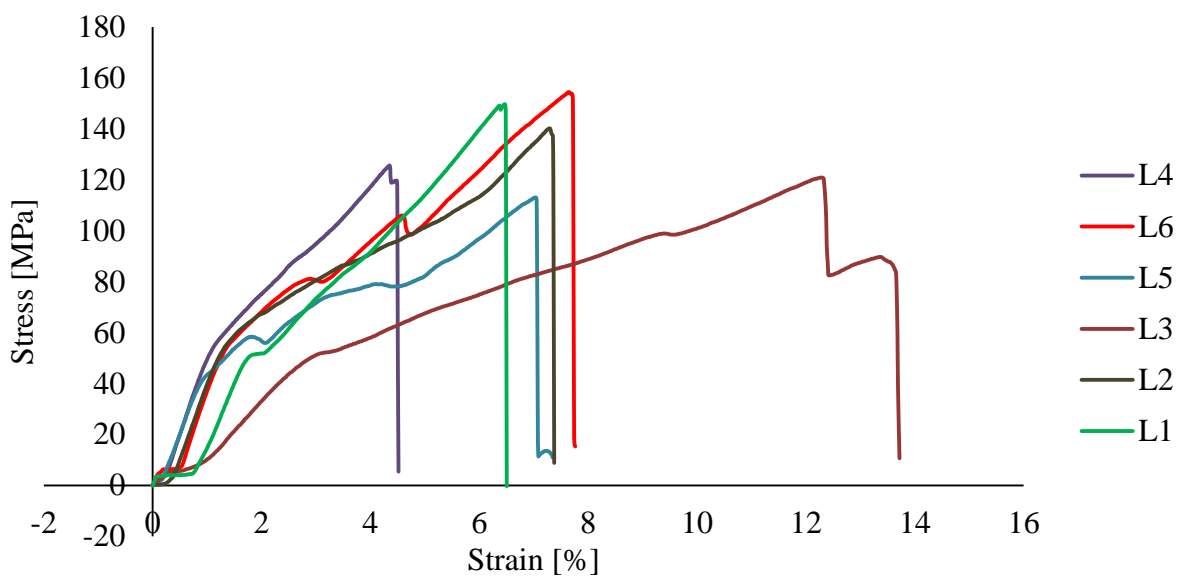
Figure 4-31: Stress-strain curves of Mercurywave specimen tested along the 0° fibres axis

L1   L2   L3   L4   L5   L6
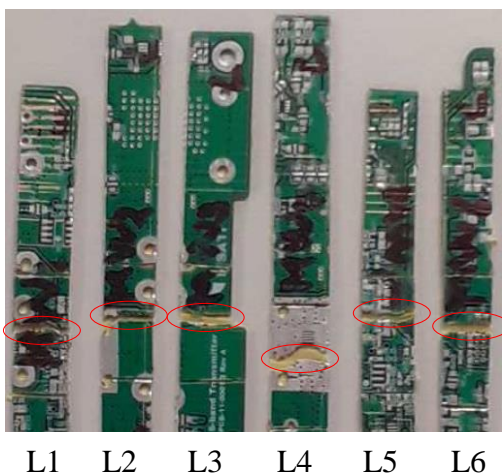
Figure 4-32: Mercurywave specimen tested along the 0° fibres axis

the Mercurywave sample tested along the axis of load-bearing fibres in Figure 4-31 clarified the extent to which each tested specimen elongated before reaching its maximum strength. Properties such as ultimate tensile strength, ultimate tensile strain, offset yield strength, Young's modulus, Poisson's ratio and post-fracture percentage elongation of different specimens are evaluated from these curves.

➢ **Toe correction**

Figure 4-33 presents a detailed description of the reaction of the Mercurywave sample tested along the load-bearing fibres. Characteristics such as the toe correction, the extent of elastic deformation, the extent of transition deformation, the inflection point, the offset point and the breakpoint are illustrated; more details were provided in section 4.1.1.
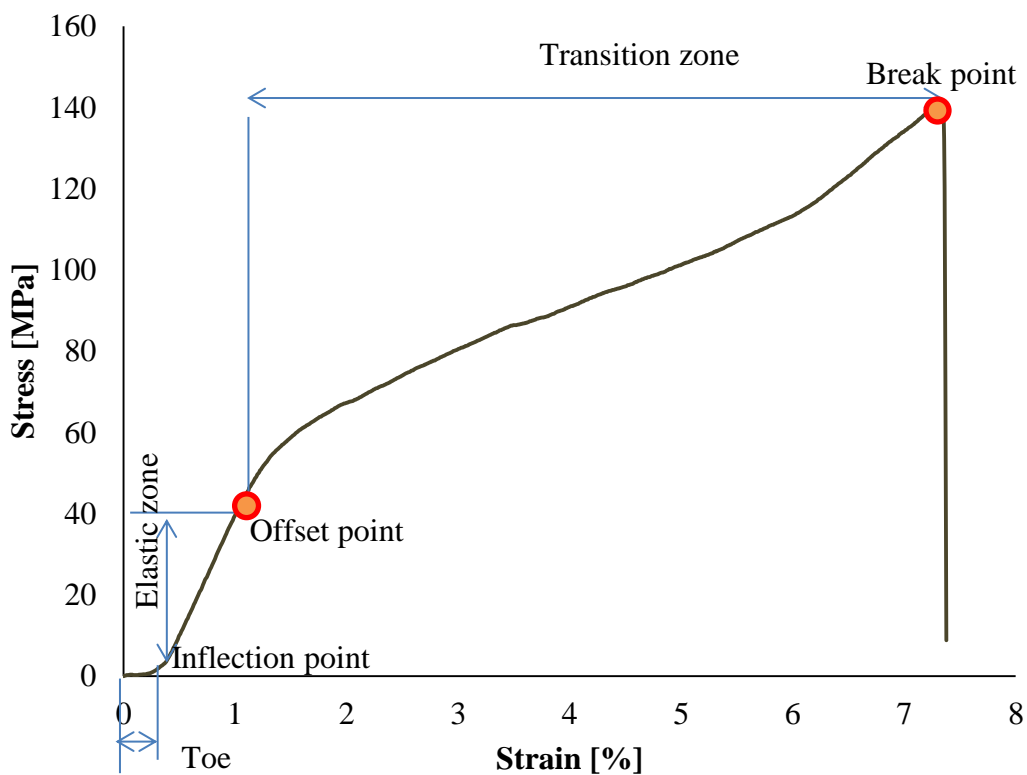
Figure 4-33: Toe correction and other characteristics of the stress-strain curve

➢ **Offset tensile yield strength**

Analysis of the curves in Figure 4-31 verified that the first deviation of the strain from the linear deformation had occurred at different strain rates. Figure 4-34 showed different offset points identified on the curves of Figure 4-31 from which the offset yield strength of different

specimens was computed and illustrated in Figure 4-35. Figure 4-35 shows that specimen L2 had the highest offset yield strength and L5 the lowest yield strength. The mean yield strength was computed at 41.0551 MPa with a standard deviation of 3.0597 at an offset mean of 0.8774% with a standard deviation of 0.4725. Similar to the properties discussed in the previous section, the rate of change in yield strength of the board was irregular. Therefore, the Mercurywave sample subjected to tensile stress did deviate at different offset strains, proving the heterogeneous nature of the sample.

➢ **Ultimate tensile strength**

Figure 4-31 of section 4.1.4 showed that the specimens did not break at the same maximum stress. Each specimen yielded a specific ultimate strength (see Figure 4-36), L6 has the highest ultimate strength and L5 the lowest. A mean ultimate tensile strength of 134.0048MPa with a standard deviation of 15.1841 was computed, showing that different regions of the sample opposed different resistance to tensile stress applied along the 0° fibres.

	L1	L2	L3	L4	L5	L6
■ εO [%]	0.9	0.7	1.9	0.6	0.6	0.5
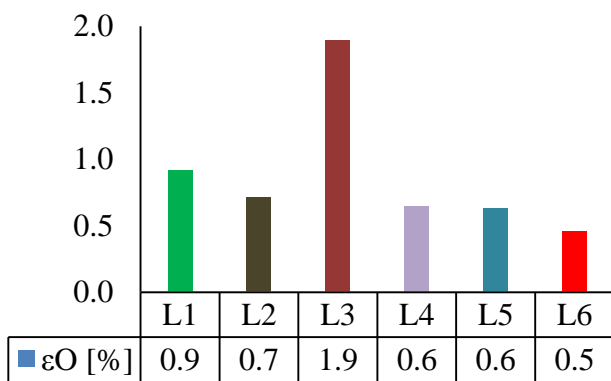
Figure 4-34: Offset strain

	L1	L2	L3	L4	L5	L6
■ σy [MPa]	39.6	45.5	42.5	38.9	36.4	43.5
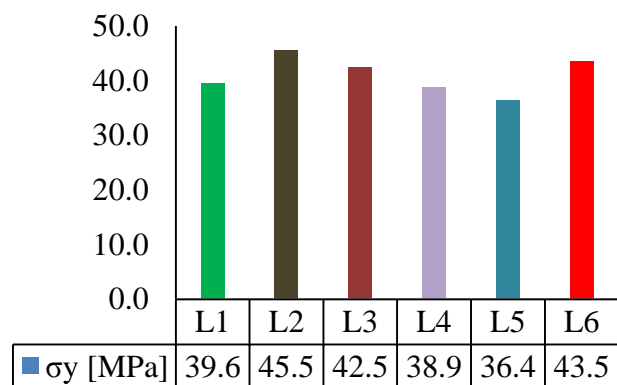
Figure 4-35: Offset yield strength

➢ **Ultimate tensile strain**

The analysis of stress-strain curves of Figure 4-31 in section 4.1.4 confirmed that the specimens obtained from the very same sample broke at different strain rates. Figure 4-37 shows that L3 had the highest strain 11.768% and L4 the lowest. The mean ultimate tensile strain of 7.1208% with standard deviation of 1.2057 was computed, suggesting that when subjected to tensile stress applied along the 0° fibres. A certain region of the sample did elongate significantly more than the other because some parts of the sample were more ductile than others due to the complex nature of the sample (see Figure 4-32).

σult [MPa]	L1	L2	L3	L4	L5	L6
	149.7	140.2	120.9	125.6	113.1	154.5
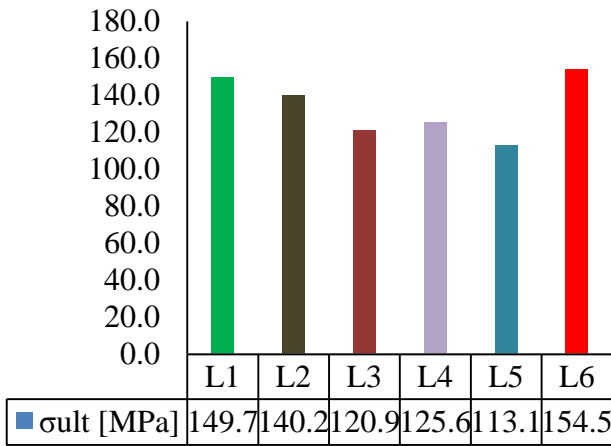
Figure 4-36: Ultimate tensile strength

εUlt [%]	L1	L2	L3	L4	L5	L6
	5.7	7.0	11.8	4.1	6.9	7.2
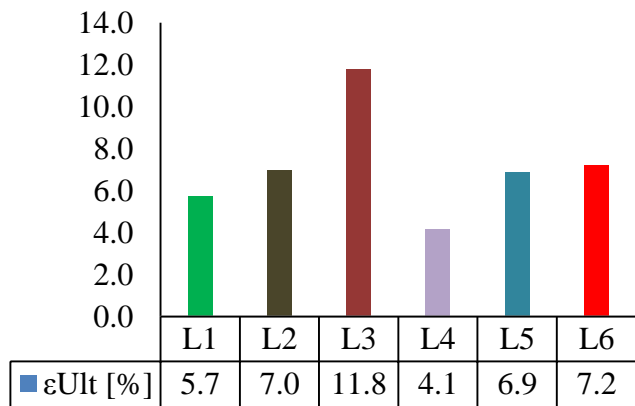
Figure 4-37: Ultimate tensile strain

➢ **Young's modulus of elasticity**

Analysis of Figure 4-33 of section 4.1.4 revealed the extent of elastic deformation of the Mercurywave specimen; and Figure 4-39 gives the Young's modulus of elasticity of different specimens computed from the curves of Figure 4-31. Analysis reveals that L6 has the highest elastic deformation and L3 the lowest. The mean Young's modulus of elasticity was computed at 5.8522 GPa with a standard deviation of 1.9340. This showed that for the very same sample, some regions elastically deformed more than other regions while subjected to tensile stress applied along the 0° fibres.

➢ **Poisson's ratio**

Figure 4-38 displays values of different Poisson's ratios computed for each tested specimen. It was observed that for each specimen, a specific Poisson's ratio was found. The data in Figure 4-39 show that L1 had the highest Poisson's ratio and L3 the lowest. The mean

v [%]	L1	L2	L3	L4	L5	L6
	0.9	0.9	0.4	0.8	0.9	0.9

Figure 4-38: Poisson's ratio

E [GPa]	L1	L2	L3	L4	L5	L6
	4.9	5.5	2.7	6.1	7.0	9.0

Figure 4-39: Young's modulus of elasticity

Poisson's ratio was 0.8311% with a standard deviation of 0.1945, suggesting that the lateral deformation of the sample was not proportional to that of the longitudinal deformation and certain parts of the sample did deform in both the 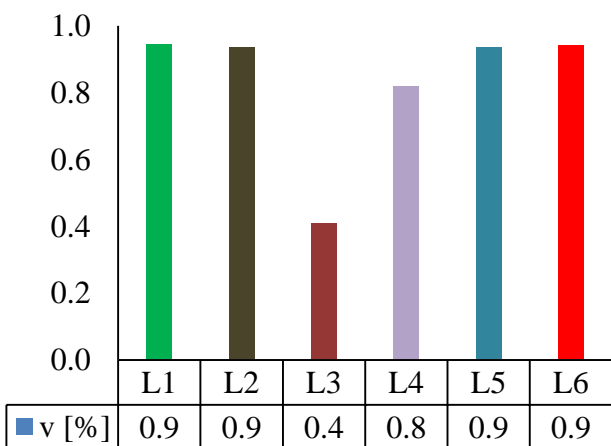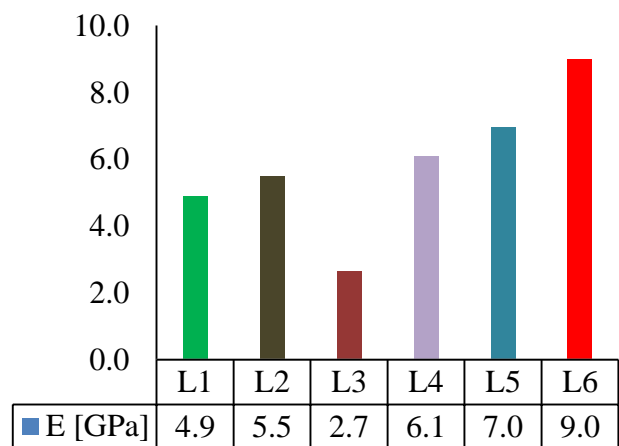longitudinal and transversal direction more than others when the sample was subjected to tensile stress applied along the 0° fibres. The structural configuration of the sample did not allow the sample to react homogeneously, but each region reacted according to its specific structural configuration.

➤ **Post-fracture percentage elongation**

Figure 4-40 shows the different post-fracture percentage elongations computed from the analysis of the curves in Figure 4-31 of section 4.1.4. Figure 4-40 shows that L3 yielded the highest plastic deformation and L4 the lowest. The mean post-fracture percentage elongation computed was 7.0948% with a standard deviation of 2.3192 showing that some parts of the sample did plastically elongate more than others when subjected to tensile stress applied along the 0° fibres.

	L1	L2	L3	L4	L5	L6
■%δ	5.7	7.0	11.7	4.1	6.8	7.2
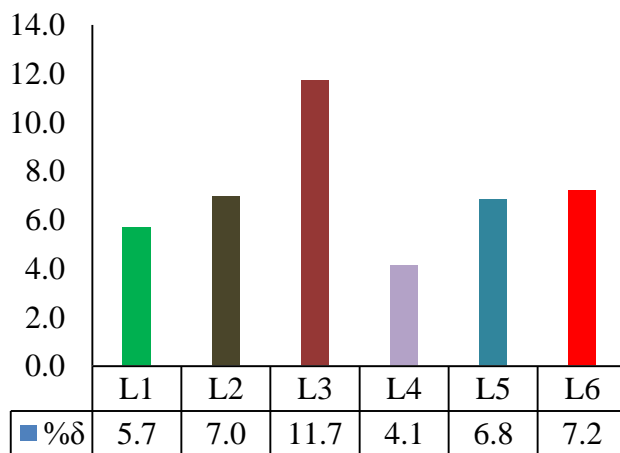
Figure 4-40: post-fracture percentage elongation

4.2. Flexure test result

The Mercurywave and FR-4 samples tested to flexure stress were analysed and presented in this section; eight specimens per sample were tested, four along and four across their load-bearing fibres axis. This section will begin by analysing the flexure properties of the FR-4 sample, followed by that of the Mercurywave sample.

4.2.1. Flexure properties of FR-4 sample tested across the load-bearing fibres
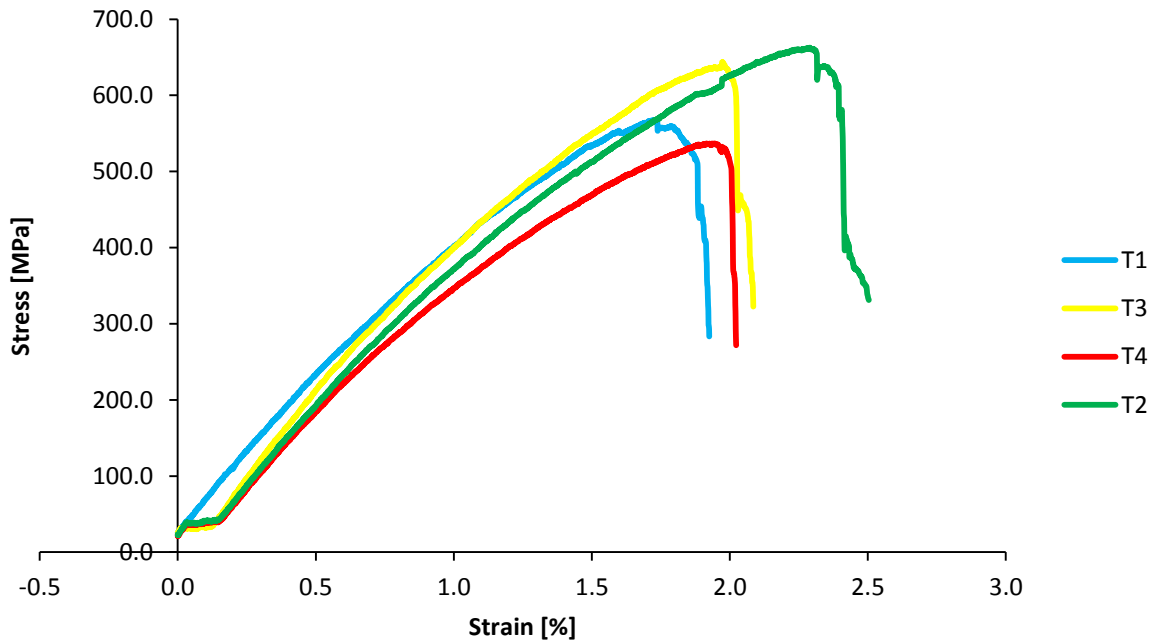
Figure 4-41: FR-4 sample tested to flexure stress across the 0o axis of its fibres

| Specimen 3 | Specimen 2 | Specimens 1 & 4 |
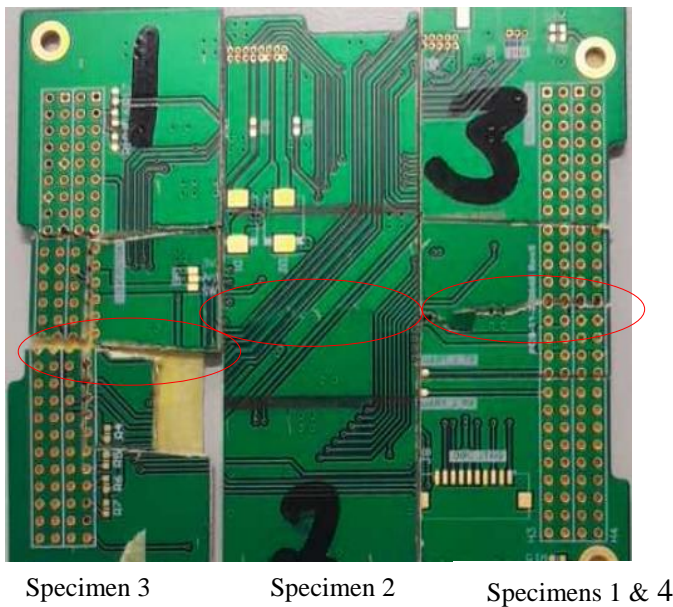
Figure 4-42: The FR-4 specimens tested across the fibre load-bearing axis

The curves of Figure 4-41 displayed the reaction of the FR-4 specimens subjected to flexure stress applied across their load-bearing fibres. Analysis determined that T1 had the lowest bending strain; T2 had the highest bending strength and strain; T3 had the lowest bending strength; and T4 had a bending strength and strain lower than that of T2 but greater than those of T3 and T4. Figure 4-42 shows failed specimens cut from the same sample: T1 and T4 had the very same structural configuration so there was no need to represent T4 in Figure

4-42 (Appendix B). Figure 4-42 shows the propagation of fracture throughout the width of T1 following a holes-filled path. It demonstrated why it appeared to be the weakest part of the sample; T2 had no hole on it and its curve in Figure 4-41 showed that it was the strongest part of the specimen; and T3 had holes as T1 on one side, but the other side has no hole on it; thus, it had a moderate strength compared to T1, T2 and T4.

> **Toe correction**

Figure 4-43 presents a descriptive analysis of the stress-strain curve of a specimen tested to flexure stress applied along its load-bearing fibres. The description in section 4.1.1 applied to
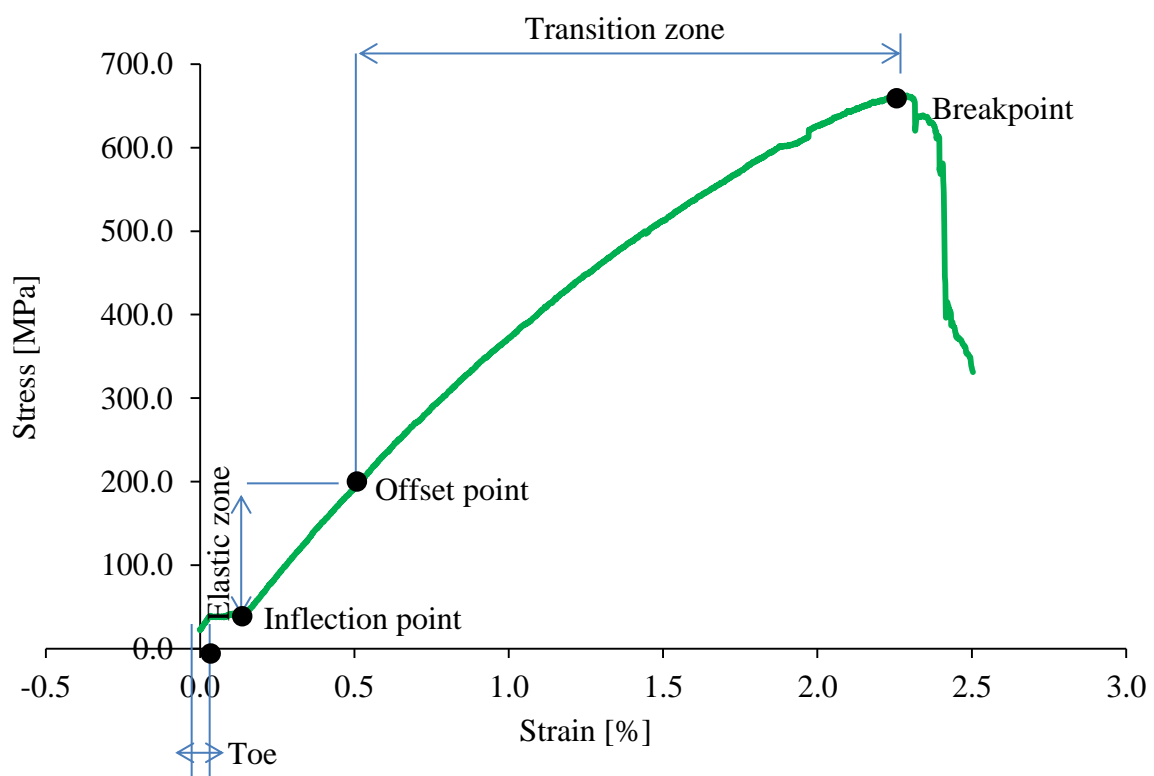
Figure 4-43: Toe correction for the FR-4 sample tested to flexural stress along its axis of load-bearing fibres

this section and the characteristics described are the same.

> **Bending stiffness**

The rate at which the specimen deflected as a function of the applied flexure stress is an important factor in determining the strength of the specimen. Figure 4-44 shows different bending stiffness measured on the different specimens. The analysis showed that T3 had the highest bending stiffness and T1 the lowest. The mean bending stiffness of 32.3438 N/mm with a standard deviation of 1.5994 was computed, verifying that the resistance of the sample

to flexure stress was a function of the localised structural configuration of each part of the sample as the four specimens were cut from the same sample.

Analysis of Figure 4-44 showed that when subjected to flexure stress, the region of the sample corresponding to T3 opposed high resistance while T1 did bend easily.
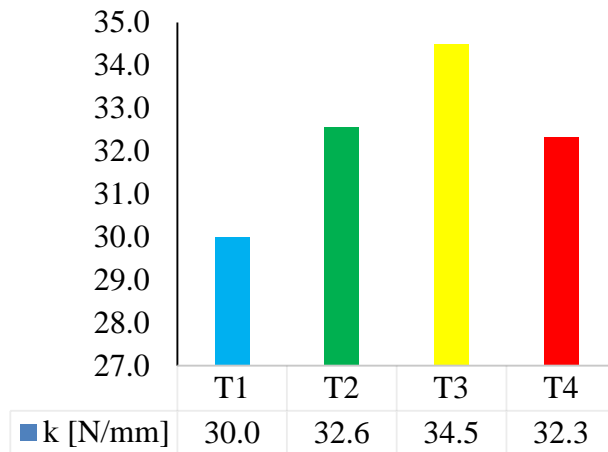
Figure 4-44: Bending stiffness

	T1	T2	T3	T4
■ k [N/mm]	30.0	32.6	34.5	32.3

➤ **Flexure yield strength**

Analysis of Figure 4-41 shows that the four specimens deformed following a similar path until the offset point was exceeded. Analysis of Figure 4-46 revealed different offset points at which yield occurred. Figure 45 gave the value of different yield strengths deducted from the curves of Figure 4-41. Figure 4-46 shows that L1 deviated at the highest offset strain corresponding to the highest yield strength and L3 yielded at the lowest offset strain corresponding to the lowest yield strength. The mean yield strength of 183.8984 MPa was computed with a standard deviation of 31.1439, showing that the sample did yield differently according to the localised structural configuration. Under flexure stress, the L1 region of the sample deflected elastically more and the L3 region did deflect less elastically, again confirming that the FR-4 sample has a complex structural configuration.
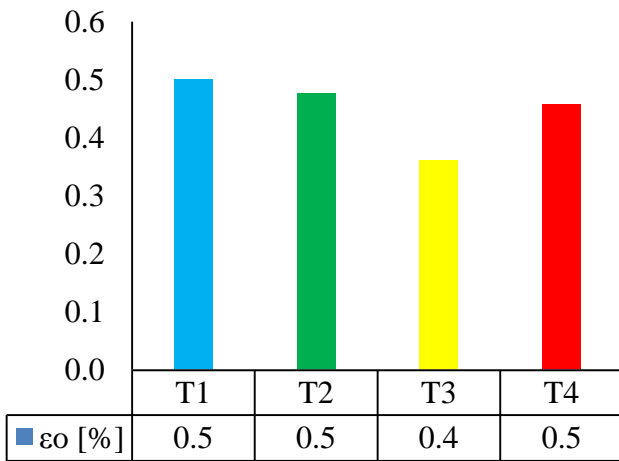
Figure 4-46: Offset strain

	T1	T2	T3	T4
■ εo [%]	0.5	0.5	0.4	0.5
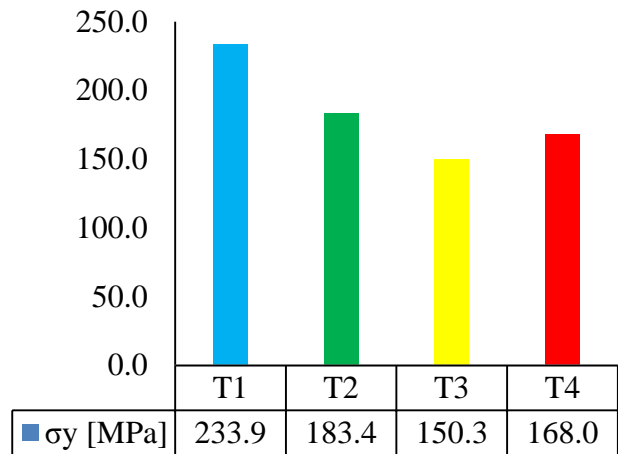
Figure 4-45: Yield strength

	T1	T2	T3	T4
■ σy [MPa]	233.9	183.4	150.3	168.0

➢ **Flexure strength**

Analysis of Figure 4-41 showed that not all specimens exhibited the very same strength to the application of flexure stress. Figure 4-47 supported the analysis of Figure 4-41 where L2 opposed the highest resistance to the application of the flexure stress and L1 the lowest. The mean flexure strength computed from Figure 4-47 was noted at 602.6554 MPa with a standard deviation of 52.1477. Figure 4-43 showed that L2 does not have as many holes as the other specimens; thus, this region of the sample exhibited high resistance to the application of flexure stress.
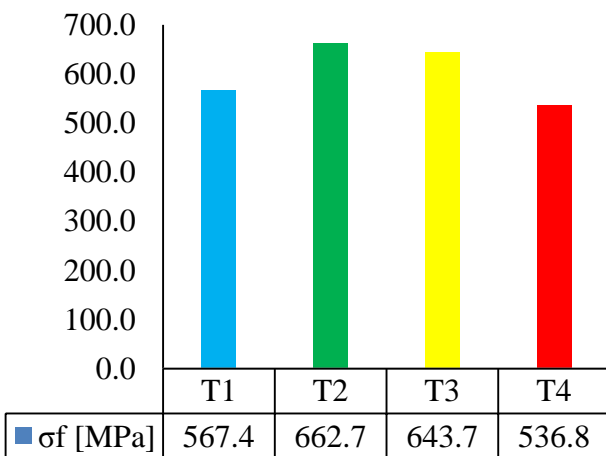
Figure 4-48: Flexure strength

	T1	T2	T3	T4
■ σf [MPa]	567.4	662.7	643.7	536.8

Figure 4-47: Flexure strain

	T1	T2	T3	T4
■ εf [%]	1.7	2.3	2.0	1.9

➢ **Flexure strain**

The stresses induced in the specimen produced deflection of the specimen at a different rate (see Figure 4-41). Each specimen did break at a specific strain, but none reached the 5%

strain. Figure 4-47 indicated the value of strain computed from the curves, showing that L2 deflected much more and L1 less before fracture. A mean strain of 1.9609 with a standard deviation of 0.2034 was computed from Figure 4-47 showing that when subjected to flexure stress applied across its load-bearing axis, the FR-4 sample deflected according to the localised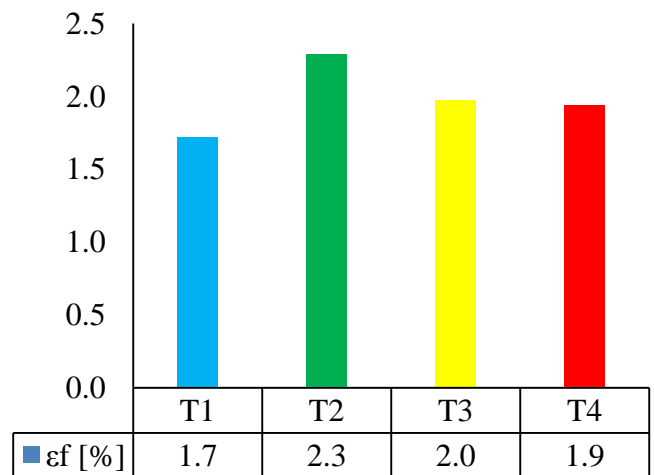 configuration of each region of the sample. The L2 region of the sample deflected more when localised flexure stress was induced in its midsection, but fracture was initiated from the region of L1.

> **Flexure modulus of elasticity**

Figure 4-42 shows that the first type of deformation noticed in the deflection of specimens was an elastic one; this elastic deformation was characterised by the modulus of elasticity of the specimen. The specimens were obtained from the same sample; the computed elastic modulus of each specimen determines the elastic reaction of a different region of the sample to flexure stress. According to Figure 4-50, L3 displayed the highest modulus of elasticity and L4 the lowest. The mean modulus of elasticity was computed at 42.0242 GPa with a standard deviation of 2.7980, showing that the localised structural configuration of the sample had an impact on the elastic deformation of the sample. From the results obtained, it was evident that the L3 region of the sample did elastically deform much more than the other

	T1	T2	T3	T4
■ Ef [GPa]	41.4	41.1	46.6	39.0
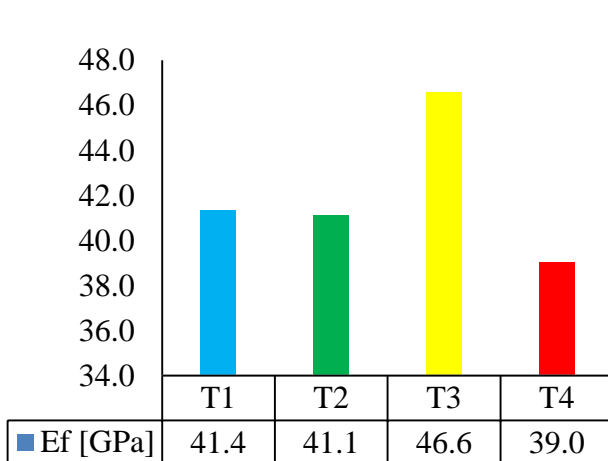
Figure 4-50: Flexure modulus of elasticity

	T1	T2	T3	T4
■ θ˚	46.2	60.5	52.6	49.9

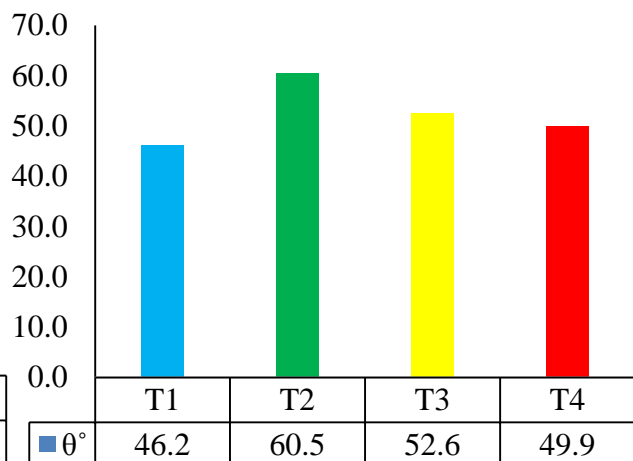**Figure 4-49: deflection angle at fracture 0° fibres**

regions, but plastic deformation was initiated from region 4.

> **Measurement of sample's ductility**

Analysis of Figure 4-42 shows that the specimens resisted high flexure stress before the occurrence of fracture, but each specimen broke at a different deflection, making an angle between the orientation of the specimen and the orientation of the deflection. Figure 4-49 presents the different angles at which each specimen reached its maximum strain or break. L2 deflected at a high angle and L1 at the lowest one. The mean angle of deflection of the sample was computed at 52.0603^o with a standard deviation of 5.1444 showing that the specimen deflected up to more than half the support span of the testing fixture. The standard deviation shows that the sample did not deflect with the very same angle, but each localised region deflected according to its structural configuration. The magnitude of the mean angle showed that the FR-4 sample tested along the axis of load-bearing fibres was highly ductile.

4.2.2. Flexure properties of FR-4 sample tested across the load-bearing fibres

The curves of Figure 4-51 displayed the reaction of the FR-4 specimens tested across the axis of their load-bearing fibres: specimen one (L1) had the lowest bending strength; specimen two (L2) had the highest bending strain; specimen three (L3) had a bending strength and strain greater than that of specimen one (L1) but its bending strength was greater than that of specimen two (L2) with strain lower than that of specimen two (L2); specimen four (L4) had the highest bending strength with the lowest bending strain. Figure 52 (Appendix B) shows failed specimens cut from the same sample: specimens 1 and 4 are similar and illustrated by specimen 1. Analysis of Figure 4-52 shows that the fracture did not propagate in a linear path.
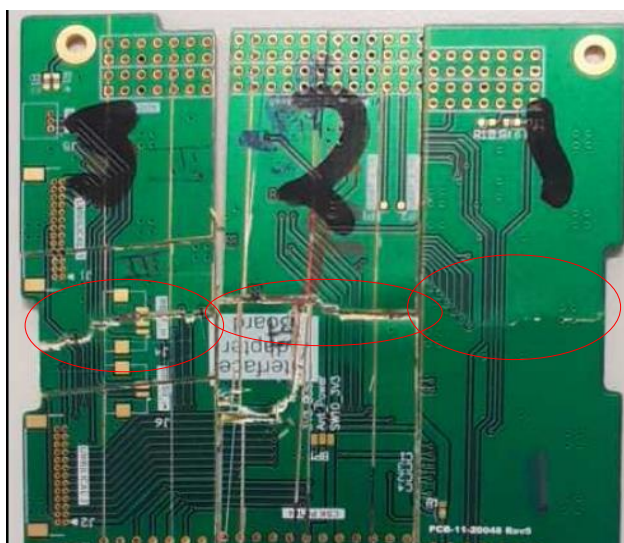
Specimen 3   Specimen 2   Specimen 1 & 4

Figure 4-51: Failed specimen tested along the 0° fibres
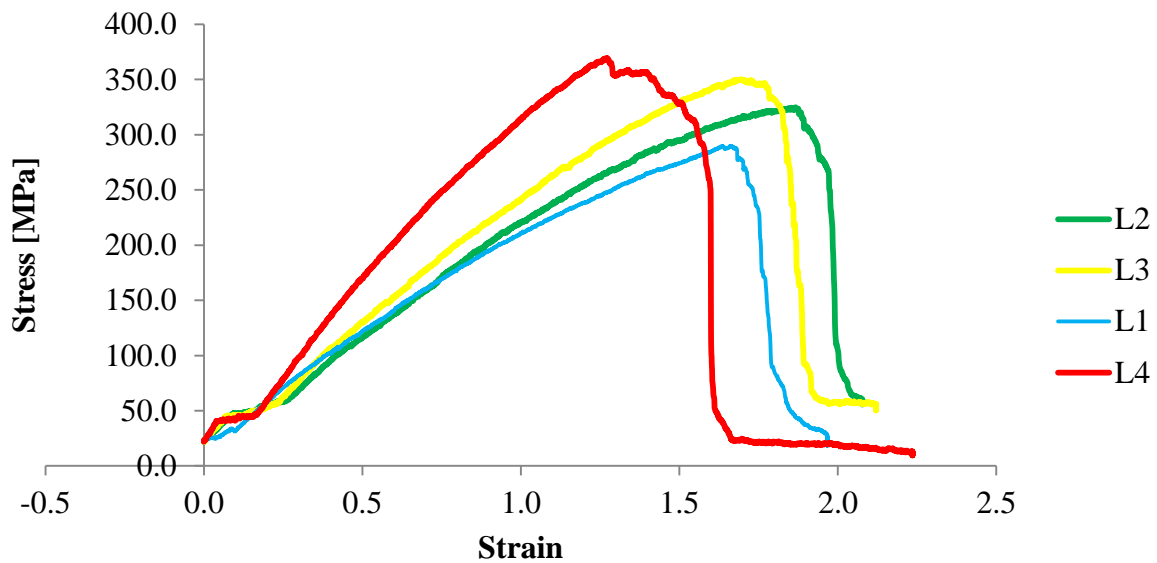
Figure 4-52: Stress-strain curves of the FR-4 sample tested across the axis

➢ **Toe correction**

Figure 4-53 presents a detailed description of the stress-strain curve of the FR-4 sample tested to flexural stress applied across its load-bearing fibres. The explanation in section 4.1.2 applies to this section as well.
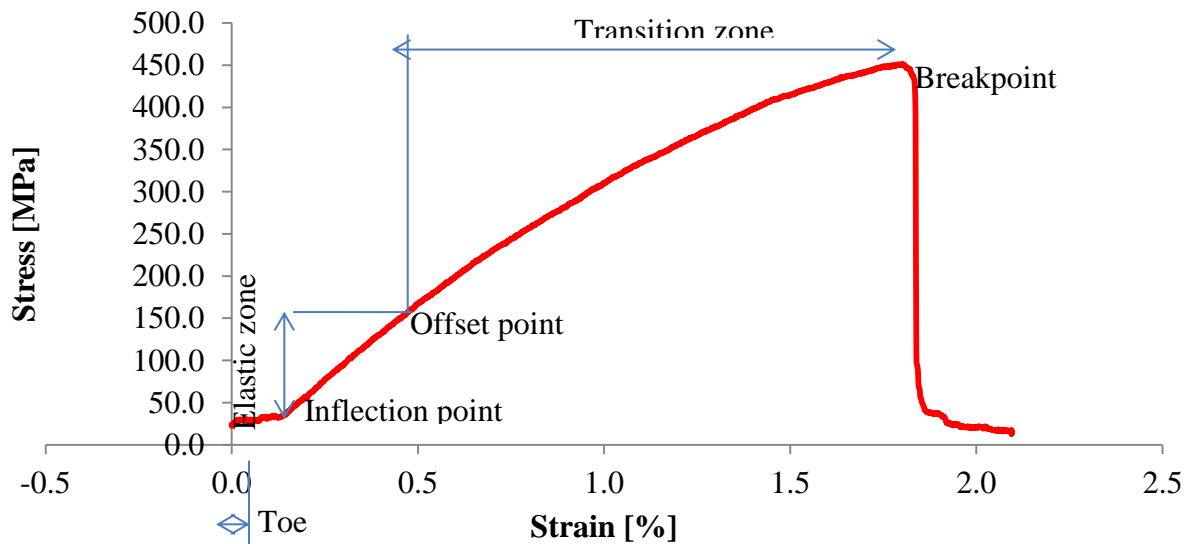
Figure 4-53: Toe correction for the FR-4 specimen tested across the fibre load-bearing axis

➢ **Bending stiffness**

The rate at which the specimen deflected as a function of the applied flexure stress was computed and Figure 4-54 displays different bending stiffness measured on different tested

specimens. Analysis showed that T4 had the highest bending stiffness and L1 the lowest. The mean bending stiffness of 22.7100 N/mm with a standard deviation of 3.4484 was computed suggesting that the resistance of the sample to flexure stress was a function of the localised structural configuration of the sample as the four specimens were cut from the same sample. The region T4 of the sample did oppose high resistance to the application of flexure stress and region T2 did bend easily.

	L1	L2	L3	L4
■ k [N/mm]	20.3	19.6	22.6	28.4
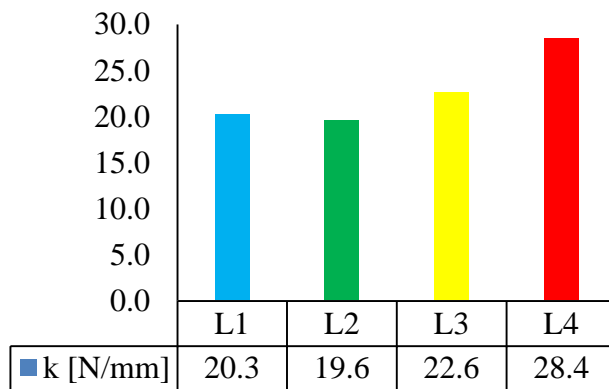
Figure 4-54: Bending stiffness

➤ **Yield strength**

Analysis of Figure 4-52 showed that the four specimens yielded in different ways. Figure 4-56 gave different offset points at which yield occurred, and Figure 4-55 gave the value of different yield strengths deducted from the curves of Figure 4-53. Data in Figure 4-56 verified that T4 deviated at the highest offset strain which corresponds to the highest yield strength, and T1 yielded at the lowest offset strain. The mean yield strength of 119.7527 MPa was computed with a standard deviation of 31.2269, showing that the sample did yield differently according to the localised structural configuration. T4 region did deform

	L1	L2	L3	L4
■ εo [%]	0.3	0.4	0.4	0.5

Figure 4-56: Offset strain

	L1	L2	L3	L4
■ σy [MPa]	91.4	103.4	106.4	164.5

Figure 4-55: Flexure yield strength

53

elastically more than other regions of the sample, but plastic deformation was initiated from region T1.

➢ **Flexure strength**

Analysis of Figure 4-51 showed that each specimen opposed a specific resistance to the application of the flexure stress, and analysis of Figure 4-57 showed that T4 had the highest resistance to the application of the flexure stress and T1 the lowest. The mean flexure strength computed from Figure 4-57 was at 360.3361 MPa, with a standard deviation of 53.8635 giving evidence that the sample did not have the same strength within all its regions, but the T4 region did oppose high resistance to the application of the flexure stress due to its structural configuration (see Figure 4-52).
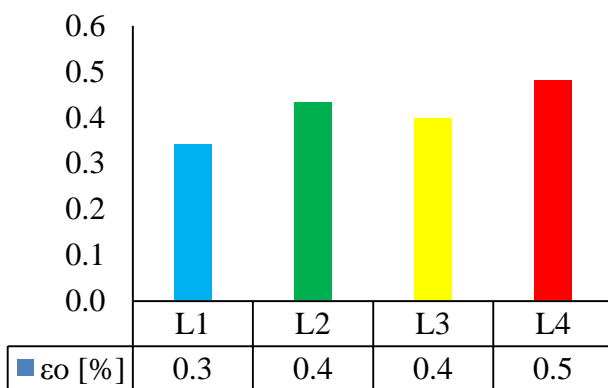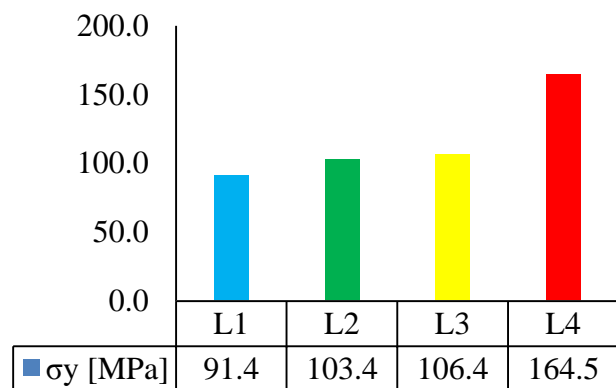
➢ **Flexure strain**

The stresses induced in the specimen produced deflection at a different rate (see Figure 4-51) where each specimen did break at a specific strain, but none reached the 5% strain. Figure 4-58 gives the value of strain computed from the curves, showing that T2 deflected quite a bit more and T4 deflected less before failure. A mean strain of 1.8693 with a standard deviation of 0.31128 was computed, showing that when subjected to flexure stress, the sample did deflect according to the localised structural configuration of each region of the sample. Region T2 deflected more than all the others, but the highest stress concentration was in the T4 region from where fracture of the sample was initiated.

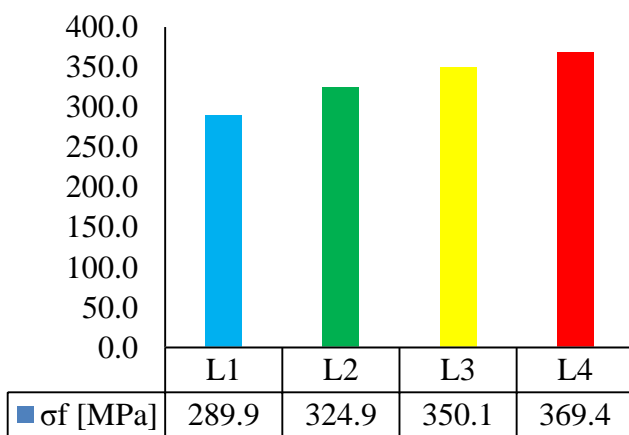|	L1	L2	L3	L4
σf [MPa]	289.9	324.9	350.1	369.4

Figure 4-57: Flexure strength

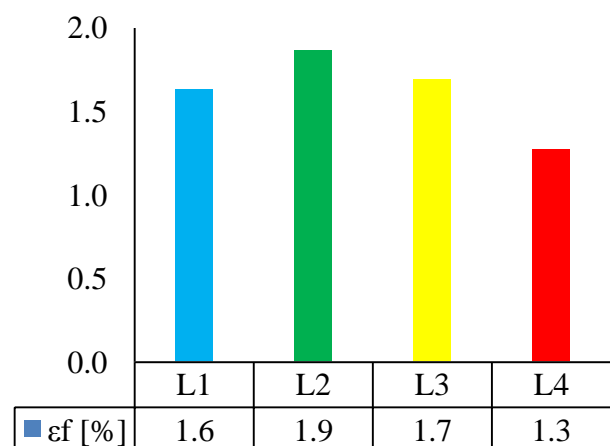|	L1	L2	L3	L4
εf [%]	1.6	1.9	1.7	1.3

Figure 4-58: Flexure strain

➢ **Flexure modulus of elasticity**

Figure 4-51 confirmed that the first type of deformation noticed in the deflection of specimens was elastic (see Figure 4-53), characterised by the modulus of elasticity of the specimen. Knowing that the specimens were obtained from the same sample, the computed modulus of each specimen determined the elastic reaction of a different region of the sample to flexure stress. Figure 4-59 shows that T4 had the highest modulus of elasticity and T1 the lowest; the mean modulus of elasticity was 27.8016 GPa with a standard deviation of 4.0382 showing that the localised structural configuration of the sample had an impact on the elastic deformation of the sample. The T4 region did deform elastically more than the other regions but the plastic deformation was initiated from region T1.

	L1	L2	L3	L4
■ Ef [GPa]	22.3	24.4	27.4	35.6
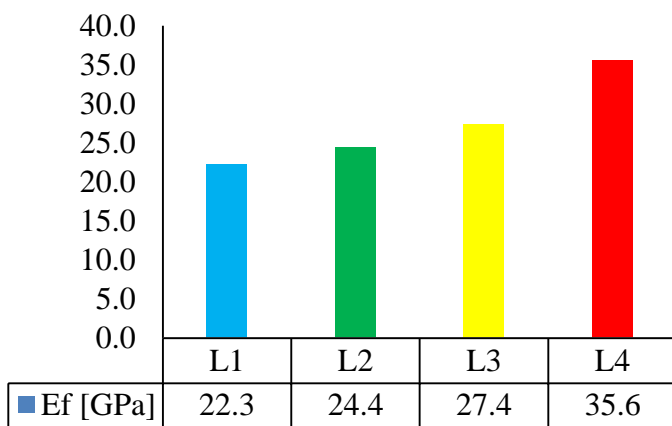
Figure 4-60: Flexure modulus of elasticity

	L1	L2	L3	L4
■ θ°	42.7	48.5	44.2	34.5
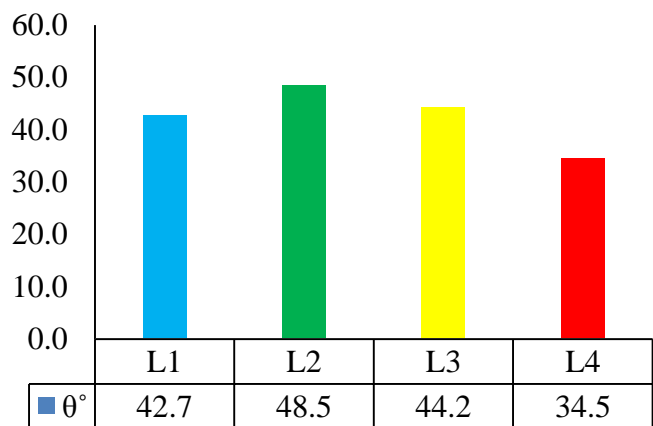
Figure 4-59: Deflection angle at the fracture

➢ **Measurement of sample's ductility**

Analysis of Figure 4-51 showed that the sample opposed lower resistance to the application flexure stress compared to the specimens tested across the 0° fibres before the occurrence of fracture. But each specimen did break at a different deflection making an angle between the orientation of the specimen's support span and the orientation of the deflection. Figure 4-60 showed the different angles at which the specimens did reach their maximum strain or break, where T2 was shown to have deflected at the highest angle and T4 at the lowest. The mean angle of deflection of the sample was computed at 42.6653^o with a standard deviation of 5.0382 showing that the sample deflected just about half the support span of the testing fixture. The standard deviation showed that the sample did not deflect at the same rate, but each localised region deflected according to its structural configuration. The value of the mean deflection angle showed that the FR-4 sample tested along the axis of load-bearing fibres was less ductile than that tested across the axis.

4.2.3. Flexure properties of Mercurywave sample tested across the axis of the load-bearing fibres

The curves of Figure 4-61 displayed the reaction of the Mercurywave specimens tested across the load-bearing fibres. The figure confirmed that each sample reacted differently to the application of the flexure stress: T1 presented high resistance followed by T4, then T2, and

T4   T1   T3   T2
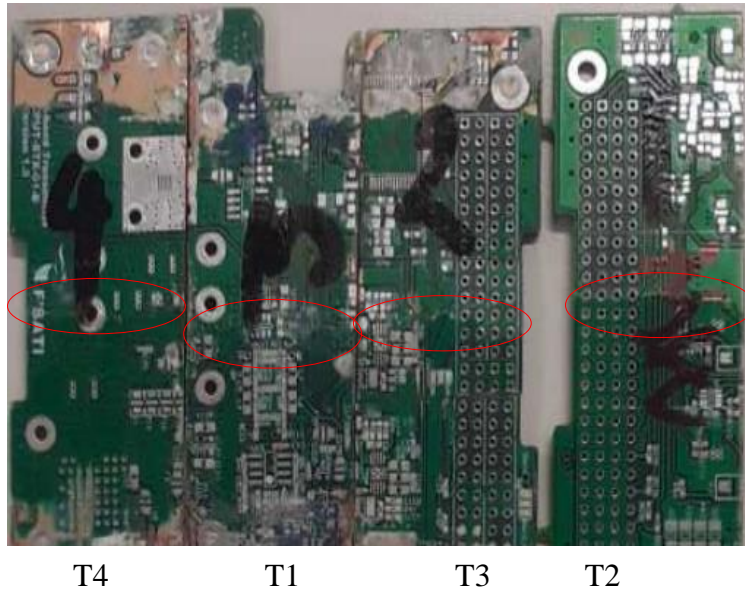
Figure 4-62: Failed Mercurywave specimens tested across the 0° fibres
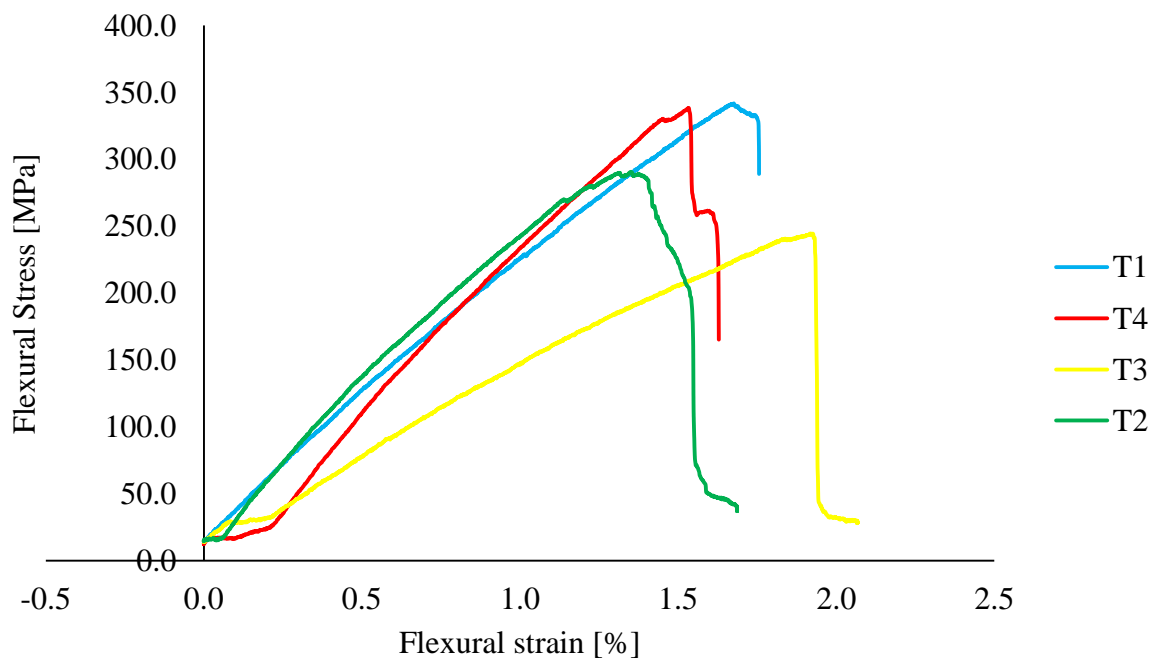
Figure 4-61: Stress-strain curves of the Mercurywave specimen tested across the axis

later T3 with the highest deflection. Figure 4-62 (Appendix B) shows fractured specimens: the specification of Figure 4-62 was that it gave an idea of the structural configuration of each specimen or a view of the complexity of the sample from which these specimens were obtained.

➢ **Toe correction**

Figure 4-63 presents a descriptive analysis of the stress-strain curve of a specimen tested to flexure stress across the axis of the load-bearing fibres. Analysis in section 1.1.1 is applicable to this section
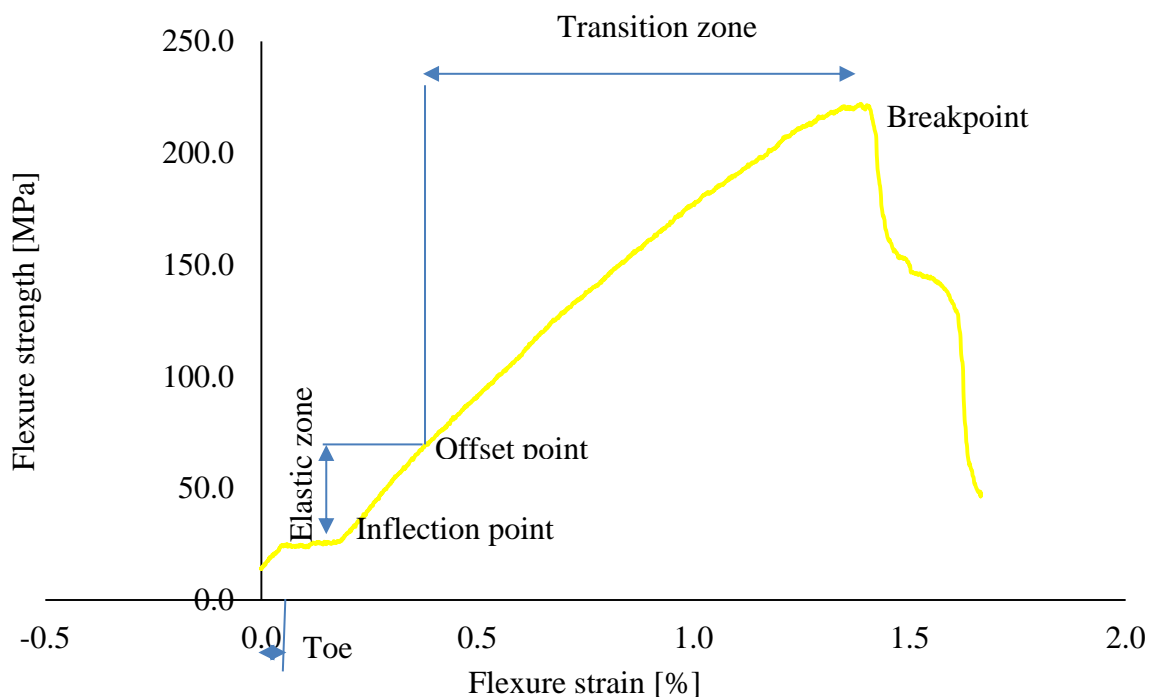
Figure 4-63: Toe correction for the Mercurywave sample tested across the axis

.

➢ **Bending stiffness**

According to Figure 4-64, different bending stiffness was measured on different specimens, where T4 had the highest bending stiffness and T3 the lowest. A mean bending stiffness of 28.1094 N/mm with a standard deviation of 12.2396 was computed, demonstrating that the resistance of the sample to flexure stress was a function of its localised structural configuration. The L4 region of the sample did oppose high resistance to deflection but the

T3 region did bend easily. The standard deviation showed that the resistance of the sample to
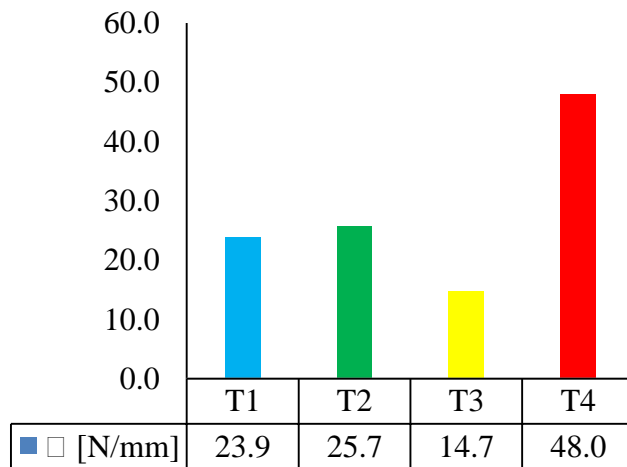
Figure 4-64: Bending stiffness

	T1	T2	T3	T4
■ □ [N/mm]	23.9	25.7	14.7	48.0

bending stress was irregular throughout the width of the sample.

➢ **Yield strength**

Analysis of Figure 4-61 showed that the four specimens yielded in different paths. Figure 4-65 reveals different offset point at which yield did occur, and Figure 4-66 gives the value of different yield strength deducted from the curves of Figure 4-62. Figure 4-65 shows that T3 deviated at the highest offset strain but according to Figure 4-66, T1 displayed the highest yield strength and T2 the lowest yield strength with the lowest offset strain. The mean yield strength of 125.8515 MPa was computed with a standard deviation of 14.8024, showing that the sample did yield differently according to the localised structural configuration. The T1

	T1	T2	T3	T4
■ εo [%]	0.6	0.4	0.8	0.6

Figure 4-66: Offset strain

	T1	T2	T3	T4
■ σy [MPa]	143.2	103.7	122.2	134.3

Figure 4-65: Yield strength

region was more elastic than other regions, but the T2 region deviated earlier than all the others.

➢ **Flexure strength**

Analysis of Figure 4-61 showed that T1 had the highest resistance to the application of the flexure stress and T3 the lowest. Figure 4-68 shows the computed flexure strength of the Mercurywave sample within its different regions. Mean flexure strength computed from the results presented in Figure 4-68 was noted at 602.6554 MPa with a standard deviation of 52.1477. Analyses of Figures 4-61 and 4-68 showed tha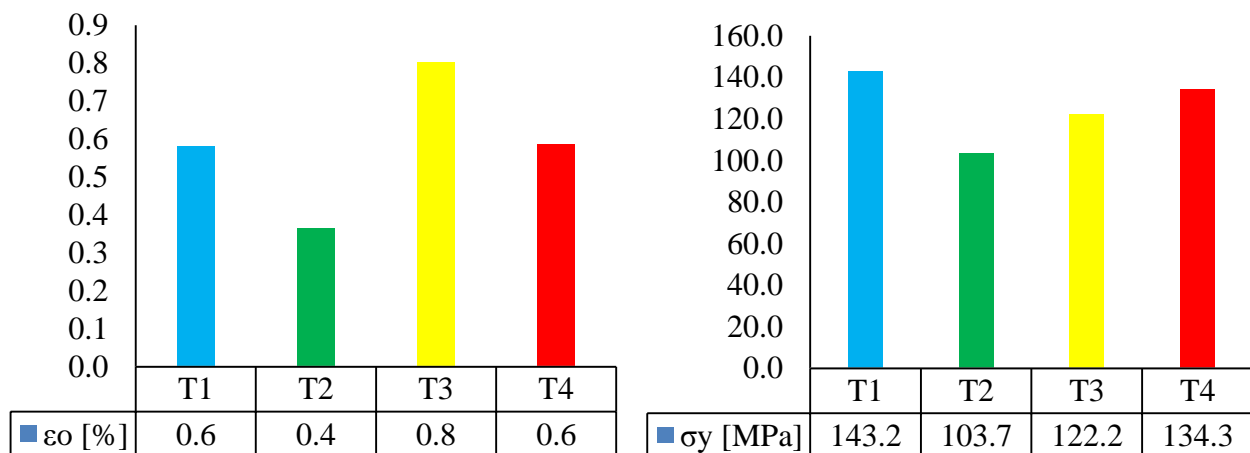t the T1 region of the sample did oppose high resistance to the application of the flexure stress and the T3 region, the lowest, because of the highly complex nature of the sample.

➢ **Flexure strain**

The stresses induced in the specimen produced a deflection of the specimen at a different rate (see Figure 4-61) where each specimen broke at a specific strain, but none reached the 5% strain. Figure 4-67 gives the value of strain computed from the curves, suggesting that T3 deflected more and T2 deflected less before fracture. A mean strain of 1.6201% with a standard deviation of 0.2079 was computed, demonstrating that when subjected to flexure stress, the T3 region of the sample did deflect more than other regions but failure was initiated from region T2.

	T1	T2	T3	T4
■ σf [MPa]	341.7	290.7	244.5	338.4

Figure 4-68: Flexure strength

	T1	T2	T3	T4
■ εf [%]	1.7	1.4	1.9	1.5

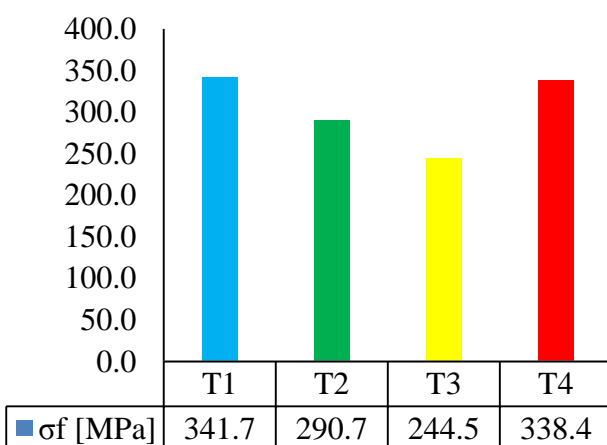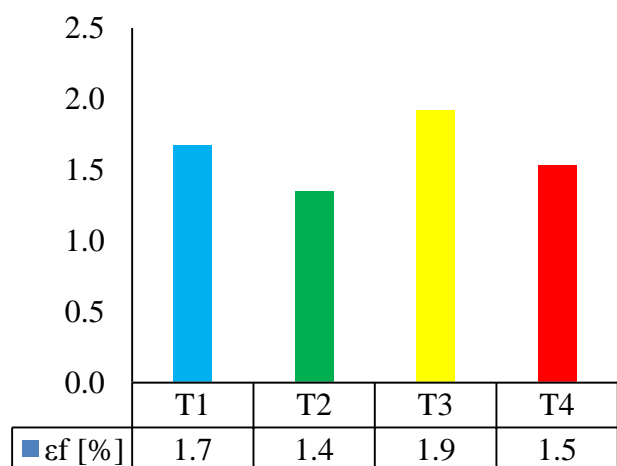**Figure 4-67: Flexure strain**

➢ **Flexure modulus of elasticity**

Figure 4-63 shows that the first type of deformation noticed in the deflection of specimens is an elastic one as explained above. From Figure 4-69, T4 displayed the highest modulus of elasticity and T3 the lowest; the mean modulus of elasticity was 23.7080 GPa with a standard deviation of 5.6112, showing that the localised structural configuration of the sample had an impact on the elastic deformation of the sample. The results displayed in Figure 4-69 show that the T4 region of the sample did deform elastically more than other regions, but plastic deformation was initiated from region T3.

➤ **Measurement of sample's ductility**

Figure 4-70 presents the different angles at which the specimens reached their maximum strain or break. T3 deflected at the highest angle and T2 at the lowest. The mean angle of deflection of the sample was computed as 40.6581^{o} with a standard deviation of 6.5005 showing that the specimen deflected up to about half the support span of the testing fixture. The standard deviation shows that the sample did not deflect with the very same angle, but each localised region did deflect according to its structural configuration. The magnitude of the mean angle showed that the Mercurywave sample tested across the axis of load-bearing fibres was ductile.

	T1	T2	T3	T4
Ef [GPa]	22.1	28.3	15.2	29.2
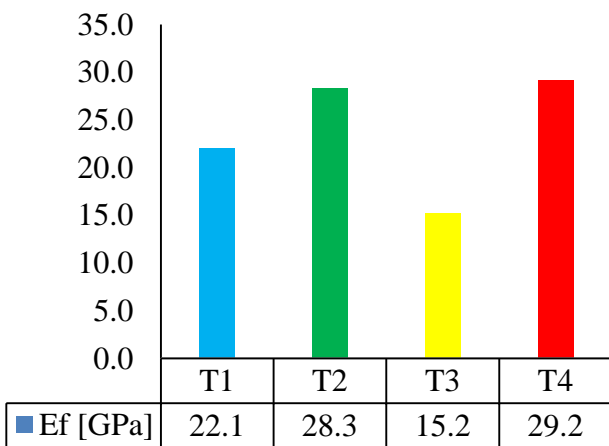
Figure 4-70: Flexure modulus of elasticity

	T1	T2	T3	T4
θ˚	43.7	35.5	49.8	33.6
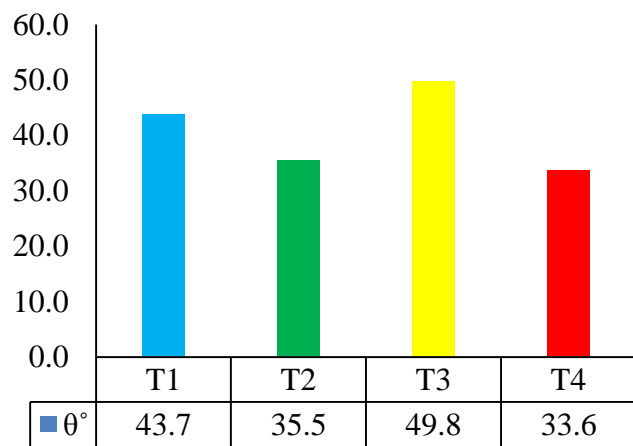
Figure 4-69: Angle of deflection of the specimen

4.2.4. Flexure properties of Mercurywave sample tested along the axis

Figure 4-71 gives the reactions of Mercurywave specimens subjected to flexure stress applied along the load-bearing fibres. Analysis showed that the stress-strain curves of all specimens followed the same path but did not oppose the same resistance to the application of the flexure stress. L3 broke at the lowest stress and strain; L1 and L4 followed the very same

path but L1 broke a lower stress then L4; and L2 broke at the highest stress and strain. Figure 4-72 (Appendix B) shows failed specimens cut from the same sample; it displayed different
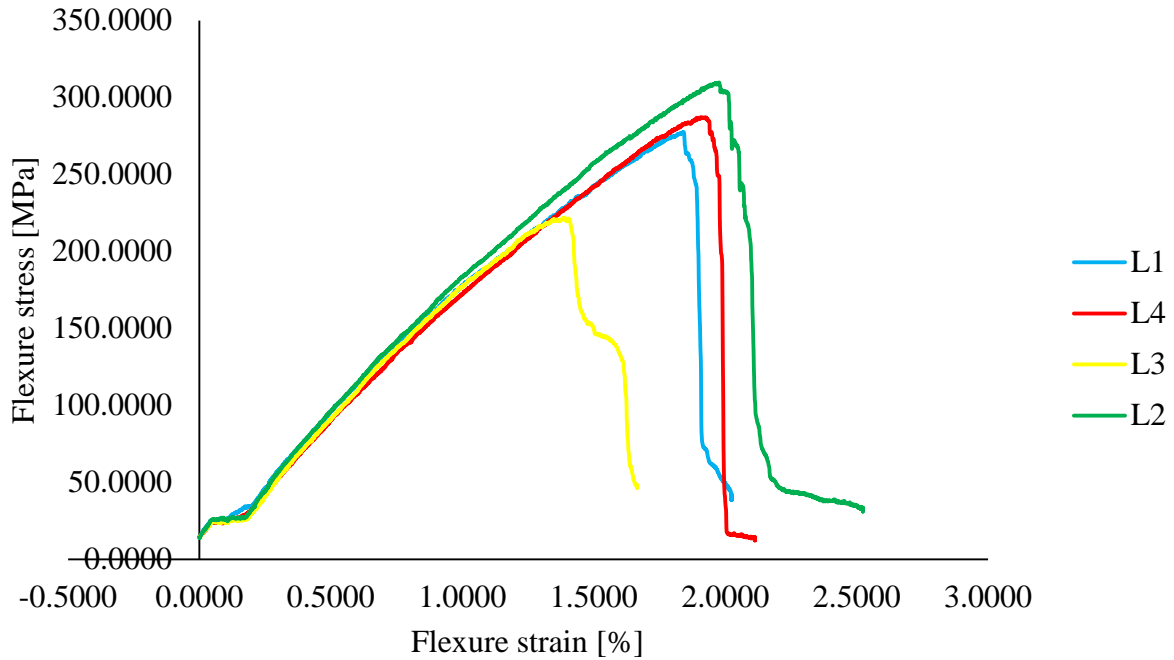
Figure 4-72: Stress-strain curves for the Mercurywave sample tested along the axis

outer structural configurations of the specimens.

The impact of each localised structural configuration of the sample on its reaction to flexure stress was assessed through the analysis of the stress-strain curves in Figure 4-71. Details are
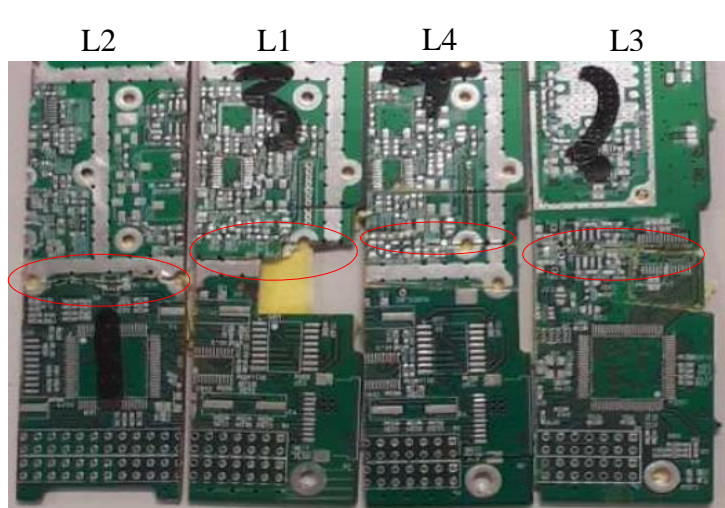
Figure 4-71: Failed Mercurywave specimens tested along the 0° fibres

given in the section below

> **Toe correction**

As explained in section 4.1.1, Figure 4-73 presents a descriptive analysis of the stress-strain curve of the Mercurywave sample tested to flexure stress applied along the axis of its load-bearing fibres.
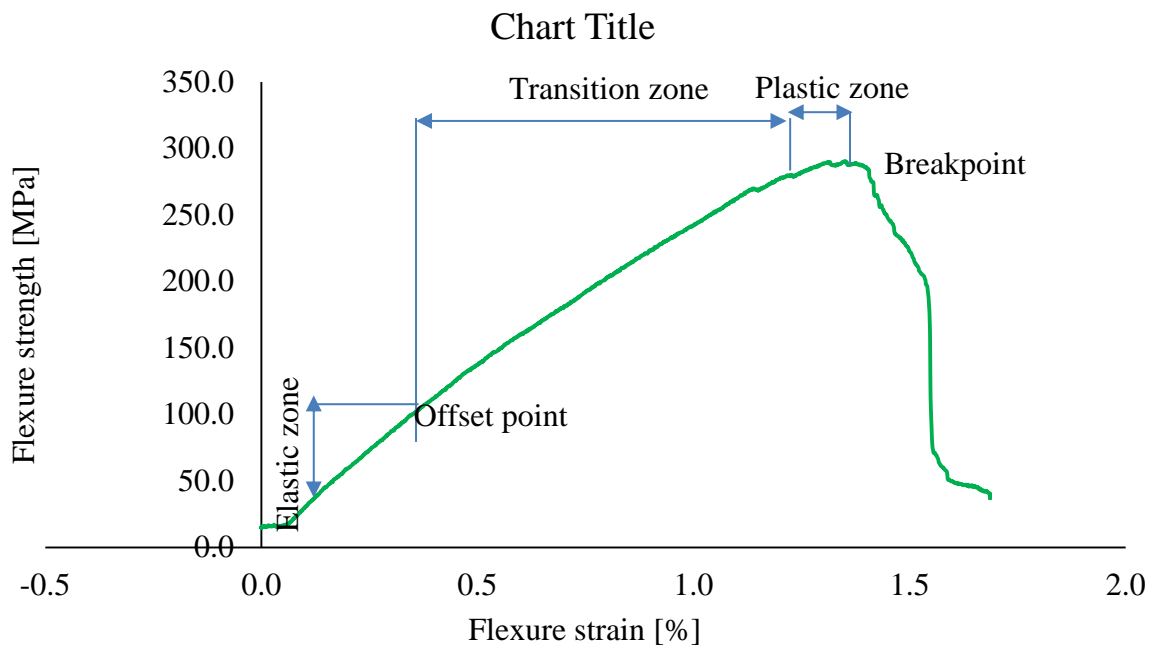
Figure 4-73: Stress-strain curve description

> **Bending stiffness**

Figure 4-74 shows different bending stiffness measured on the different specimens. It is clear

	L1	L2	L3	L4
☐ [N/mm]	17.9	18.3	19.8	18.1
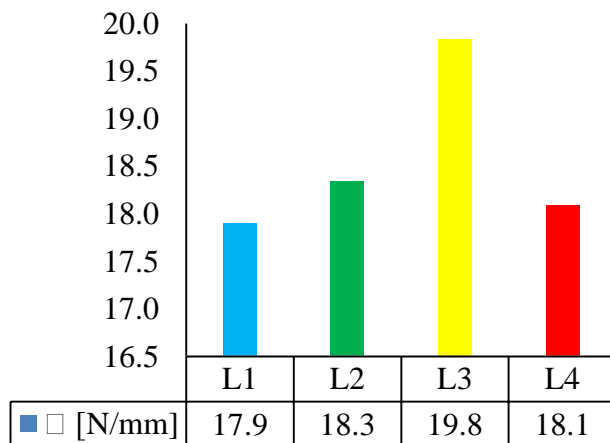
Figure 4-74: Bending stiffness

that L3 had the highest bending stiffness and L1 the lowest. A mean bending stiffness of 18.5451 N/mm with a standard deviation of 0.7641 was computed. Therefore, the region of L3 did resist more than other regions to the application of flexure stress.

➤ Yield strength

Data in Figure 4-71 showed that the four specimens yield in a very different manner. Figure 4-75 gives different offset points at which yield occurred and Figure 4-76 presents the different yield strengths deducted from the curves of Figure 4-71.

Analysis of Figure 4-76 showed that L4 deviated at the highest offset strain which corresponds to the highest yield strength, and L3 yielded at the lowest offset strain which corresponds to the lowest yield strength. The mean yield strength of 96.3285 MPa was

|	L1	L2	L3	L4
■ εo [%]	0.5	0.5	0.4	0.7
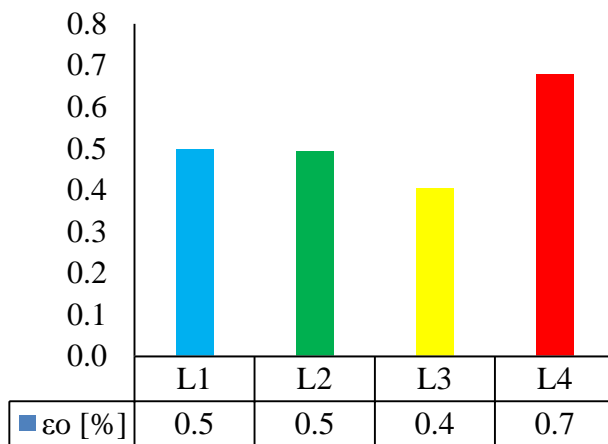
Figure 4-76: Offset strain

	L1	L2	L3	L4
■ σy [MPa]	96.1	95.0	73.7	120.5
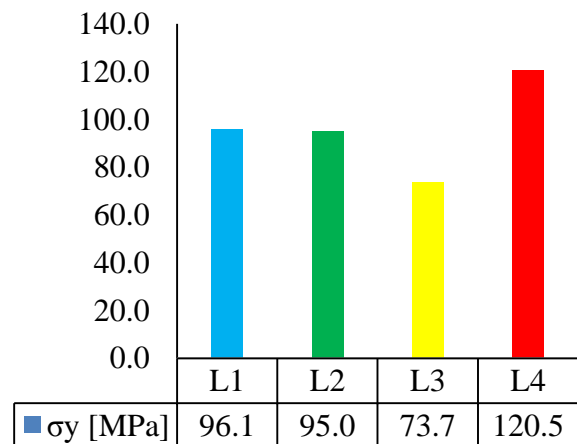
Figure 4-75: Yield strength

computed with a standard deviation of 16.5728 showing that the sample did yield differently according to the localised structural configuration. The T4 region deformed elastically more than other regions of the sample, but the plastic deformation was initiated from the region of T3.

➤ Flexure strength

The analysis of Figure 4-72 showed that L2 had the highest resistance to the application of the flexure stress and L3 the lowest. Figure 4-77 reveals the computed flexure strength of the sample tested across the axis from which the mean flexure strength was computed at 274.0759 MPa with a standard deviation of 32.2566. L3 region of the sample exhibited high

resistance to the application of flexure stress, but the standard deviation showed that the sample did not oppose the same resistance to the application of flexure stress.

> **Flexure strain**

The stresses induced in the specimen tested along its load-bearing fibres produced deflection of the specimen at a different rate (see Figure 4-71) where each specimen broke at a specific strain, but none reached the 5% strain. Figure 4-78 gives the value of strain computed from the curves, showing that L2 deflected more and L3 deflected less before breaking. A mean strain of 1.7777% with a standard deviation of 0.2310 was computed showing that when subjected to flexure stress, the sample did deflect according to the localised configuration of each region of the sample. Region L2 deflected more than all the others but fracture was initiated from region L3

	L1	L2	L3	L4
■ σf [MPa]	277.6	309.7	222.0	287.1
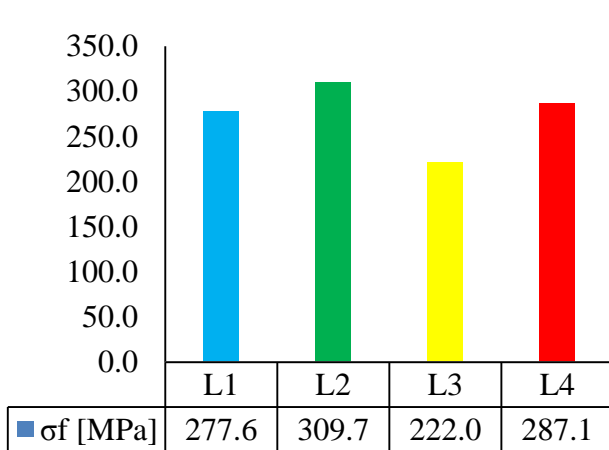
Figure 4-78: Flexure strength

	L1	L2	L3	L4
■ εf [%]	1.8	2.0	1.4	1.9
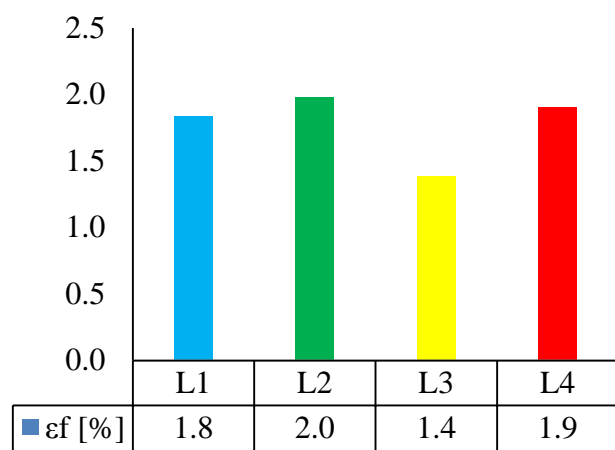
Figure 4-77: Flexure strain

> **Flexure modulus of elasticity**

Figure 4-73 shows that from the inflection to the offset point, the deflection of the specimen followed a linear path characterised by the modulus of elasticity of the specimen. Figure 4-80 suggests that L3 displayed the highest modulus of elasticity and L4 the lowest. The mean modulus of elasticity computed from analysis of Figure 4-80 was at 20.3030 GPa with a standard deviation of 1.3265 showing that the localised structural configuration of the sample impacted its elastic behaviour. The region of T4 did deform elastically more than the other regions of the sample, but plastic deformation was initiated from the L4 region of the sample.

> **Measurement of sample ductility**

Analysis of Figure 4-71 showed that the specimens resisted lower flexure stress compared to the specimens tested across the load-bearing fibres before the occurrence of fracture. Each specimen broke at a different deflection making an angle between the orientation of the specimen's support span and the orientation of the applied load. Figure 4-79 shows the different angles at which the specimens reached their maximum strain or break: T2 deflected with the highest angle and T4 with the lowest. The mean angle of deflection of the sample was computed noted at 46.2243^o with a standard deviation of 5.7954 showing that the specimen deflected with a magnitude right above half the support span of the testing fixture.

The standard deviation showed that the samples did not deflect with the same angle, but each localised region deflected according to its structural configuration. The magnitude of the mean angle showed that the Mercurywave sample tested across the axis of load-bearing fibres was less ductile than that tested along the axis.

	L1	L2	L3	L4
Ef [GPa]	20.4	21.2	21.5	18.1
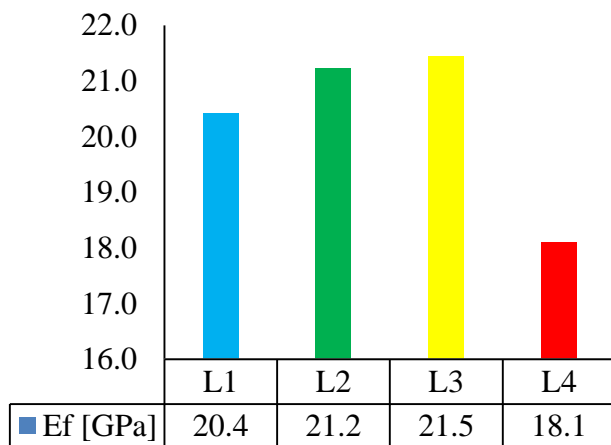
Figure 4-80: Flexure modulus of elasticity

	L1	L2	L3	L4
θ˚	47.9	51.2	36.4	49.4
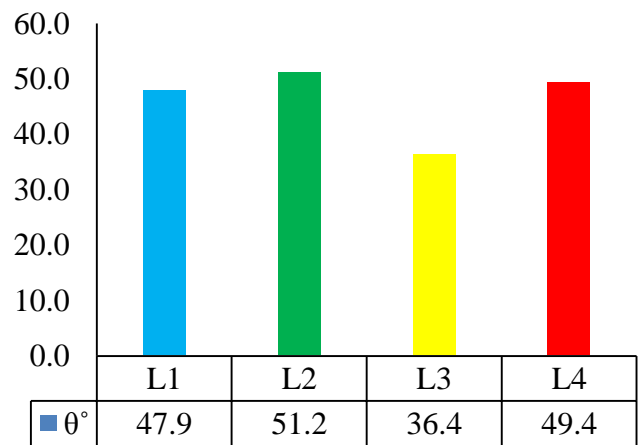
Figure 4-79: Deflection angle at fracture

4.3. Fractography analysis

To justify the difference in the strength exhibited by samples while subjected to the application of mechanical stress along and across the longitudinal axis of the sample, it was important to investigate the nature of its core element and its orientation. Research has revealed that the sample of the present paper was a composite material made of layers of different lamina where each lamina was constituted with reinforced particles (fibres) that characterise its strength or was the core element, with matrix particles that serve as load transmission mechanism between the fibres of the lamina, the interface matrix-fibres, and the interface between different layers. The orientation of the fibres determined the axis of the

laminate, but laminate can be either unidirectional or multidirectional (Adams *et al.*, 2002). Microscopic analysis of the sample (see Figure 4-81) indicated that the fibres were set in two directions called cross ply composite material, one set at 0° called the load-bearing fibres and the second at 90° fibres orientation (Greenhalgh, 2013). Therefore, the highest strength of the sample was found along its load-bearing fibres axis. Fractography analysis of failed specimens is presented in the sections below where the samples subjected to tensile stress will be analysed first, then those subjected to flexure stress will follow. Research informed
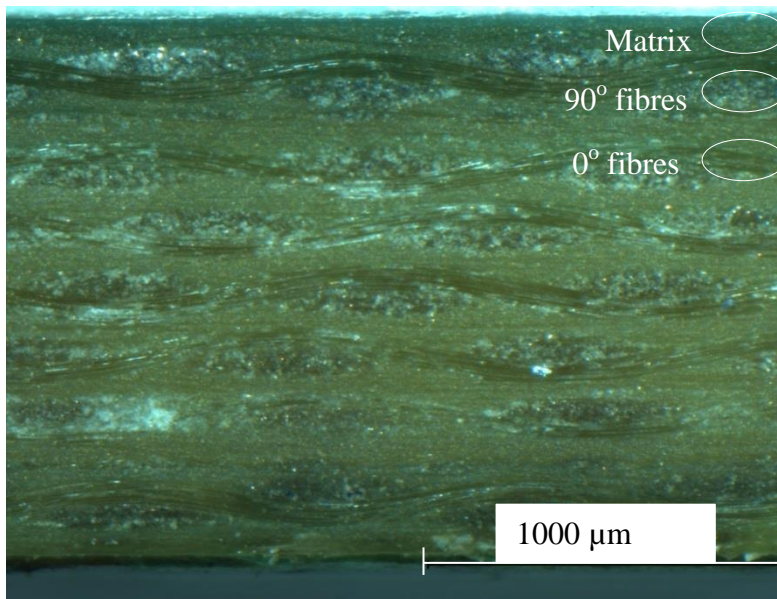
Figure 4-81: Microscopic view of sample fibre orientation at 110 pixels

that a composite material was characterised by three main factors: strength defined by the strength of its fibres, toughness defined by the strength of the matrix, and ductility defined by the strength of the interface between fibre and matrix.

4.3.1. Failure analysis of the specimen subjected to tensile stress

Different modes of failure were observed during testing, among which were specimens that broke within their weakest region, the region where the specimens had holes within them as per their design. According to Figure 4-84, other specimens failed within the grip jaw and were discarded, and other failed right below the grip jaw, but most specimens failed within the gage length region (see Figure 4-83). Few specimens failed at an angle within their gage length region (see Figure 4-82). Table 4.1 presents details of the different types of failure modes observed during the test. When analysing multidirectional composite material tested to tensile stress**,** the influence of delamination on the failure process was reflected by the degree of brooming.

The fractographic aspect observed during the investigation focused on the behaviour of the load-bearing fibres which directly affects the fracture sequence of the sample.

Other factors such as matrix cracks, delamination and interface de-bonding or crack were developed prior to the occurrence of a fracture's unstable state and were considered as a complementary aspect of this study.

Table 4-1: Different types of failure mode observed during the test

Typical failure Code	Description of the code			Observation
	Failure type	Failur	Failure	
LIT	Lateral	Inside	Top	Discarded
LAT	Lateral	At	Top	Low
LGM	Lateral	Gage	Middle	High
AGM	Angle	Gage	Middle	Low
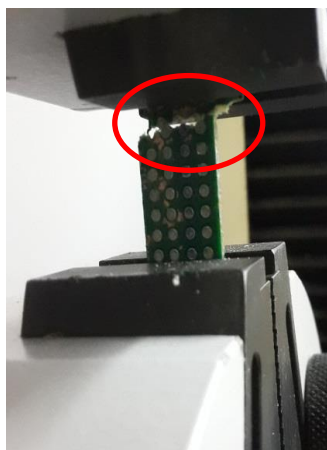
Figure 4-82: LAT specimen

Figure 4-83: AGM specimen
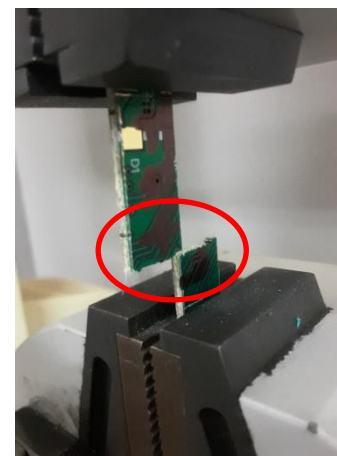
Figure 4-84: LGP specimen

> **Fractography analysis of sample tested along the load-bearing fibres**

Analysis of Figure 4.85 showed a failed sample tested to tensile stress where the ultimate strength was found to be high. According to the figure, not all fibres did fail on the same plan; individual fracture of fibres was observed and fracture propagation through the interface between the copper hollow cylinder and the surface of holes in which these copper cylinders were fitted was observed on one side. The objective of this analysis was to evaluate the reason the samples yielded high ultimate tensile strength while tested in a specific direction and less in the other normal to the first direction.

The fractured surface needed to be analysed from which the morphology of the load-bearing fibres, the matrix, the interface, and the laminate were investigated.

Figure 4.86 presents the failed surfaces area of the sample viewed at 20 pixels (a) and a magnified view of a portion of the failed surface area at 60 pixels (b). Zoom view displayed different aspects of the fractured surface area: analysis of the failed surface showed that the fibres had been fractured on different planes, fibre brooming had occurred at a lower degree, most fibres on the failed surface were bonded to the matrix, delamination of the outer copper layer was observed, and there was evidence of matrix cracking.

Figure 4-85: Sample tested along the 0° fibre axis view at 20 pixels

Figure 4-86: Fractured surface of the sample tested to tensile stress along the 0° fibre axis

The high degree of failed fibres at different planes showed that the fibres individually elongated before fracture. The lower degree of fibre brooming showed the low level of the failure process delamination. This proved that the load was applied along the axis of the load-bearing fibres and had caused their elongation before fracture. This supports the result obtained from the analysis of the stress-strain curve of this same specimen as noted in section 4.1.

➢ **Fractography analysis of specimen tested across the load-bearing fibres**

Figure 4-87 shows a failed specimen that was tested to tensile stress and yielded an ultimate strength lower than that of above analysis.

Analysis of this figure showed a high degree of pulled fibres, and the fracture had propagated within a straight path. One side of the specimen had two evident holes containing via hollow cylinder where fracture had followed the interface between the holes and the Via path.

Analysis of the failed surface was conducted as illustrated in Figure 4-88. Acronym 'a' denotes the full view of the fractured surface at 20 pixels, and acronym 'b' is 60 pixels zoom into a zone of full view where different aspects describing the morphology of the failure of this specimen were shown. Aspect such as cracked fibres, cracked matrix, pulled fibre and delaminated layer are observed. Two aspects characterised the localised zoom view; the high degree of brooming reflected the presence of layer delamination and the failure of fibres within the same plane indicating that failure was caused by interactions between the 90° and 0° axis fibres. Failure of the fibres was also noted but conventionally, when tested along the 90° fibre orientation, failure development is initiated by crack of the 90° fibres, followed by delamination between the 90° and the 0° fibres. Later the interaction between the 90° and 0° fibres did cause fracture of the interface between fibres and matrix which led to failure of the sample with a higher degree of fibre brooming. The analysis of the stress-strain curves, section 4.1, obtained from the tensile tested of this same specimen showed that fracture had occurred at the lower ultimate strength compared to that of the previous section.
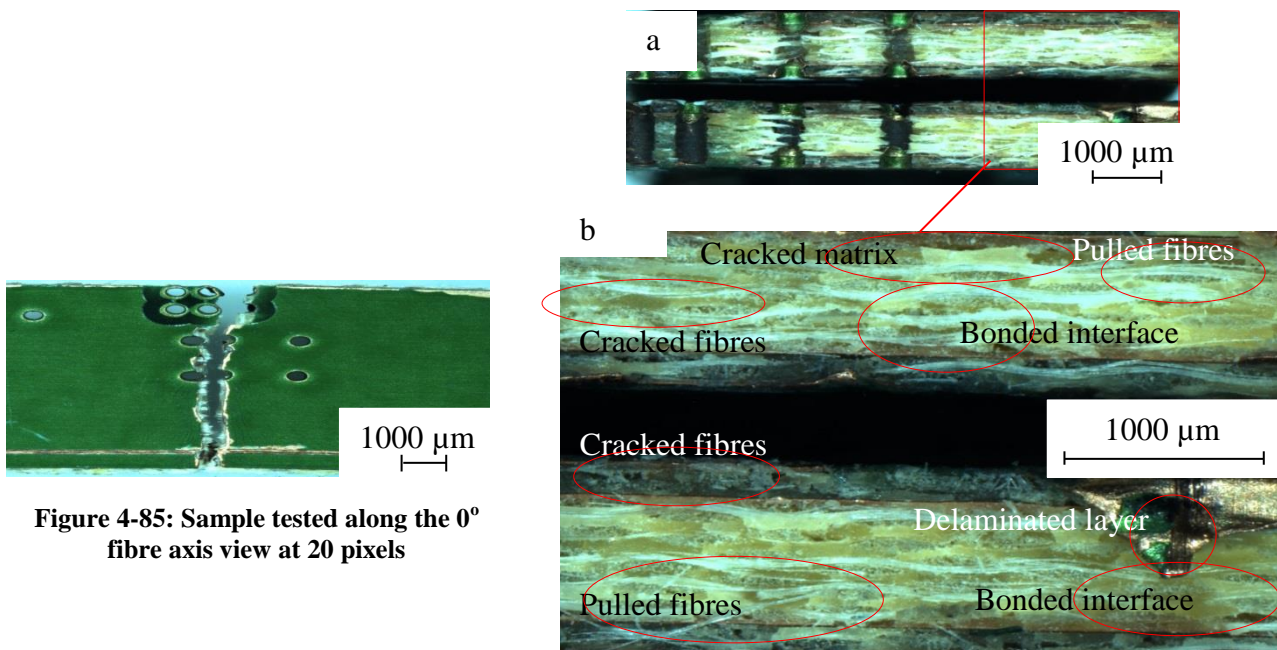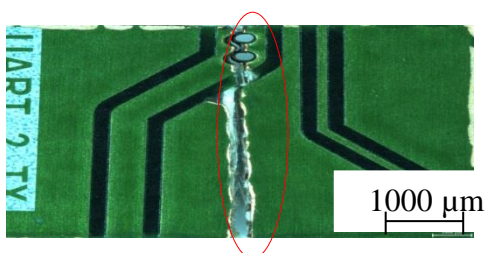

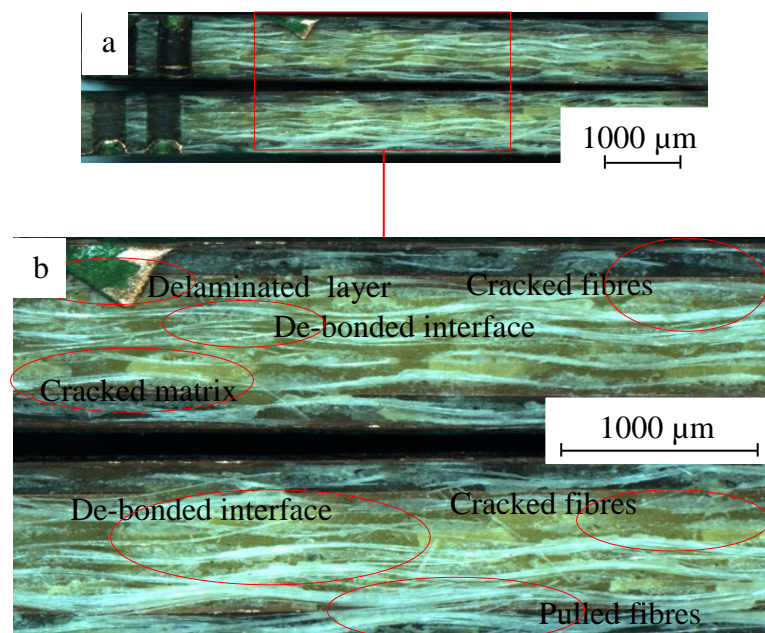**Figure 4-87: Sample tested along the 90° fibre axis view at 20 pixels**

Figure 4-88: Fractured section of the sample tested to tensile stress along the 90° fibre axis

4.3.2. Failure analysis of the sample tested to flexure stress

Failure morphology of the sample tested to flexure stress is characterised by the combination of tension and compression failure modes. Compression failure is characterised by ply splitting (delamination), debris (compressed fibres) and kink-band (micro-buckling instability in the fibres accompanied by axial splitting cracks in the matrix). Tension failure is characterised by fibres cracks, matrix crack, pulled fibres and delamination. Failure of cross ply material is prone to the development of ply splitting that makes the morphology of the fractured surface quite complex, a complexity resulting from the fact that flexure stress causes fracture within a certain number of planes of the laminate to the point where the laminate is regarded as several sub-laminates failed in flexure with surface exhibiting many bands of alternating compression-tension failure.

➢ **Specimen tested across the load-bearing fibres**

Figure 4-89 shows a profile of the failure propagation on the specimen that yielded the highest flexure strength view at 20 pixels noted '1' and at 110 pixels noted '2'. Two zones were illustrated: the tensile zone characterised by the fibrous reflective region and the compression zone by a flat dull region. Profile 2 shows a tension zone displaying transversally cracked fibres, cracked matrix and de-bonded interface but not much can be seen that describes the compression failure from the view of Figures 4-89 and 4-90.
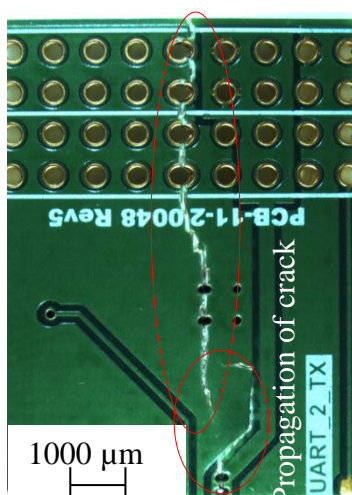

Figure 4-89: Fracture trajectory of the specimen tested across the fibres view at 6.3 pixels

Therefore, Figure 4-91 was provided to offer more detail on the compression failure of the upper midsection of the specimen that was in direct contact with the apply load and that of the tension failure of the lower midsection of the specimen. Figure 4-89 displays the trajectory followed by the fracture as it was propagating throughout the width of the specimen. The propagation of a crack was not continuous; as a deviation was noted, it can be assumed that layer delamination was induced in the specimen as failure was propagating throughout its thickness. Figure (4-91) displays the fracture surface area of the specimen tested along the load-bearing fibres, letter 'a' denotes full view of the crack area at 20 pixels microscopic view, T1 denotes the portion of the fracture area zoom from the tension zone of the upper part, C1 is the portion zoom from the compression zone of the upper part, T2 is the portion zoom from the tension zone of the lower part; and C2 is the portion zoom from the compression zone of the lower part. T1 and T2 displayed high degrees of fibres cracked, matrix cracked, split fibres and de-bonded matrix-fibres interfaces, but C1 and C2 displayed
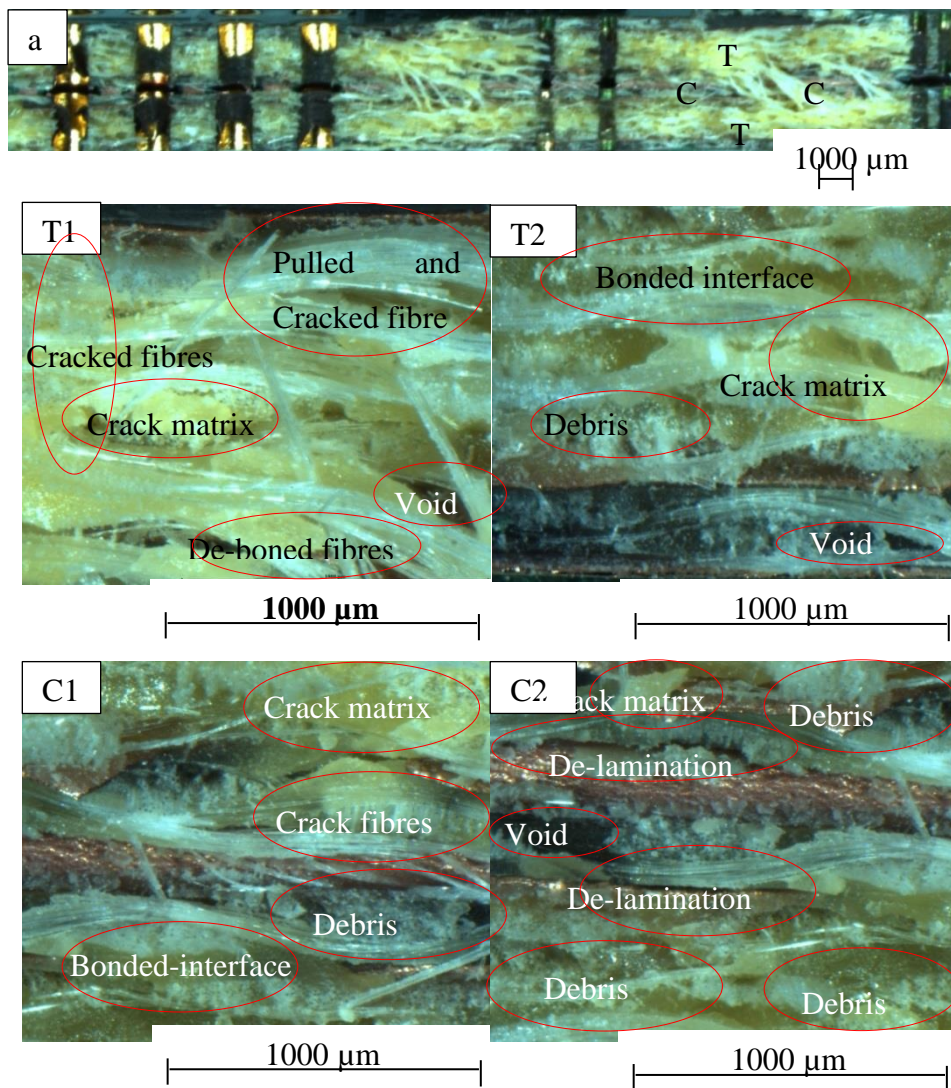

Figure 4-90: Fractured surface of the specimen tested across the 0° fibres

high levels of debris resulting from the compressed fibres and matrix, delamination, and bonded fibres-matrix interfaces. This showed that this specimen had an interlaminar fracture, a trans-laminar fracture combined with an intra-laminar fracture illustrating fracture caused by flexure stress applied in a direction transversal to the axis of the load-bearing fibres.

> **Specimen tested along the load-bearing fibres**

Figure 4-93 presents the profile of the failed specimen through its thickness for the specimen tested along its load-bearing fibres. Acronym '1' denotes the propagation of failure view at 20 pixels displaying two regions: the tension zone characterised by the shiny region and the compression zone characterised by the dull region. Acronym '2' denotes the fracture profile
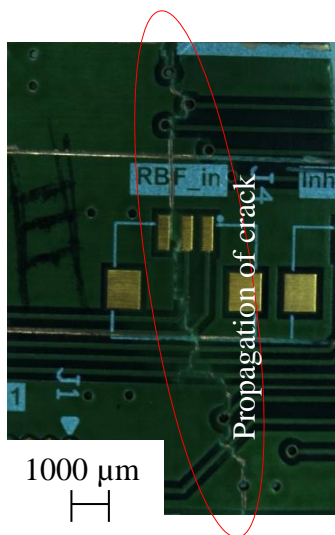
Figure 4-92: Fracture trajectory of the high flexure strength specimen view at 6.3 pixels
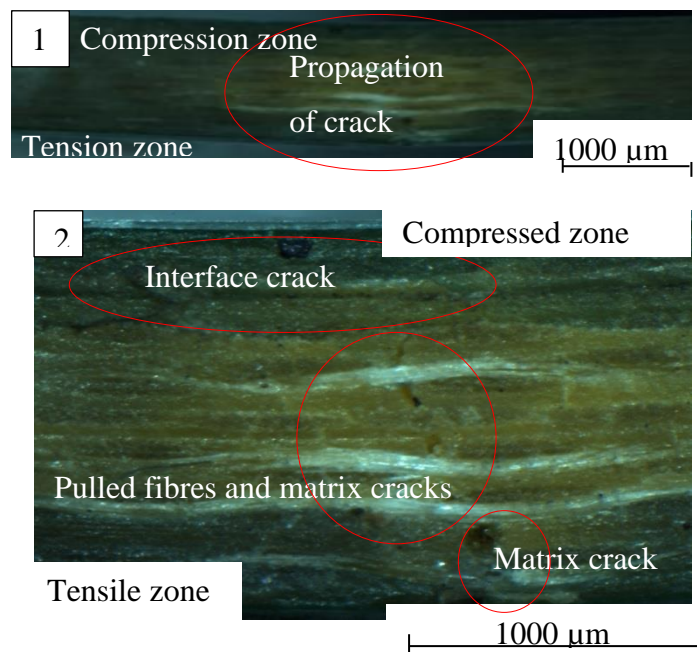
Figure 4-91: Profile of the failed region of the low flexure strength sample

view at 110 pixels displaying the propagation of fracture within the thickness of the specimen. The tension zone was illustrated by matrix cracked and pulled fibres and the compression zone by delamination along the axis of the load-bearing fibres and fretted fibres and matrix. Figure 4-92 shows the trajectory of the propagation of failure within the width of the specimen. It was evident that fracture propagated in a continuous trajectory. As Figures 4-92 and 4-93 did not give a proper view of the failure morphology of the load-bearing fibres, the matrix, the interfaces, and the layers. Therefore Figure 4-94 was provided where T1, C1, T2 and C2 represent the same elements as presented in the section above.

T1 and T2 showed high degrees of load-bearing fibres pulled, matrix crack and fractured 90° fibres; T2 had the particularity of displaying significant debris showing that a compressive failure had been recorded in that region. C1 and C2 confirmed the presence of debris, pulled 0° fibres and cracked layer interface illustrated by the delamination. This clarified that the fracture was caused by a flexure stress applied in a direction parallel to 0° fibre axis.

Figure 4-93: Fractured surface of the specimen tested along the 0° fibres

5. DISCUSSION

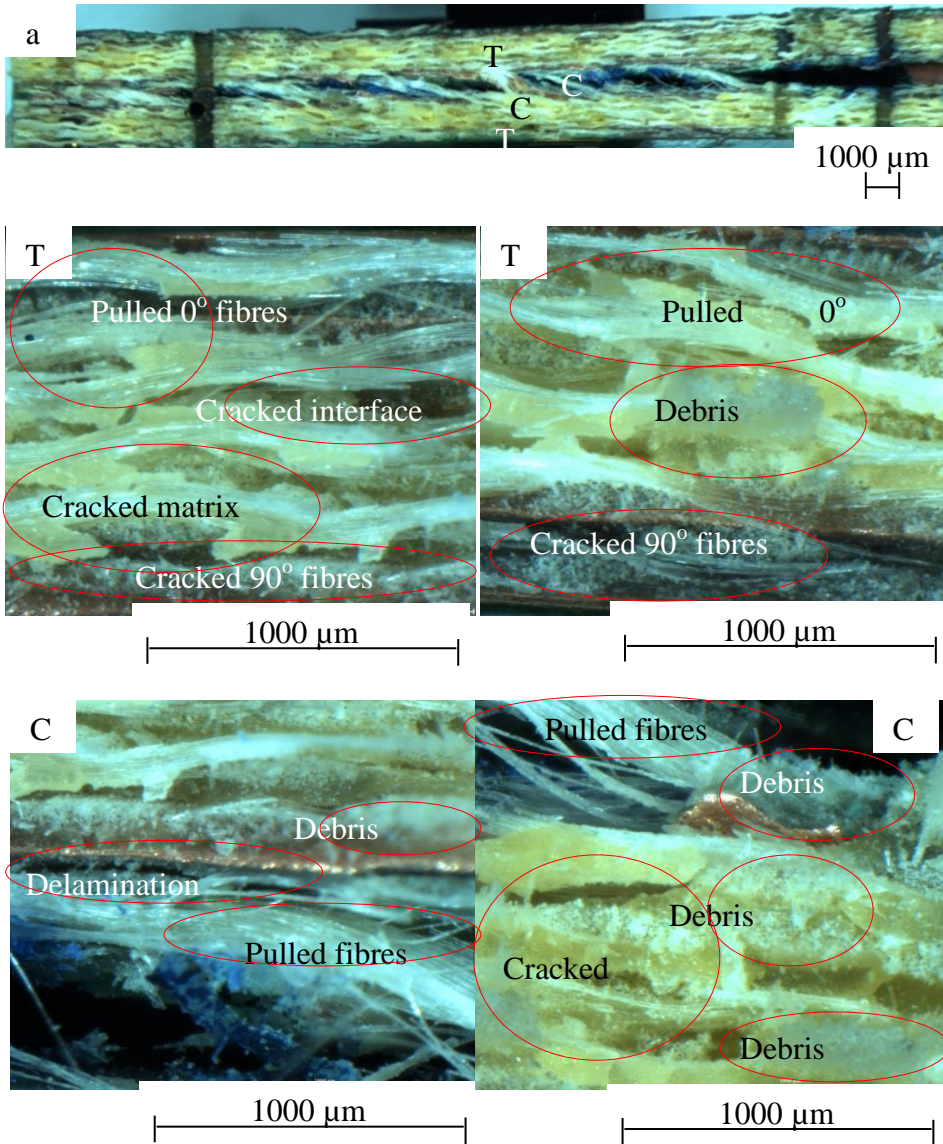Analysis of the samples' behaviour to tensile and flexure stress conducted and reported in Chapter 4 focused on factors such as the direction of the applied load relative to that of the load-bearing fibres of the sample, the strength and elastic properties of the sample, and the morphology of the fractured surface. These factors are discussed in this chapter; findings of the discussion constituted the recommendations and conclusions of this research work. The first section of this chapter discussed the reaction of the boards to tensile stress; the second section that of the flexure stress; and the third and final section compared the outcomes from the two previous sections and generate remarks that will lead to recommendations and conclusions.

5.1. Tensile test result discussion

Two samples each with twelve specimens were analysed in Chapter 4; each sample had six specimens tested along and six across the axis of the load-bearing fibres. Properties such as Young's modulus of elasticity, Poisson's ratio, ultimate tensile strength, ultimate tensile strain, offset yield strength and post-fracture percentage elongation were analysed for each sample, with comparisons between the properties evaluated along the axis of fibre against those evaluated across the fibres for each sample and the properties of the FR-4 samples against those of the Mercurywave samples.

5.1.1. Reaction of the sample relative to the orientation of the fibre

1) FR-4 sample

The stress-strain curves of Figure 5-1 compared the reaction of the FR- sample tested along its load-bearing fibres (0° fibres) referred to as FR-4_T_0 to the one tested across (90° fibres) referred to as FR-4_T_90. The figure shows that the sample tested along the 0° fibres is steeper than that tested across by the fact that the analysis of the curves showed a steep increase in the stress of the sample tested along the 0° fibres once the strain exceeded 3%, but for the sample tested across the 0° fibres the steep increase was noted at a strain of 9% with a lower magnitude than that of the one tested along the 0° fibres. Another aspect noted from the analysis of Figure 5-1 was that the sample tested along the 0° fibres was stiffer than that tested across the fibres; this was evident in the fact that the sample tested along the 0° fibres deformed less at high stress while the sample tested across deformed more at lower stress.

The final aspect deduced from the analysis of the curves in Figure 5-1 was that the sample tested across the fibres was more ductile compared to the one tested along the fibres, evident in the fact that between 4 and 9% strain the stress was almost constant for the sample tested across the fibres. These three observations are supported by the fractography analysis in section 4.4 of Chapter 4 where it was found that to reach the unstable state of fracture in the sample tested along the 0° fibres. The strength of the load-bearing fibres that characterised the strength of the sample had to be overcome by the stress-induced in the sample. And for the one tested across the load-bearing fibres, the bond strength of the interface between the fibres and the matrix that determined the degree of ductility of the sample had to be overcome to cause a crack of the interface and so obtain an unstable failure state of the sample. To further discuss the reaction of these two samples, the following properties were compared.
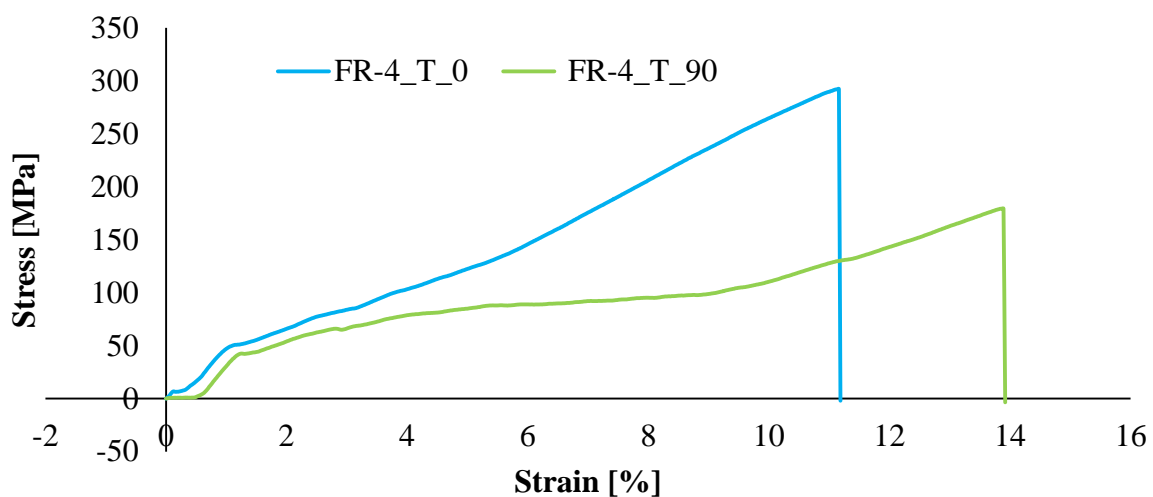
Figure 5-1: Stress-strain curves of the FR-4 sample

➢ **Ultimate tensile strength of the FR-4 sample**

Figure 5-3 displayed the mean ultimate tensile strengths of the sample tested along the 0° fibres, X_L, and across the 0° fibres, X_T. According to data in Figure 5-3, X_L had the highest ultimate strength; this meant that the FR-4 sample did oppose high resistance to the application of tensile stress along its load-bearing fibres.

➢ **Ultimate tensile strain of the FR-4 sample**

Figure 5-2 compared the mean ultimate strain measured in the FR-4 sample tested along and across the 0° fibres. Analysis showed that the strain induced in the sample tested along the 0° fibres was the highest, showing that the FR-4 sample subjected to tensile stress applied along its axis did elongate more before it fails.

	FR-4_X_TL	FR-4_X_TT
εUlt [%]	9.8	8.0
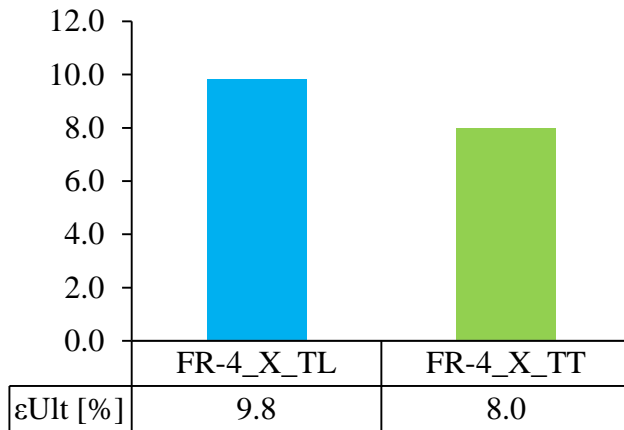
Figure 5-3: Mean ultimate strain

	FR-4_X_TL	FR-4_X_TT
σ [MPa]	200.9	151.3
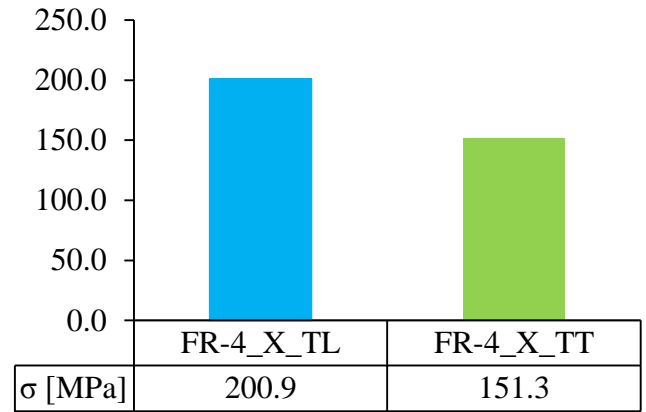
Figure 5-2: Mean ultimate strength

➢ **Offset tensile yield strength**

Analysis of Figure 5-5 showed that the extent of elastic deformation observed in the sample subjected to tensile stress was observed as high in the sample tested across the load-bearing fibres and lower in the one tested along. Again, this meant that the FR-4 sample did deform elastically more when subjected to tensile stress across its load-bearing fibres.

	FR-4_X_TL	FR-4_X_TT
σy [MPa]	33.2	41.2

Figure 5-4: Mean offset yield strength

	FR-4_X_TL	FR-4_X_TT
εO [%]	0.5	0.7

Figure 5-5: Mean offset strain

➢ **Mean post-fracture percentage elongation**

Figure 5-6 displayed the mean post-fracture percentage elongation; this property illustrated the extent of plastic deformation the sample endured before fracture was observed. According to Figure 5-6 data, the sample tested along the 0° fibres deformed plastically more than that tested across the 0° fibres. This was supported by the f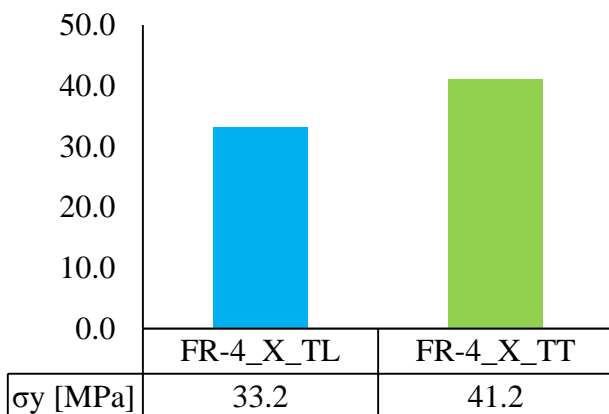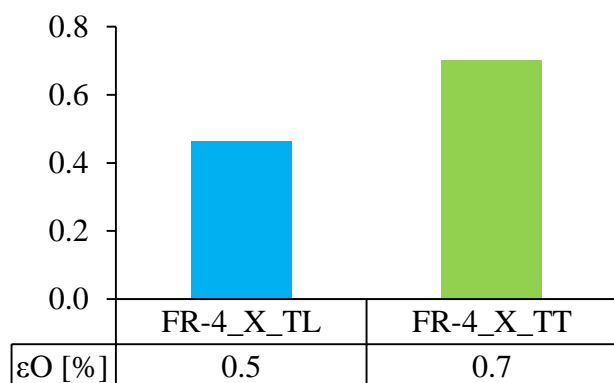ractography analysis of the failed surface area in section 4.3 of Chapter 4 where the microscopic analysis of the sample tested along the load-bearing fibres had shown that each fibre broke within a different plane. This demonstrated the plastic deformation of the fibres before fracture, but for the sample tested across the load-bearing fibres, a high degree of fibre brooming was observed on the surface area of the failed sample showing that the interface fibres-matrix deformed plastically before they broke. Further analysis of Figure 5-5 shows that the interface fibres-matrix of the FR-4 sample had a strong bond; thus, the sample was deemed highly ductile.

	FR-4_X_TL	FR-4_X_TT
%δ	9.8	8.0
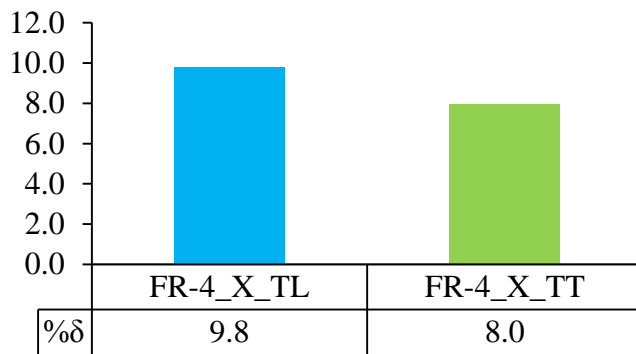
Figure 5-6: Mean post-fracture percentage elongations

➢ **Young's modulus of elasticity**

From observation of Figure 5-8, it was evident that Young's modulus of the FR-4 sample was evaluated around 6 GPa but the direction along which the tensile stress was applied relative to the orientation of the load-bearing fibres of the sample influenced the elastic behaviour of the sample. Analysis showed that the difference between Young's modulus of elasticity measured along and across the 0° fibres was just about 0.4439 GPa. Therefore, the sample had similar elastic behaviour along and across its 0° fibres with the observation that along the $0°$ fibres, the sample reacted elastically a little bit better than across.

➢ **Poisson's ratio**

Analysis of Figure 5-7 showed that the Poisson's ratio measured along the 0° fibres was high compared to the one tested across. According to this analysis, the lateral deformation of the FR-4 sample subjected to tensile stress was high when the load was applied along the load-bearing fibres of the sample.

E [GPa]	FR-4_X_TL	FR-4_X_TT
	6.8	6.3
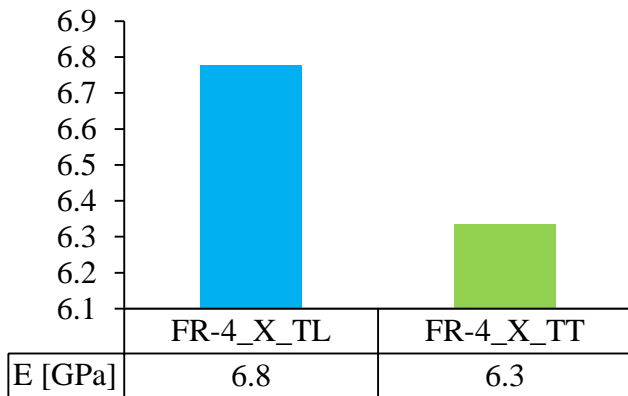
Figure 5-8: Mean Young's modulus of elasticity

v [%]	FR-4_X_TL	FR-4_X_TT
	0.9	0.7
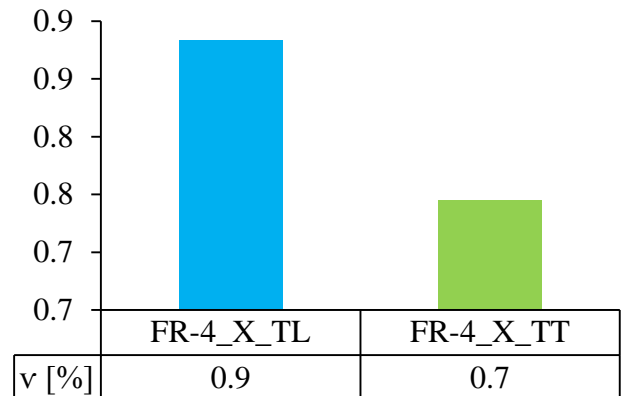
Figure 5-7: Mean Poisson's ratios

2) Mercurywave sample

The stress-strain curves of Figure 5-9 compared the reaction of the Mercurywave sample tested along the load-bearing fibres (0° fibres), referred to as MW_T_0, to the one tested across, and referred to as MW_T_90. The figure shows a similar reaction in the behaviour of the stress-strain curves of the sample tested along and across the 0° fibres: the steepness and
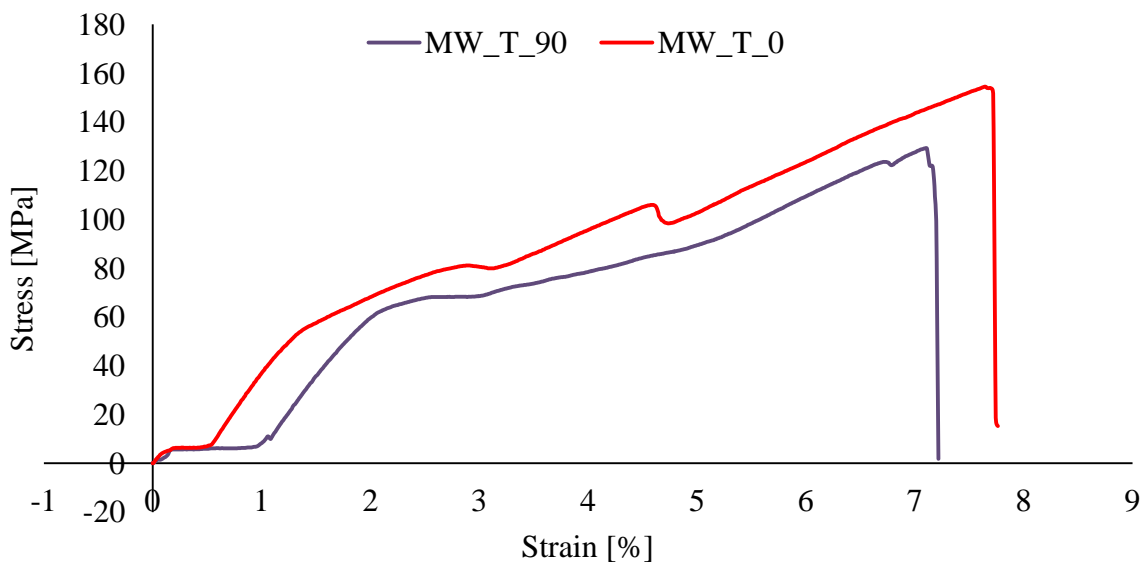
Figure 5-9: Stress-strain curves of the Mercurywave samples tested along vs across the 0° fibres axis

78

stiffness of the two samples were almost the same as the two curves following almost the very same path, but the sample tested along the 0° fibres showed high ultimate strength and higher ultimate strain. A detailed comparison of the different evaluated properties below did help establish the difference the Mercurywave sample yielded when tested in the two directions.

➢ **Ultimate tensile strength of the Mercurywave sample**

Analysis of the mean ultimate strength displayed in Figure 5-10 showed that X_L had the highest ultimate strength; this means that as for the FR-4 sample, the Mercurywave sample did oppose high resistance to the application of tensile stress along its load-bearing fibres axis.

σult [MPa]	X_T	X_L
	101.5	134.0
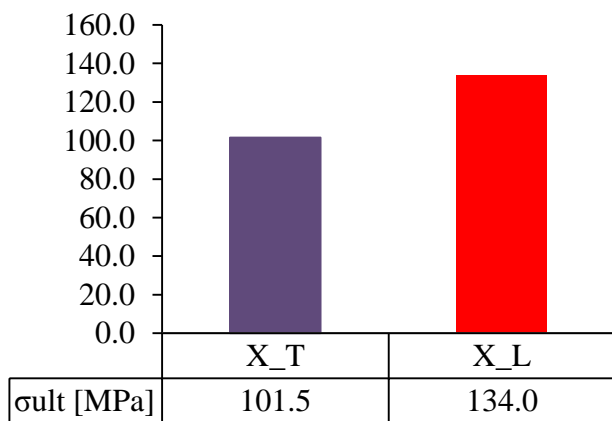
Figure 5-10: Mean ultimate tensile strength

εUlt [%]	X_T	X_L
	5.1	7.1
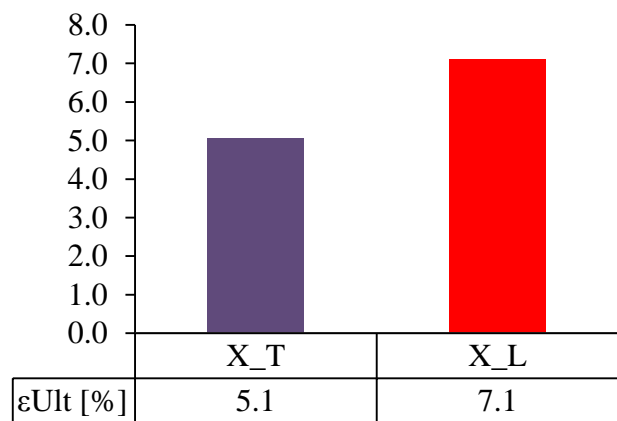
Figure 5-11: Mean ultimate tensile strain

➢ **Ultimate tensile strain of the Mercurywave sample**

Figure 5-11 compared the mean ultimate strain measured on the Mercurywave sample tested along and across the 0° fibres. Analysis showed that the strain recorded in the sample tested along the 0° fibres was the highest; this means that when subjected to tensile stress, the Mercurywave sample did elongate more along its 0° fibres axis before it fails.

➢ **Offset tensile yield strength**

Analysis of Figure 5-13 showed that the extent of elastic deformation recorded in the sample subjected to tensile stress was observed as high in the sample tested along the load-bearing fibres and lower in the one tested across. As with the FR-4 sample, the Mercurywave sample

did elongate elastically more when subjected to tensile stress applied along the axis of its
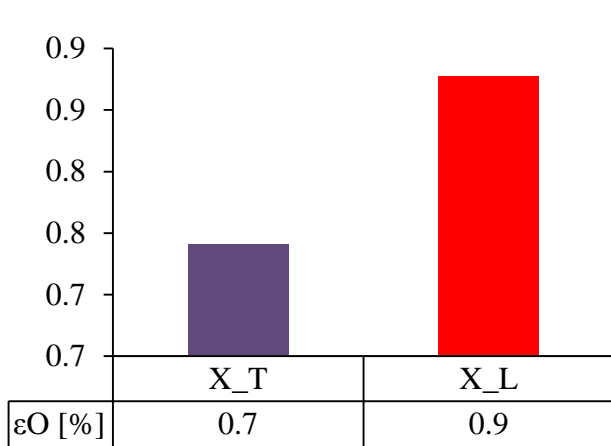
Figure 5-13: Mean offset strain

	X_T	X_L
εO [%]	0.7	0.9
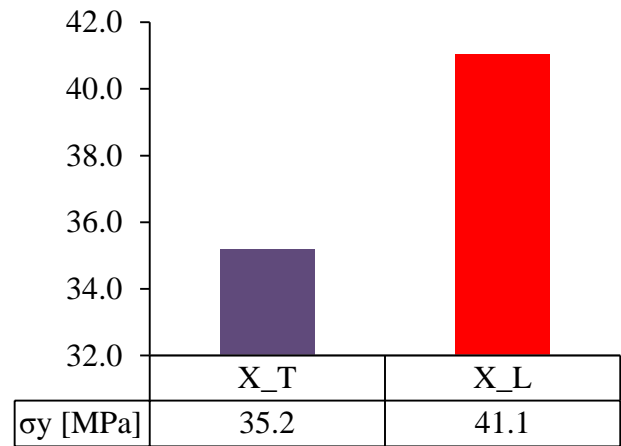
Figure 5-12: Mean offset yield strength

	X_T	X_L
σy [MPa]	35.2	41.1

load-bearing fibres.

➢ Mean post-fracture percentage elongation

Figure 5-14 displayed the mean post-fracture percentage elongation which gave the extent of plastic deformation experienced by the sample before its fracture. According to Figure 5-12, data verified that the sample tested along the 0° fibres deformed plastically more than that tested across the 0° fibres. This was supported by the fractography analysis of the failed surface, as in section 4.4 of Chapter 4; microscopic analysis of the sample tested along the load-bearing fibres had shown that each fibre broke at an individual plane. It demonstrated the plastic deformation of individual fibre before fracture. But for that tested across the load-

	X_T	X_L
%δ	5.0	7.1

Figure 5-14: Mean post-fracture percentage elongations

bearing fibres, a high degree of fibre brooming was observed on the surface area of the failed sample showing that the interface fibres-matrix deformed less plastically before they broke. Further analysis of Figure 5-12 showed that the interface fibres-matrix of the Mercurywave sample had a strong bond; consequently, the sample was found to be highly ductile.

> **Young's modulus of elasticity**

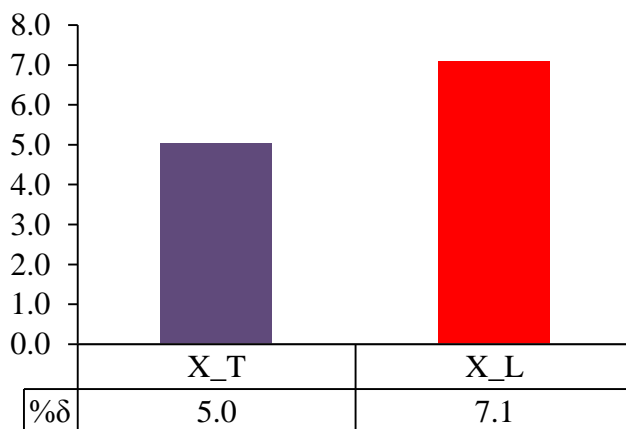From observation of Figure 5-16, it was evident that Young's modulus of the Mercurywave sample was evaluated around 5 GPa, but the direction along which the tensile stress was applied relative to the orientation of the load-bearing fibres of the sample slightly influenced the elastic behaviour of the sample. Analysis showed that the difference between the Young's modulus of elasticity measured along and across the 0° fibres was approximately 0.2115 GPa.

v [%]	X_T	X_L
	1.0	0.8
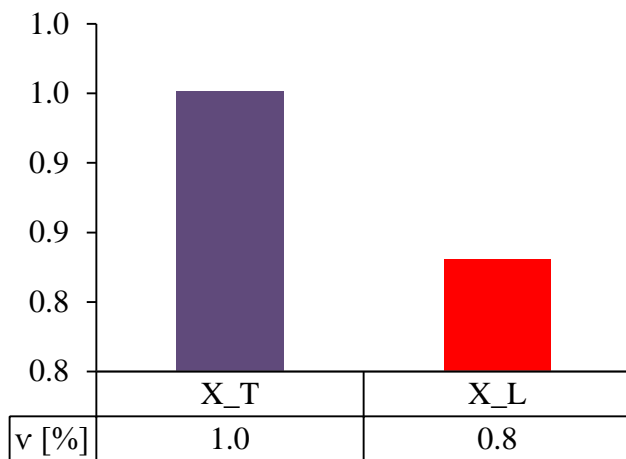
Figure 5-16: Mean Poisson's ratios

E [GPa]	X_T	X_L
	5.6	5.9
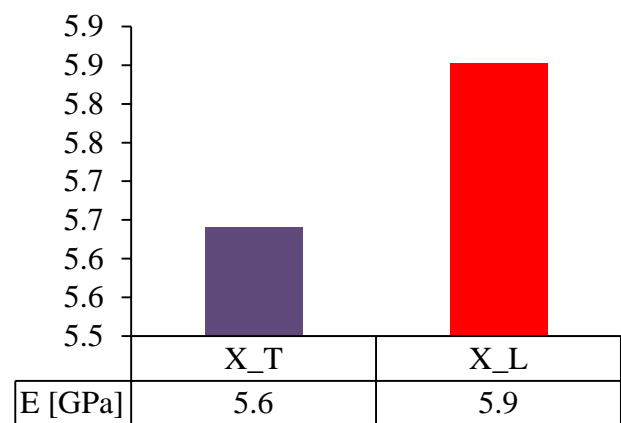
Figure 5-15: Mean Young's modulus of elasticity

> **Poisson's ratio**

According to data in Figure 5-15, the Poisson's ratio measured along the 0° fibres was lower than that of the one tested across. This analysis confirmed that the lateral deformation of the Mercurywave sample subjected to tensile stress was high when the load was applied across the load-bearing fibres of the sample

5.1.2. Reaction of the samples relative to the substrate used

Figure 5-17 showed stress-strain curves describing the behaviour of the four samples discussed above. It was clear that the FR-4 sample tested along the 0° fibre was steeper and

stiffer than the Mercurywave sample tested along the same axis; this observation was supported by the comparison between their mean ultimate strength. The above discussion showed several pertinent points. For example, the mean ultimate strength of the FR-4 sample was 33.301% greater than that of the Mercurywave sample tested along the load-bearing fibres and 32.931% across. It was therefore evident that the ultimate tensile strength of the FR-4 sample was about 33% greater than that of the Mercurywave sample; therefore, it was concluded that the FR-4 sample opposed higher resistance to the application of tensile stress than the Mercurywave sample.

The mean ultimate strain of the FR-4 sample was determined as 27.488% greater than that of the Mercurywave sample tested along the 0° fibres and 36.607% across. Compared to the mean ultimate strength, the rate at which the strains differ between the two specimens measured along versus across the load-bearing fibres was large. It can be concluded that the FR-4 sample was found to be more ductile than the Mercurywave sample for it elongated more before fracture while subjected to tensile stress.

The mean offset yield strength of the FR-4 sample was 19.162% smaller than that of the Mercurywave sample tested along the load-bearing fibres and 14.460% greater across. This suggested that the Mercurywave sample expanded more elastically than the FR-4 sample when subjected to tensile stress applied along the load-bearing fibres and less when the stress is applied across.
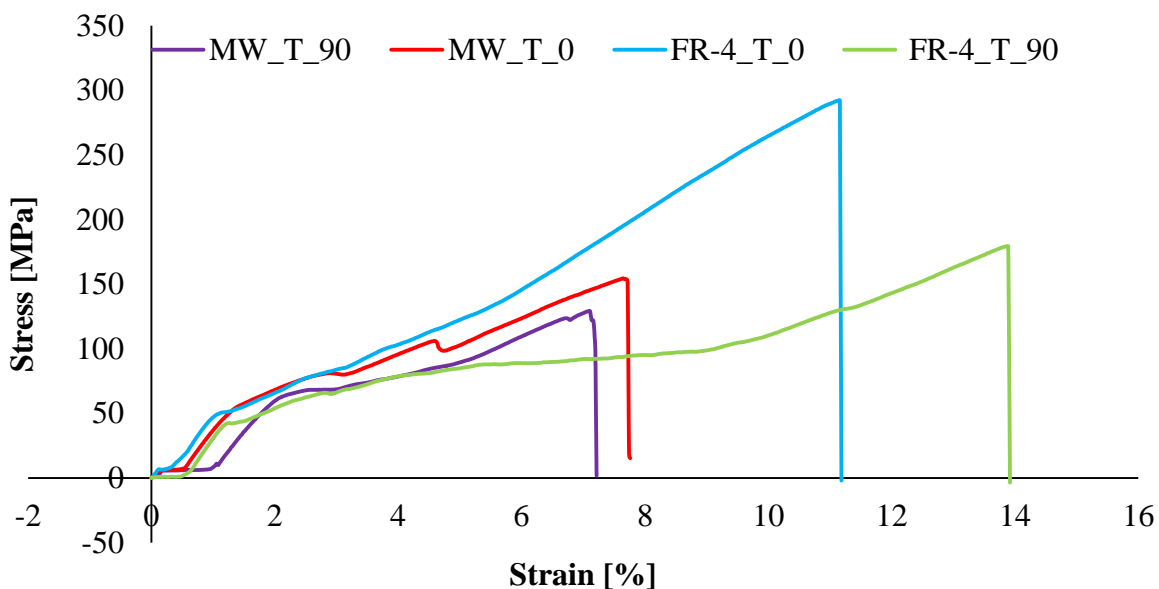

Figure 5-17: Stress-strain curves of FR-4 vs. Mercurywave samples

The mean post-fracture percentage elongation of the FR-4 sample was determined as 27.523% greater than the Mercurywave sample tested along the load-bearing fibres and 36.641% across. It can therefore be said that the extent of plastic deformation of FR-4 sample subjected to tensile stress was much larger than that of the Mercurywave sample. This confirmed the observation made for the strain and the analysis of the curves of Figure 5-15 where it was clearly seen that the FR-4 sample was more ductile than the Mercurywave sample.

The mean Young's modulus of elasticity of the FR-4 sample was 13.668% greater than that of the Mercurywave sample tested along the load-bearing fibres and 10.957% across. This was in slight contrast with the observation made in the discussion of the yield strength. Based on the Young's modulus of elasticity computed, the FR-4 sample reacted elastically much better to tensile stress than the Mercurywave sample.

The mean Poisson's ratio of the FR-4 sample was 5.942% smaller than the Mercurywave sample tested along the 0° fibres and 21.733% across. The mean Poisson's ratios of the two samples measured along the 0° fibres were closed; this means that along the fibres, the two samples had the same reaction to mechanical stress.

5.2. Flexural test result discussion

Four samples each with four specimens were tested and the results analysed in Chapter 4. The first sample consisted of FR-4 PCB substrate tested along the axis of the load-bearing fibres; the second of FR-4 PCB substrates tested across; the third one of Mercurywave PCB substrate tested along; and the fourth one of Mercurywave PCB substrate tested across the 0° fibres. Properties such as flexure modulus of elasticity, flexure strength, flexure strain, bending stiffness, offset flexure yield strength and deflection angle at fracture were analysed for each sample. This section discusses the properties evaluated along the axis of the load-bearing fibre against those evaluated across each sample, and the properties of the FR-4 samples against those of the Mercurywave samples.

5.2.1. Reaction of the sample relative to the orientation of the fibre

1) **FR-4 sample**

The stress-strain curves of Figure 5-18 compared the reaction of the FR-4 sample tested along the load-bearing fibres (0° fibres) to the one tested across (90° fibres). According to the data,
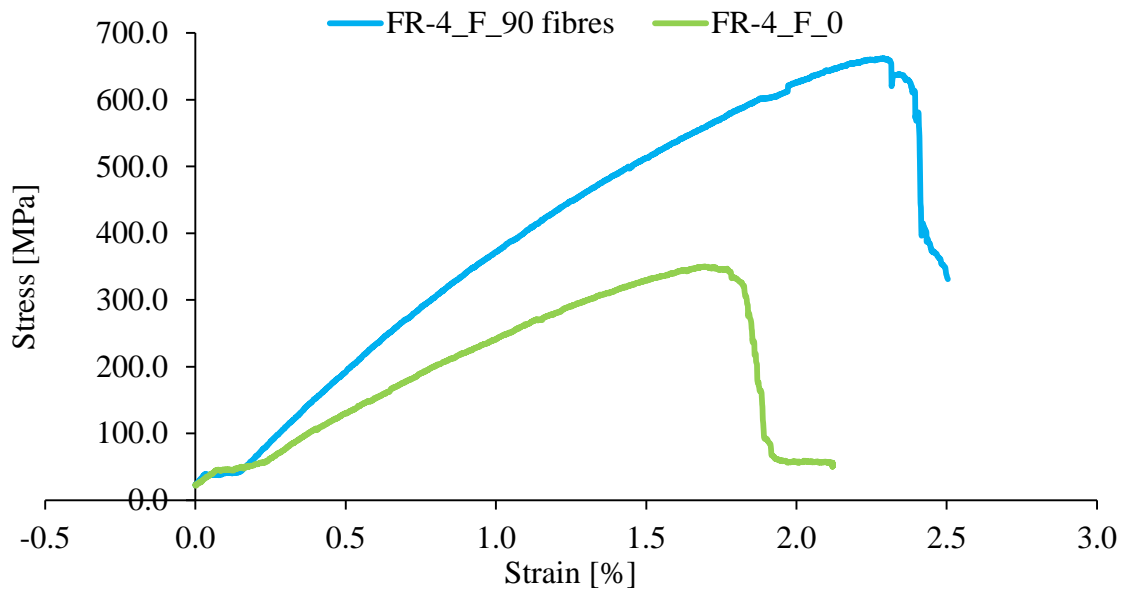

Figure 5-18: Stress-strain curves of the FR-4 sample subjected to flexure stress

the sample tested across the 0° fibres was found to be stiffer than that tested across the fibres; this was observed by the fact at the same stress the sample tested across the 0° fibres deformed less than that tested along. Another aspect deduced from the analysis of the curves of Figure 5-16 was that the sample tested across the fibres was more ductile than one tested along the fibres, evident by the fact that the two curves had similar shapes, but the sample tested across the 0° fibres broke at higher stress and strain while the one tested along broke at lower stress and strain. These two observations were supported by the fractography analysis in section 4.4 of Chapter 4 and related in the above discussion. To further discuss the results obtained from the two samples subjected to flexure stress, several properties were compared as presented below.

➢ **Bending stiffness of the FR-4 sample**

The mean bending stiffness of the sample tested along the 0° fibres (X_L) and that of the sample tested across (X_T) are displayed in Figure 5-19. Analysis showed that X_T had the highest bending stiffness. This means that the FR-4 sample did oppose high resistance to the application of flexure stress across its load-bearing fibres more than along. This was because the deflection of the sample subjected to flexure stress applied across its load-bearing fibres was a function of the transversal strength of load-bearing fibres.
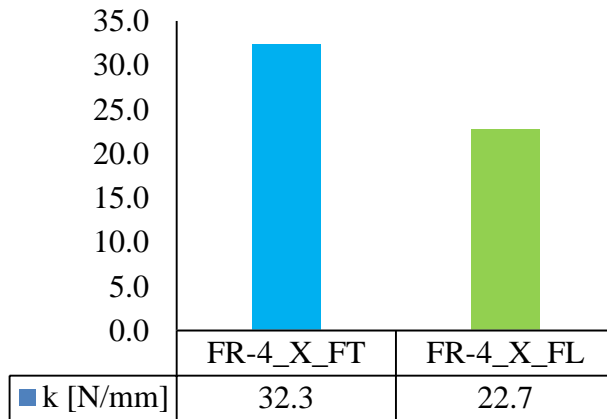
	FR-4_X_FT	FR-4_X_FL
■ k [N/mm]	32.3	22.7

Figure 5-19: Mean bending stiffness

➢ **Flexure strength**

The mean flexure strengths displayed in Figure 5-20 show the difference between the mean flexure strength of the sample tested along the 0° fibres and that of the sample tested across. According to analysis, X_T had a flexure strength which was approximately twice that tested along, suggesting that the FR-4 sample did oppose high resistance to the application of flexure stress across its load-bearing fibres more than across. Fractography analysis confirmed that when tested across its load-bearing fibres, the FR-4 sample's total unstable fracture state was achieved when the transversal fracture of its load-bearing fibres was observed. Thus the assessment of the bending strength of the FR-4 sample tested across its 0° fibres was a function of the radial strength of the load-bearing fibres of the sample.

➢ **Flexure strain**

Figure 5-21 compared the mean flexure strain measured in the FR-4 sample tested along and across the 90° fibres. According to analysis, the strain induced in the sample tested across the 0° fibres was the highest; therefore, the FR-4 sample subjected to a flexure stress applied across its 0° fibres had a large deflection before its fracture.
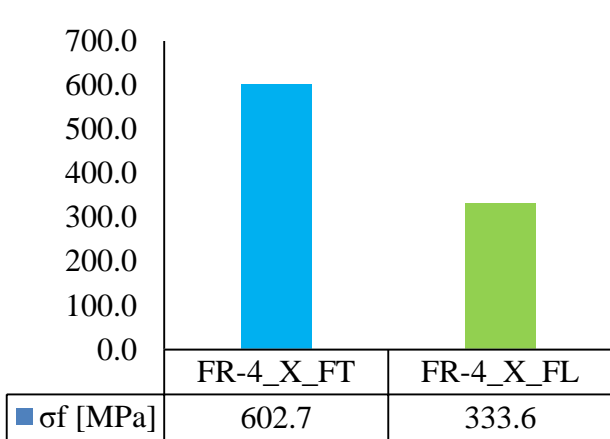
	FR-4_X_FT	FR-4_X_FL
■ σf [MPa]	602.7	333.6

Figure 5-21: Mean flexure strength

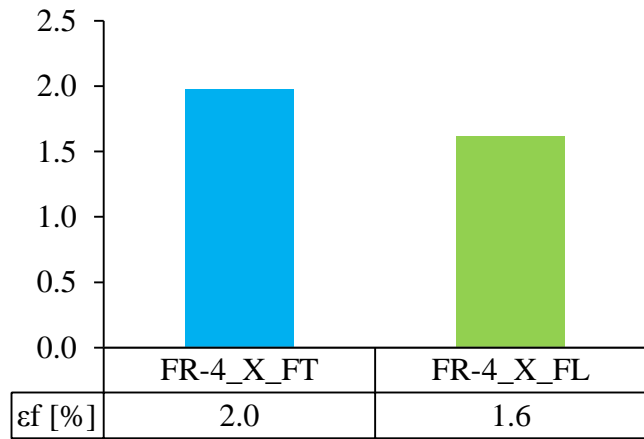|	FR-4_X_FT	FR-4_X_FL
εf [%]	2.0	1.6

Figure 5-20: Mean flexure strain

➢ **Offset flexure yield strength**

Analysis of Figure 5-22 showed that the extent of elastic deformation observed in the sample subjected to flexure stress was observed as high in the sample tested across the load-bearing fibres and lower in the one tested along. This means that the FR-4 sample did deflect elastically more when the flexure stress was applied in a direction transversal to the direction of orientation of the load-bearing fibres.

	FR-4_X_FT	FR-4_X_FL
■ σy [MPa]	183.9	116.4
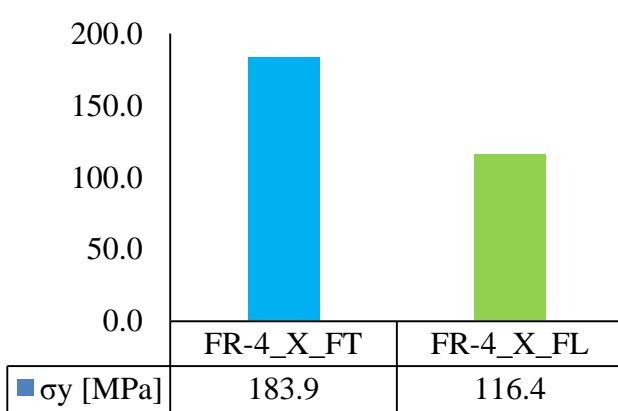
Figure 5-22: Mean offset flexure yield strength

	FR-4_X_FT	FR-4_X_FL
■ εo [%]	0.4	0.4
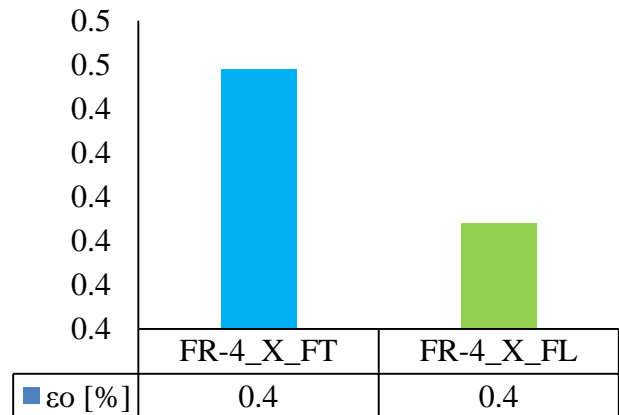
Figure 5-23: Mean offset strain

➢ **Deflection angle at fracture**

Figure 5-24 displays the mean deflection angle recorded in the sample at fracture, giving the extent to which the sample bends before fracture was noticed. The analysis showed that the sample tested across the 0° fibres failed at a higher deflection angle than that tested along the 0° fibres. This was supported by the fractography analysis of the failed surface in section 4.3 of Chapter 4; the microscopic analysis of the sample tested across the load-bearing fibres

showed that the load-bearing fibres bent largely before fracture. The fracture of the sample tested across the 0° fibres started from the bottom side midsection fibres of the sample. But for that tested along the load-bearing fibres, a high degree of fibre brooming was observed on the bottom midsection face of the failed sample. It showed that the interface fibres-matrix cracked before crack was observed in the specimen. Further analysis of Figure 5-16 confirmed that as the interface fibres-matrix of the FR-4 sample was strong, the sample was consequently highly ductile.

➢ **Flexure modulus of elasticity**

Figure 5-25 compared the flexure modulus of elasticity of the FR-4 sample tested across the load-bearing fibres against the one tested along. Analysis showed that the flexure modulus of elasticity measured across the 0° fibres was the greatest. This suggested that the FR-4 sample did react elastically much better to flexure stress applied across its load-bearing fibres.

	FR-4_X_FT	FR-4_X_FL
■ θ˚	52.3	42.5
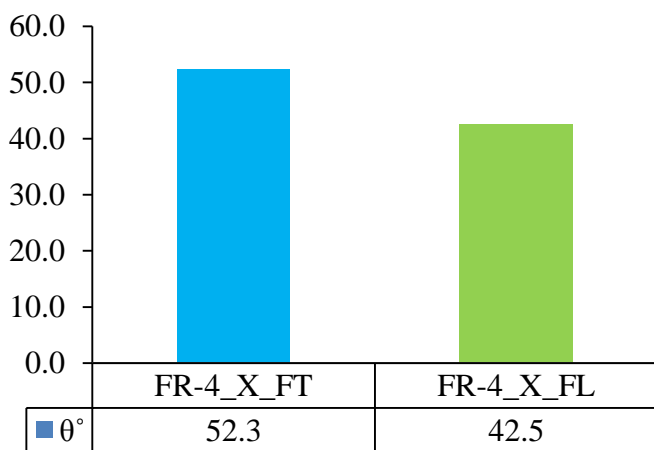
Figure 5-25: Mean deflection angle at fracture

	FR-4_X_FT	FR-4_X_FL
■ Ef [GPa]	42.0	27.4
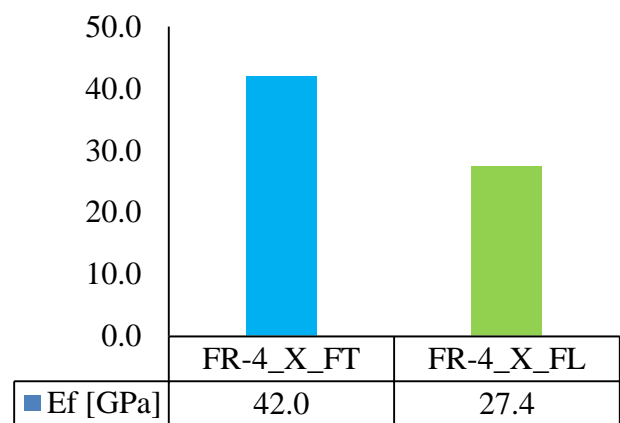
Figure 5-24: Main flexure modulus of elasticity

2) **Mercurywave sample**

The stress-strain curves of Figure 5-26 compared the reaction of the Mercurywave sample tested along the load-bearing fibres to the one tested across. The figure showed similar reactions in the behaviour of the sample tested along and across the 0° fibres. It was noted that the steepness and stiffness of the two samples were almost the same as the two curves followed almost the exact same path, but the sample tested across the 0° fibres showed high flexure strength and higher flexure strain. A detailed comparison of the different evaluated

properties below did help establish the difference the Mercurywave sample yielded when tested in the two directions
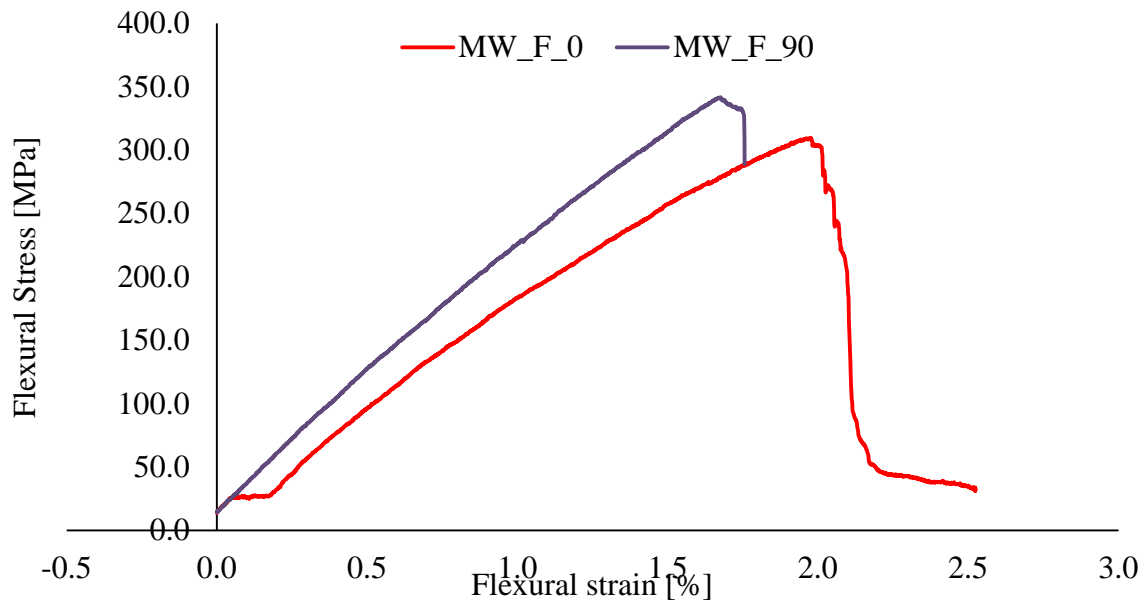
Figure 5-26: Stress-strain curves of Mercurywave sample tested along vs. across load-bearing fibres

➢ **Bending stiffness**

Figure 5-27 compared the rate at which the samples bent under the application of flexure stress. Analysis showed that the Mercurywave sample opposed high resistance to bending when subjected to flexure stress applied across the axis of its 0° fibres. As research had revealed that the bending stiffness of a material was a function of the strength of its load-

	XL	XT
■ k [N/mm]	18.5	28.1

Figure 5-27: Mean bending stiffness

bearing fibres, it was clearly established that the resistance of the sample to bending stress was found across its load-bearing fibres.

> **Flexure strength**

Analysis of the mean ultimate strength displayed in Figure 5-28 shows that X_L had the highest flexure strength; this means that as for the FR-4 sample, the Mercurywave sample did oppose high resistance to the a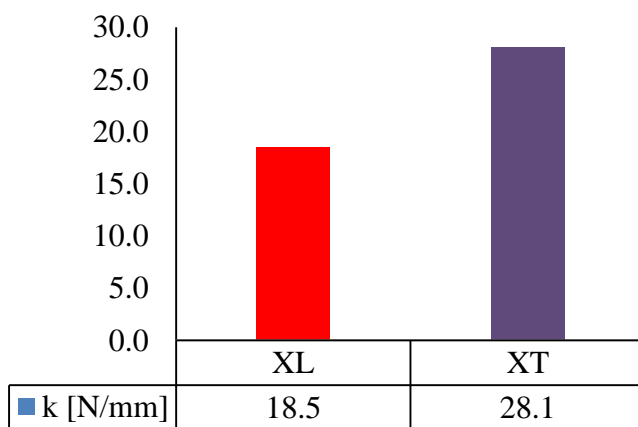pplication of flexure stress across its load-bearing fibres axis. The strength of the sample to flexure strength was a function of the transversal strength of the sample and the fractography analysis generated the same outcome as that of the FR-4 sample

> **Flexure strain**

Figure 5-29 compared the mean flexure strain measured on the Mercurywave sample tested along and across the 0° fibres. Analysis showed that the strain induced in the sample tested along the 0° fibres was the highest; this means that when subjected to flexure stress, the Mercurywave sample did deflect more along its 0° fibres axis before it failed. This also showed that the Mercury wave sample subjected to flexure stress was highly ductile along its load-bearing fibres

	XL	XT
■ εf [%]	1.8	1.6
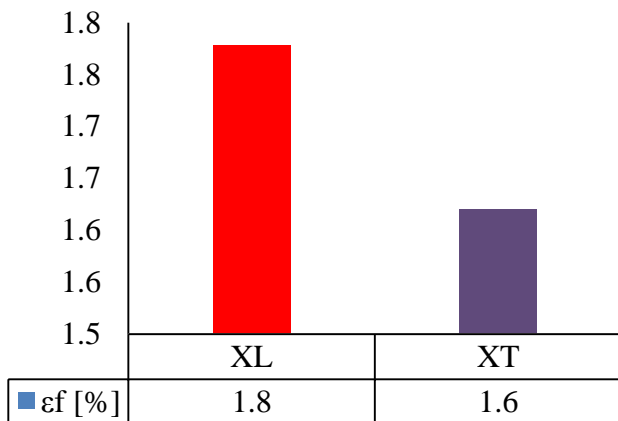
Figure 5-29: Mean flexure strain

	XL	XT
■ σf [MPa]	274.1	303.8

Figure 5-28: Mean flexure strength
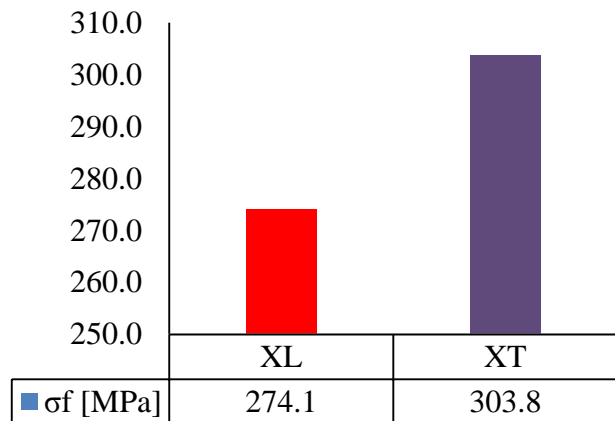
> **Offset flexure yield strength**

According to analysis of Figure 5-30, the extent of elastic deflection observed in the sample subjected to flexure stress was observed as high in the sample tested across the load-bearing fibres and lower in the one tested along. This meant that the sample tested across the fibres did deflect elastically more than that tested along the fibres.
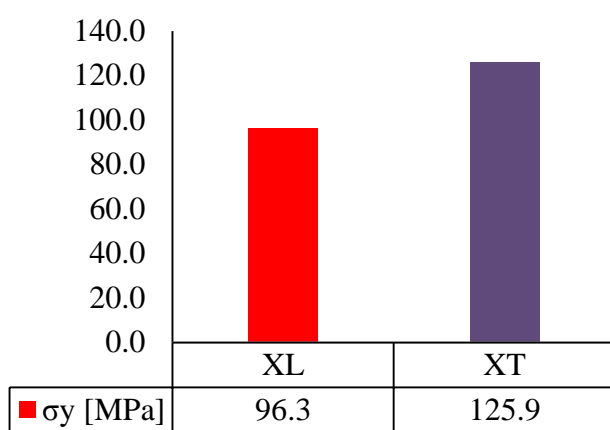
	XL	XT
■ σy [MPa]	96.3	125.9

Figure 5-31: Mean offset flexure yield strength
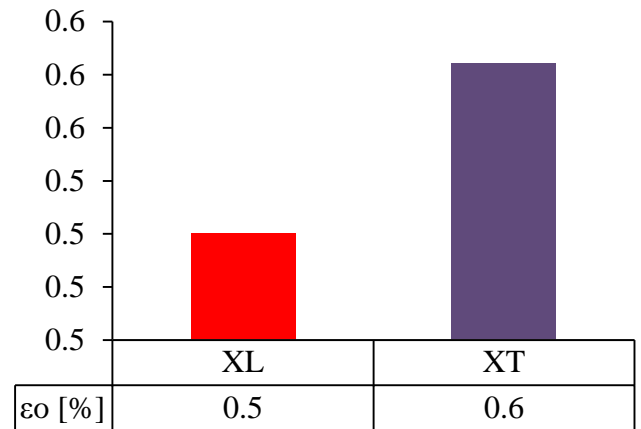

	XL	XT
εo [%]	0.5	0.6

Figure 5-30: Mean offset strain

➢ **Deflection angle at the fracture**

Figure 5-32 compared the mean deflection angle measured at fracture on the samples tested along versus across the 0° fibres. Analysis revealed that the sample tested across the 0° fibres deflected at a high angle before its fracture occurs. This was supported by the fractography analysis of the failed surface area in section 4.4 of Chapter 4. Microscopic analysis of the sample tested across the load-bearing fibres showed that the fibres on the bottom side midsection of the sample deflected at a higher angle than the interface before fracture. But for that tested across the load-bearing fibres, a high degree of fibre brooming was observed on the surface area of the failed sample. This showed that the interface fibres-matrix deflected before they broke. Further analysis of Figure 5-23 showed that the interface fibres-matrix of the Mercurywave sample had a strong bond; therefore, the sample was ductile.

➢ **Flexure modulus of elasticity**

Figure 5-33 shows the mean flexure modulus of elasticity of the Mercurywave sample tested along versus the one tested across the load-bearing fibres of the sample. Analysis showed that the sample tested across the fibres had a high flexure modulus of elasticity; this meant that the sample was more elastic across its load-bearing fibres when subjected to flexure stress.
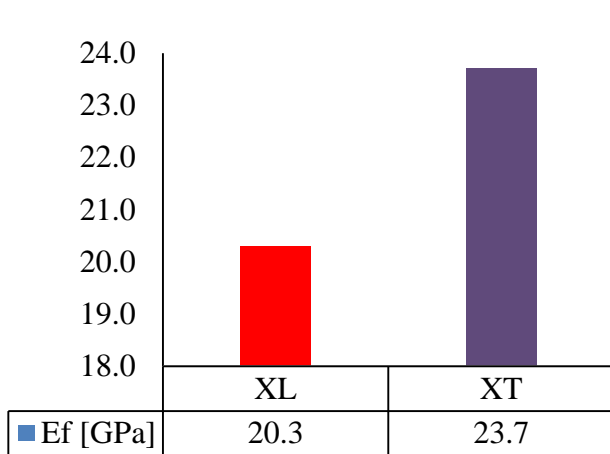
	XL	XT
■ Ef [GPa]	20.3	23.7

Figure 5-33: Mean flexure modulus of elasticity

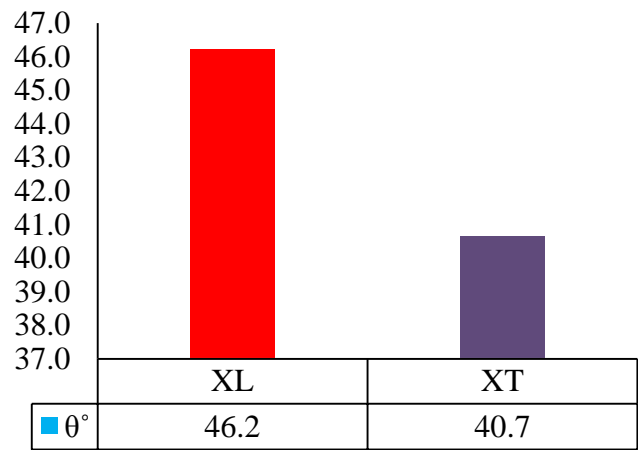

	XL	XT
■ θ˚	46.2	40.7

Figure 5-32: Mean deflection angle at fracture

5.2.2. Reaction of the samples relative to the substrate used

Figure 5-34 shows stress-strain curves describing the behaviour of the four samples discussed above. It was clearly established that the FR-4 sample tested across the 0° fibre was steeper and stiffer than the Mercurywave sample tested along the same axis; this observation was supported by the comparison of their mean flexure strength, discussed as follows.

The mean lowest flexure stress that can cause minimum deflection of the FR-4 sample was found at 48.2628 MPa along the 0° fibres and 40.8121 MPa; that of the Mercurywave sample was at 28.8256 MPa along the 0° fibres and 26.5733 MPa across. Thus, the mean lowest flexure stress that can affect the operational integrity of the FR-4 sample was 40.274% greater than that of the Mercurywave sample along the 0° fibres and 34.889% across.

The mean bending stiffness measured on the FR-4 sample determined at 18.417% greater than that of the Mercurywave sample tested along the load-bearing fibres and 13.092% across. It was therefore stated that the FR-4 sample had a high resistance to bending stress.

The mean flexure strength of the FR-4 sample was 17.838% greater than that of the Mercurywave sample tested along the load-bearing fibres and 49.585% across. The flexure strength of the FR-4 sample tested across the 0° load-bearing fibres had a flexure strength that was almost double that of the Mercurywave sample tested along the same direction. It can therefore be said that the FR-4 sample opposed higher resistance to the application of flexure stress than Mercurywave sample.

The mean flexure strain of the FR-4 sample was determined as 8.984% smaller than that of the Mercurywave sample tested along the 0° fibres and 18.181% across. Compared to that of the strength, the rate at which the strains differed between the two specimens measured along versus across the load-bearing fibres was small. It can be concluded that the FR-4 sample was more ductile than the Mercurywave sample for it deflected more before fracture while subjected to flexure stress.
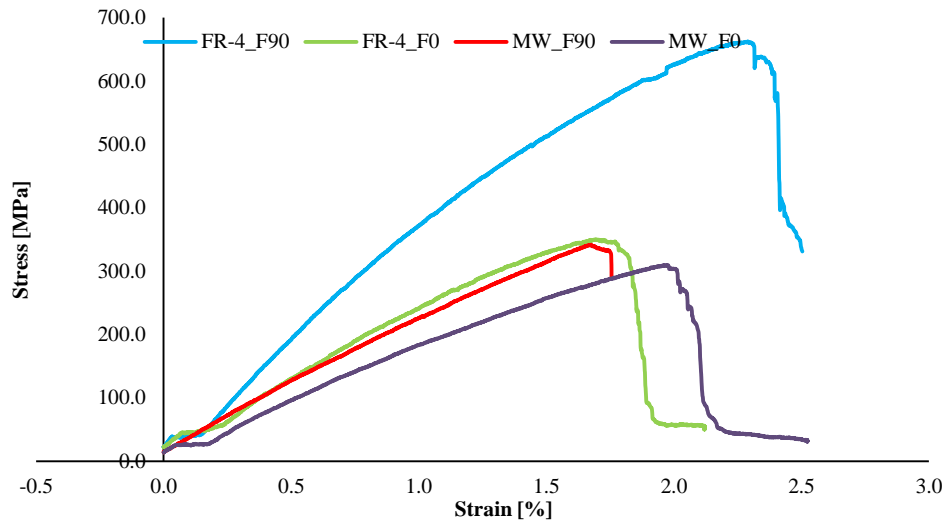

Figure 5-34: Stress-strain curves of the FR-4 sample versus Mercurywave sample

The mean offset flexure yield strength of the FR-4 sample was 17.250% greater than that of the Mercurywave sample tested along the load-bearing fibres and 31.565% across. This showed that the Mercurywave sample expanded more elastically than the FR-4 sample when subjected to flexure stress applied across the load-bearing fibres and less when the stress was applied along.

The mean deflection angle at fracture measured on the FR-4 sample was 8.080% greater than that of the Mercurywave sample tested along the load-bearing fibres and 22.268% across. It can therefore be said that the extent to which the FR-4 sample deflected under the flexure stress was much larger than that of the Mercurywave sample. This supports the observation for the strain and the analysis of the curves of Figure 5-30 where it was evident that the FR-4 sample was reported to be more highly ductile than the Mercurywave sample.

The mean flexure modulus of elasticity of the FR-4 sample was 25.980% greater than that of the Mercurywave sample tested along the load-bearing fibres and 43.585% across. This supported the observation in the discussion of the yield strength where it was found that the

rate of elastic behaviour of the FR-4 sample was much better than that of the Mercurywave sample subjected to flexure stress.

5.3. Reaction of the samples to tensile stress versus flexure stress

From the discussion done in section 5.1 and 5.2, it was observed that the samples were stiffer and steeper to flexure stress, but highly ductile to tensile stress. A comparison done between the tensile and flexural stress revealed that:

The flexure strength of the FR-4 sample was 39.772% greater than the ultimate tensile strength along the load-bearing fibres and 74.892% across, and that of the Mercurywave sample was 51.107% along the load-bearing fibres and 66.598% across. Therefore, it can clearly be said that the boards are more vulnerable to tensile stress but can withstand higher flexural stress.

The offset yield strength of the specimen under flexural stress was found to be 71.15% greater than that of the FR-4 subjected to tensile stress along the load-bearing fibres and 77.60% across, and that of the Mercurywave was 57.32% greater along and 72.04% greater across. It was then stated that the extent of elastic deformation of the sample was high when subjected to flexural stress then when subjected to tensile stress

The flexure modulus of elasticity of the FR-4 sample was 75.286% greater than Young's modulus of elasticity along the load-bearing fibres and 84.926% across, and for the Mercurywave sample, it was 72.217% along and 75.316% across the load-bearing fibres. Therefore, it was found that the boards have high elastic deformation under flexural stress compared to tensile stress.

From the above comparisons, it was concluded that the boards behave well to flexural stress rather than to tensile stress.

6.   CONCLUSION AND RECOMMENDATIONS

6.1. Conclusion

The goal of this research work was to characterise mechanically the printed circuit boards used in the development of the South African nanosatellite mission. Three objectives were defined as fundamental to a successful achievement of the aims. They included characterisation of the reaction of the PCBs to tensile stress, characterisation of the reaction of the PCBs to flexure stress and determination of the allowable mechanical stress the PCBs can withstand without compromising performance while subjected to tensile and flexure stress. Tensile tests were undertaken on 24 specimens obtained from four samples: two were made of FR-4 substrate and two of Mercurywave substrate. The specimens were tested on a 50 kN Hounsfield UTM. The flexure tests were conducted on 16 specimens obtained from six samples, three made of FR-4 substrate and three made of Mercurywave substrate. The analysis of the results from Chapter 4 and the discussion presented in Chapter 5 largely characterise the PCBs used for nanosatellites application to tensile and flexure stress. The mechanical characterisation was conducted on the basis of two important factors: the orientation of the applied load relative to the orientation of the load-bearing fibres of the sample, and the substrate used in the manufacturing of the PCBs. The following observations summarized the findings of the present research work:

- The board should be used in such a way that the tensile stress is induced along the axis of its load-bearing fibres and the flexure stress is induced across the axis of its load-bearing fibres to ensure structural integrity of the board.
- The maximum allowable stress the boards can withstand without affecting the operational integrity of an electronic package, a subsystem or a system as a whole was found to be 8.4524 MPa for the FR-4 sample and 9.4854 MPa for the Mercurywave sample under tensile stress, and 40.8121 MPa for the FR-4 sample and 26.5733 MPa for the Mercurywave sample under flexure stress.
- The FR-4 sample presented high resistance to the application of tensile stress with a computed ultimate tensile strength of 200.9084 MPa, but the Mercurywave sample presented lower resistance with a calculated ultimate tensile strength of 134.0048 MPa. This means that the Mercurywave sample is lighter than the FR-4 sample.
- The FR-4 sample presented higher deformation to the application of the tensile stress with a calculated ultimate tensile strain of 9.8201%, but the Mercurywave sample presented

lower deformation to the application of tensile stress with a computed ultimate tensile strain of 7.1208%. This means that the FR-4 sample will elongate more than the Mercurywave sample.

- The elastic deformation of the FR-4 sample was found to be higher than that of the Mercurywave with a Young's modulus of elasticity of 6.7787 GPa and a Poisson's ratio of 0.8836% for the FR-4, and 5.8522 GPa and 0.8311% for the Mercurywave sample.

- The extent of plastic deformation was found to be high for the FR-4 sample with a percentage elongation of 9.7891%, but the Mercurywave sample presented a lower plastic deformation with a calculated percentage elongation of 7.0948%. This means that the FR-4 sample is more ductile than the Mercurywave sample, but both are ductile materials.

- The FR-4 sample presented a high bending stiffness of 32.3438 N/mm and the Mercurywave the lower one of 28.1094 N/mm. This means that the FR-4 sample is 13.0918% stiffer than the Mercurywave sample.

- The FR-4 sample presented higher flexure strength of 602.6554 MPa and the Mercurywave the lower of 303.8314 MPa. This means that the FR-4 sample was much stronger than the Mercurywave sample.

- The FR-4 sample presented high flexure strain of 1.9801% and the Mercurywave the lower flexure strain of 1.6201%. This means that the FR-4 sample is more flexible than the Mercurywave.

- The FR-4 sample presented high flexure modulus of elasticity of 42.0242 GPa and the Mercurywave sample the lower of 23.7080 GPa. This means that the FR-4 sample is more elastic than the Mercurywave sample.

- The FR-4 sample presented a high deflection angle at fracture of 52.3057^o and the Mercurywave sample the lower of 46.2243^o. This means that the FR-4 sample is more ductile than the Mercurywave sample.

This study found that the FR-4 had good reaction to flexural and tensile stress. it was found that the FR-4 substrate was more ductile in tension and stiffer in flexure than the Mercurywave substrate, additionally it is less costly. Given these benefits, the FR-4 substrate is the best option for low-cost nanosatellites mission design.

6.2. Recommendations

From the discussion of the results obtained from the experimental tests, the following recommendations are offered:

- Fatigue tests should be conducted to assess the reaction of the boards to cyclic loading to address the endurance and fracture toughness of the boards.
- In-service fracture analysis should be conducted to determine the initiation of crack in the sample under tensile and flexure stress.
- Due to luck of fundings, the research work was limited to analysing the mechanical reaction of the boards as a complex material, but further work is required to investigate this material with at least six replicate per specimen.

BIBLIOGRAPHY

Adams, D.F., Carlsson, L.A. & Pipes, R.B. 2002. *Experimental characterization of advanced composite materials*. 4th ed. Taylor & Francis Group, ed. London, N.Y.: Chemical Rubber Company (CRC). http://www.taylorandfrancis.com.

Barua, T., Mahmood, A., Rajashekar, K., Sabne, S., Sakib, A.R.N. & Agonafer, D. 2016. Effect of removal of layers of WCSP assembly under thermal cyclic loading: A computational approach. In *Proceedings of the 15th InterSociety Conference on Thermal and Thermomechanical Phenomena in Electronic Systems, ITherm 2016*. Texas: IEEE: 101–106.

Bhavsar, N.R., Shinde, H.P. & Bhat, M. 2014. Determination of mechanical properties of PCB. *International Journal on Mechanical Engineering and Robotics (IJMER)*, 2(4): 23–27.

Botelho, E.C. & Almeida, R.S. 2007. Elastic properties of hygrothermally conditioned glare laminate. *International Journal of Engineering Science*, 45: 163–172. www.elsevier.com/locate/ijengsci.

Chen, X. 2020. Fractographic analysis of sandwich panels in a composite wind turbine blade using optical microscopy and X-ray computed tomography. *Engineering Failure Analysis*, 111: 1–12. https://doi.org/10.1016/j.engfailanal.2020.104475.

Church, K.H., Tsang, H., Rodriguez, R., Defembaugh, P. & Rumpf, R. 2013. Printed circuit structures, the evolution of printed circuit boards. *IPC APEX EXPO Conference and Exhibition 2013, APEX EXPO 2013*, 2: 1242–1261.

Dasari, S., Lohani, S., Sumit Dash, S., Omprakash Fulmali, A., Kumar Prusty, R. & Chandra Ray, B. 2021. A novel study of flexural behavior of short glass fibers as secondary reinforcements in GFRP composite. *Materials Today: Proceedings*, 47: 3370–3374. https://doi.org/10.1016/j.matpr.2021.07.161.

Deepak, R.A. & Twiggs, R.J. 2012. Thinking out of the box : Space science beyond the CubeSat. *Journal of small Satellites (JOSS)*, 1(1): 3–7. www.JoSSonline.com.

Dowling, N.E. 2013. *Mechanical behavior of materials; engineering methods for deformation, fracture and fatigue*. 4th ed. Integra-Software-Services-Pvt.Ltd, ed. Westford USA: Pearson Education Limited. www.pearsoninternationaleditions.com.

Forster, A.M. 2015. *Materials testing standards for additive manufacturing of polymer materials: State of the art and standards applicability*. Gaithersburg, MD. https://nvlpubs.nist.gov/nistpubs/ir/2015/NIST.IR.8059.pdf.

Greaves, G.N. & , A. L. Greer, R.S.L. and T.R. 2011. Poisson's ratio and modern materials. *Nature materials*, 10(October): 823–837. www.nature.com/naturematerials 823 nmat_3134_NOV11.indd.

Greenhalgh, E.S. 2013. *Failure analysis and fractography of polymer composites*. SNP Best-set Typesetter Ltd., ed. New Delhi: Woodhead Publishing Limited.

Harizi, W., Chaki, S., Bourse, G. & Ourak, M. 2022. Damage mechanisms assessment of Glass Fiber-Reinforced Polymer (GFRP) composites using multivariable analysis methods applied to acoustic emission data. *Composite Structures*, 289: 1–18.

Hassan, M. 2016. *Effect of Poisson ' s ratio on material properties characterization by nanoindentation with a cylindrical flat tip indenter*. South Dakota State University. https://openprairie.sdstate.edu/etd/1020%0AThis.

Itugha, O.D. & Jumbo, E.E. 2019. Experimental determination of young ' s modulus of elasticity between construction materials using some test metals and woods american journal of engineering research (AJER). *American Journal of Engineering Research (AJER)*, 8(4): 376–386. www.ajer.org.

Jayaraman, S., Trikha, M., Somashekar, Kamesh, D. & Ravindra, M. 2016. Response Spectrum Analysis of Printed Circuit Boards Subjected to Shock Loads. *Procedia Engineering*, 144(12): 1469–1476. http://dx.doi.org/10.1016/j.proeng.2016.06.710.

Kalia, S., Gurau, V.S. & Kumar, A. 2018. Experimental study of tensile strength of glass-epoxy composites at different laminate orientations. *International Journal of Advanced Engineering, Management and Science*, 4(8): 590–593. https://dx.doi.org/10.22161/ijaems.4.8.2.

Lee W. Ritchey. 1999. A survey and tutorial of dielectric materials used in the manufacture of printed circuit boards. In L. Ritchey, ed. *PCB Design Conference west*. S. I: Lee Ritchey of speeding edge: 1–10.

Loon, K.T., Kok, C.K., Mohd Noor, E.E. & Ooi, C.C. 2019. Modeling the elastic behavior of an industrial printed circuit board under bending and shear. *IEEE Transactions on Components, Packaging and Manufacturing Technology*, 9(4): 669–676.

Mabuwa, S. 2022. *Development of new FSP method for enhancing the mechanical properties of FSW and TIG welded dissimilar aerospace aluminium alloy joints*. Cape Peninsula University of Technology.

Marques, T.P.Z., Mayer, S., Cândido, G.M. & Rezende, M.C. 2021. Fractographic analysis of scarf repaired carbon/epoxy laminates submitted to tensile strength. *Engineering Failure Analysis*, 124: 1–11. www.elsevier.com/locate/engfailanal 16 October 2022.

Monticeli, F.M., Voorwald, H.J.C. & Cioffi, M.O.H. 2022. The influence of carbon-glass/epoxy hybrid composite under mode I fatigue loading: Hybrid fiber bridging zone model. *Composite Structures*, 286: 1–8. www.elsevier.com/locate/compstruct%0AThe.

Montrose, M.I. 2000. *Printed circuit board design techniques for EMC compliance*. 2nd ed. IEEE-Press series on electronics technology, ed. New York: Wiley-interscience.

Oh, H.-U., Jeon, S.-H. & Kwon, S.-C. 2014. Structural design and analysis of 1U standardized step cube lab for on-Orbit verification of fundamental space technologies. *International Journal of Materials, Mechanics and Manufacturing*, 2(3): 239–244. https://www.researchgate.net/publication/287517736%0AStructural.

Opelt, C. V., Cândido, G.M. & Rezende, M.C. 2018. Compressive failure of fiber reinforced polymer composites – A fractographic study of the compression failure modes. *Materials Today Communications*, 15: 218–227. https://doi.org/10.1016/j.mtcomm.2018.03.012.

Opelt, C. V., Paiva, J.M.F., Cândido, G.M. & Rezende, M.C. 2017. A fractographic study on the effects of hygrothermal conditioning on carbon fiber/epoxy laminates submitted to axial compression. *Engineering Failure Analysis*, 79: 342–350. www.elsevier.com/locate/engfailanal%0AA.

Pietrikova, A., Lenger, T. & Livovsky, L. 2020. Mechanical properties of sandwich electronic boards after multi reflow exposure. In *Proceedings of the 2020 International Conference on Diagnostics in Electrical Engineering, Diagnostika 2020*. 5–8.

Printplaat. Protoboard PC board FR-4 manufacture prototype fabrication. *Alibaba Express*. https://m.aliexpress.com/item/33025983241.html?gatewayAdapt=Pc2Msite 12 March 2022.

Rahangdale, U., Sakib, A.R., Chaudhari, M., Misrak, A., Dave, C., Agonafer, D., Lohia, A., Kummerl, S. & Nguyen, L.T. 2017. Mechanical characterization of RCC and FR4 laminated PCBs and assessment of their board level reliability. In *Proceedings of the 16th InterSociety Conference on Thermal and Thermomechanical Phenomena in Electronic Systems, ITherm 2017*. Texas: 1111–1118.

Sharavanan, S., Vijaya Ramnath, B., Chandrasekaran, M. & Rajesh, S. 2018. Experimental investigation of flexural and hardness behaviour of hemp flax hybrid composite. *International Journal of Mechanical and Production Engineering Research and Development*, 8(4): 55–60. www.tjprc.org.

Sharma, S.P. & Lakkad, S.C. 2015. Impact behavior and fractographic study of carbon nanotubes grafted carbon fiber-reinforced epoxy matrix multi-scale hybrid composites. *Composites Part A: Applied Science and Manufacturing*, 69: 124–131. http://dx.doi.org/10.1016/j.compositesa.2014.11.005.

Sri, P.R., Sri, V.M. & Rao, D.S. 2015. Modeling & Testing Of Hybrid Composite Laminate. *IOSR Journal of Mechanical and Civil Engineering*, 12(1): 13–15. www.iosrjournals.org.
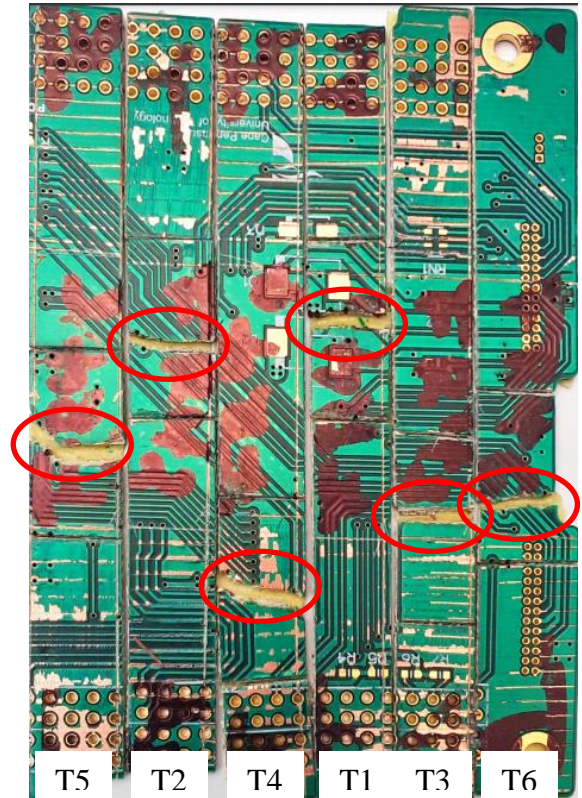
Ting, T.C.T. & Chen, T. 2005. Poisson's ratio for anisotropic elastic materials can have no bounds. *Quarterly Journal of Mechanics and Applied Mathematics*, 58(1): 73–82.

Uleiwi, J.K. 2007. Experimental study of flexural strength of laminate composite material. *Eng. & Technology*, 25(3): 454–466.
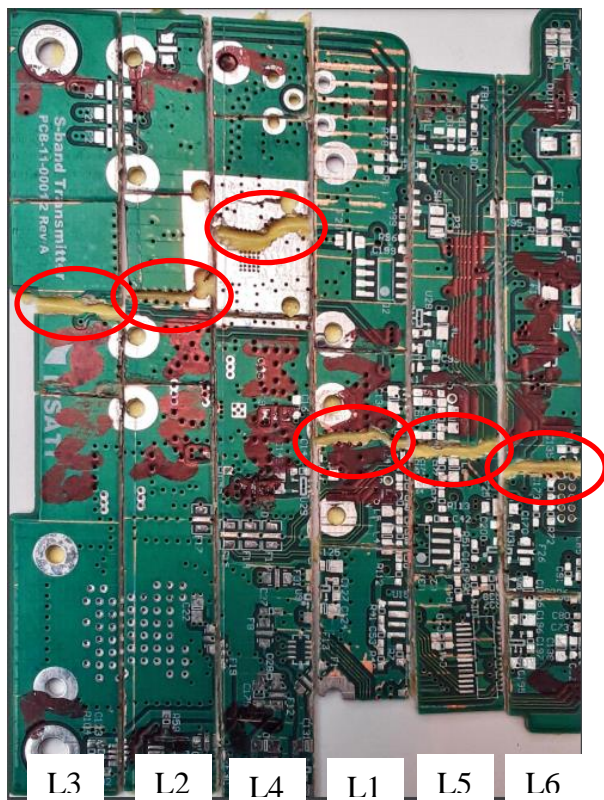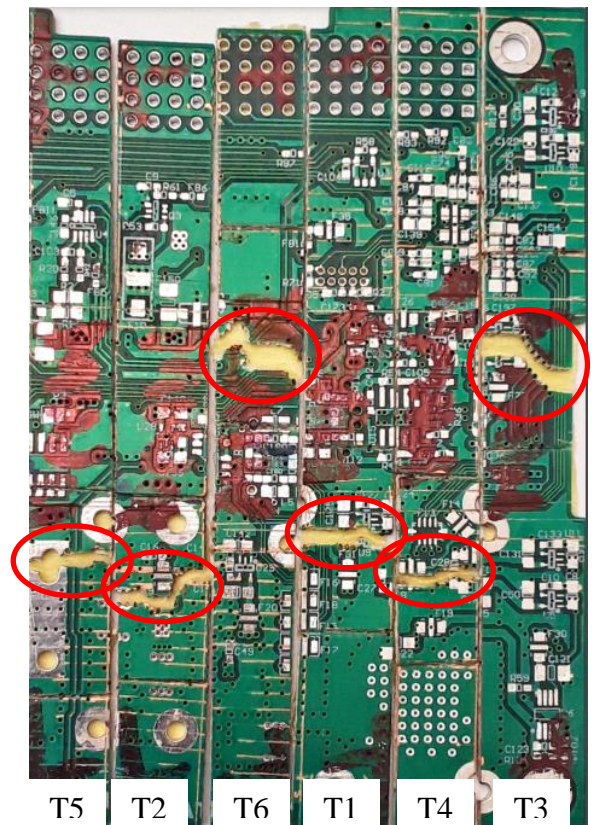
APPENDIX A: Specimens failed under tensile stress
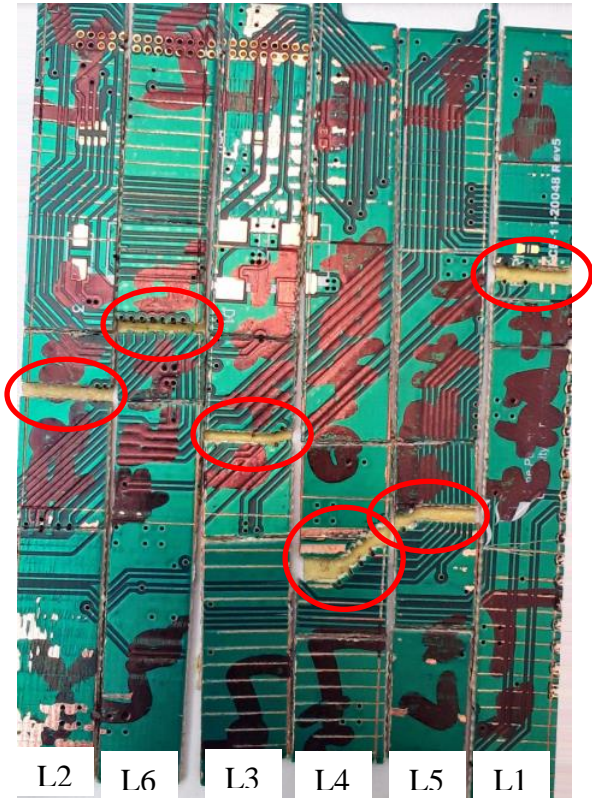
L2 | L6 | L3 | L4 | L5 | L1

FR-4 specimens tested along the fibres

T5 | T2 | T4 | T1 | T3 | T6

FR-4 specimens tested across the fibres

L3 | L2 | L4 | L1 | L5 | L6

Mercurywave specimens tested along the fibres
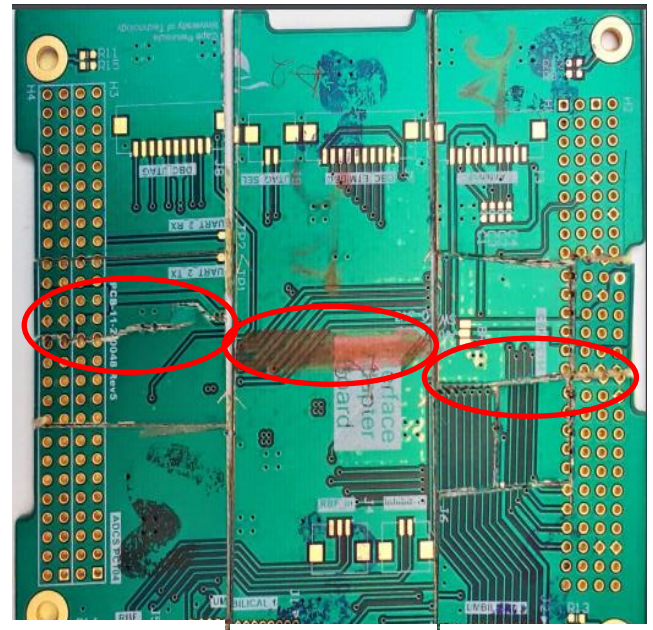

T5 | T2 | T6 | T1 | T4 | T3

Mercurywave specimens tested across the fibres
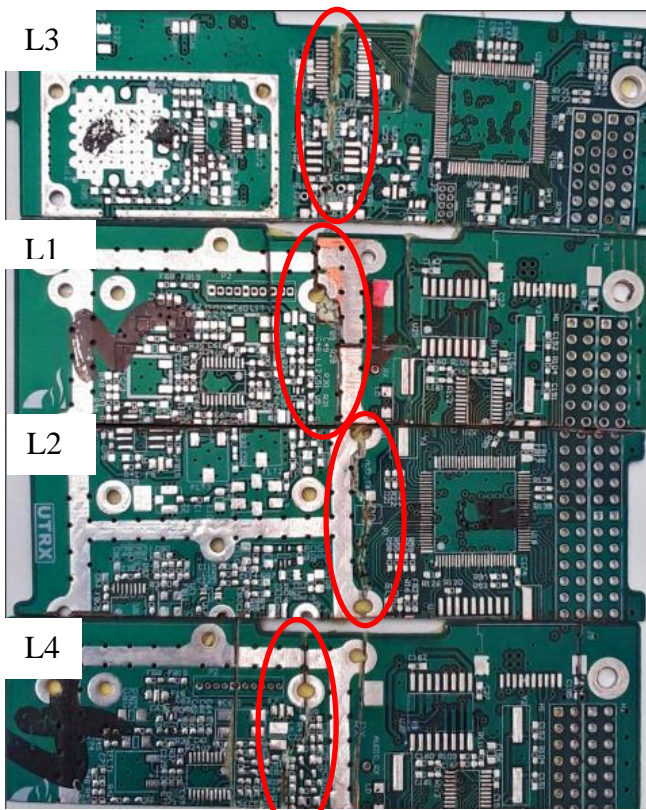
APPENDIX B: Specimens failed under flexural stress
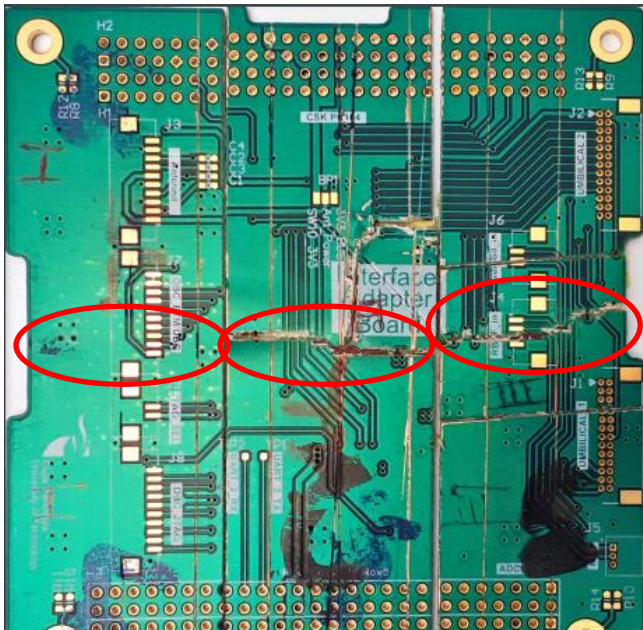
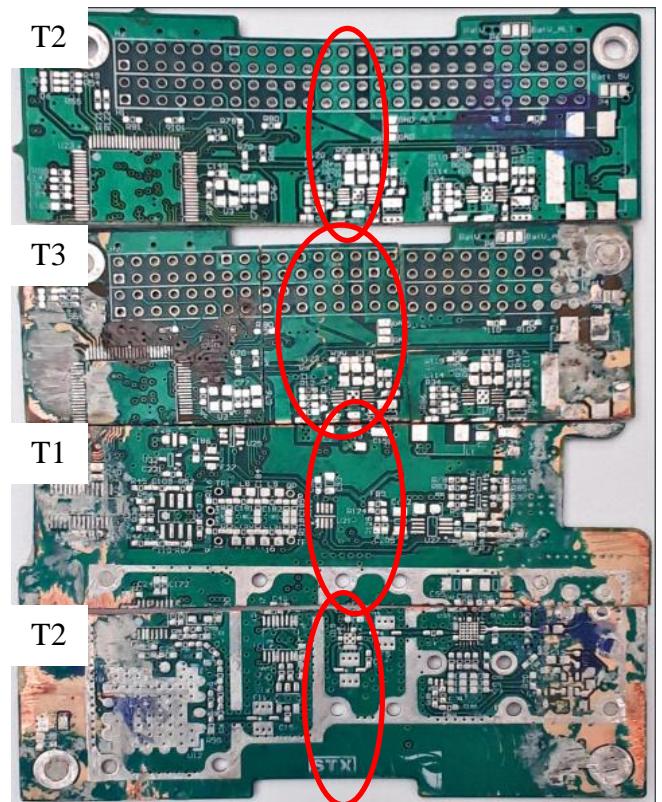

L1&4   L2   L3

FR-4 specimens tested across the fibres

T1&4   T2   T3

FR-4 specimens tested along the fibres

L3

L1

L2

L4

Mercurywave specimens tested across the

T2

T3

T1

T2

Mercurywave specimens tested along the fibres